Doctoral Dissertation

博士論文

Many-body effect on quantum transport in superconducting circuits

（超伝導回路における量子輸送と多体効果）

A Dissertation Submitted for the Degree of Doctor of Philosophy

December 2021

令和３年１２月博士（理学）申請

Department of Physics, Graduate School of Science,

The University of Tokyo

東京大学大学院理学系研究科

物理学専攻

Tsuyoshi YAMAMOTO

山本　剛史

Abstract

A superconducting circuit is one of the prominent candidates for the realization of quantum computation, which is the grand challenge in 21st-century science. The superconducting circuit has several advantages in a high degree of freedom for designing, and its elementary ingredients, such as superconducting qubits, transmission lines, and hybrid structures called the circuit quantum electrodynamics (QED), have been utilized for the application of quantum computers. The superconducting circuit also provides an ideal and useful platform for the study of fundamental physics. In particular, coupling to environments and disorder, which are usually obstacles for the realization of quantum computers, provides fascinating problems on many-body effects, quantum phase transition, localization, and heat transport.

In this thesis, we investigate three problems in superconducting circuits. First, we consider a quantum phase transition in the sub-Ohmic spin-boson system, which is realized by a charge qubit coupled to a transmission line, and study quantum critical phenomena in the frequency dependence of microwave scattering off this circuit. By performing the quantum Monte Carlo simulation, we find signatures of the quantum critical behavior as well as the Fermi-liquid-like feature indicated by the generalized Shiba-Korringa relation. We also describe how to construct the sub-Ohmic spin-boson system using superconducting circuits.

Second, we study the transmission properties through a Josephson-junction chain. This system is not only useful for application as a superinductor but also suitable to study many-body effects induced by Coulomb interaction and disorder. When the disorder is added to this system, the interplay of Coulomb interaction and disorder makes the Josephson-junction chain undergo a transition into an intriguing glassy insulator: Bose glass. We focus on the deep insulating regime and show that the collective pinning affects the dynamical properties of the Josephson-junction chain in the whole frequency region.

Finally, we study heat transport through an assembly consisting of a superconducting qubit sandwiched between superconducting harmonic resonators, which is described by the quantum Rabi model, a typical multi-level system. Using the non-perturbative approximation, we find a two-peak structure of the linear thermal conductance as a function temperature. This characteristic transport behavior comes from the fact that there are multiple levels in the assembly and is expected to be advantageous for the application of quantum heat devices.

These studies will provide a concrete foundation for further research on the physics of superconducting circuits. We also expect that the results obtained in this thesis will be observed in the near future.

Acknowledgements

I want to thank especially Professor Takeo Kato for supervising. He is very friendly, and I could ask him any little things about physics. His broad knowledge about mesoscopic physics was helpful for proceeding with my projects smoothly.

At the beginning of 2020, I stayed at CEA in Grenoble, France, for three months. There, I worked on a disordered Josephson-junction chain with Professor Manuel Houzet. I want to thank him for welcoming me to his group and working with me. His deep understanding of localization physics and great insight into the Josephson-junction chain helped my project for proceeding. Although it was my first time staying in a foreign country for over a week, I could enjoy Grenoble life thanks to members of IRIG/PHELIQS. I am also grateful to Professor Leonid I. Glazman. His helpful comments made our work more sophisticated.

This thesis would not have been possible without the funding from JSPS Research Fellowship for Young Scientists. During my stay at Grenoble, I was financially supported by the Innovative Professional Development (IPD) program. Without this support, I could not stay at Grenoble and work with Professor Manuel Houzet. Some numerical results presented in this thesis have been calculated on the supercomputer. I thank the Supercomputer Center, the Institute for Solid State Physics, the University of Tokyo for the use of the facilities.

During my five years at the Institute for Solid State Physics, the members of the Kato group have been continuously changing. I want to thank all members of the Kato group. They have made my graduate student life enjoyable. Rui Sakano is an assistant professor in the Kato group. Chatting with him about any topic was fun and relaxed me. In addition, he gave me useful comments for making presentations for scientific conferences and documents for the fellowship. Tomohiro Tamaya is a very passionate person about physics. He gave me a lot of advice as an academic researcher. Hiroko Eguchi is a secretary of the Kato group. She was always worried about me and helped me with doing paperwork.

Finally, I want to thank my parents. While there is little understanding of the Ph.D. in Japanese society, they accepted that I went on the Ph.D. course and encouraged me.

List of Publications

[1] "Microwave Scattering in the Subohmic Spin-Boson Systems of Superconducting Circuits",

T. Yamamoto and T. Kato, J. Phys. Soc. Jpn. **88**, 094601 (2019).

[2] "Transmission of waves through a pinned elastic medium",

T. Yamamoto, L. I. Glazman, and M. Houzet, Phys. Rev. B **103**, 224211 (2021).

[3] "Heat transport through a two-level system embedded between two harmonic resonators",

T. Yamamoto and T. Kato, J. Phys.: Condens. Matter **33**, 395303 (2021).

Contents

Chapter 1

Introduction

In this chapter, we briefly explain the research background of this thesis. After a brief overview of the many-body problems in superconducting circuits, we describe the purpose of this thesis. Finally, we give the outline of this thesis.

1.1   Development of quantum computer

The realization of quantum computation is one of the grand challenges in 21st-century science. The idea of the quantum computer was firstly proposed 40 years ago by Richard P. Feynman for simulating quantum systems that are too hard to do using classical computers [1]. While the information is expressed by a bit, which takes only two values, e.g., 0 or 1, in the classical computer, we can use their super-position $\alpha \left| 0 \right\rangle + \beta \left| 1 \right\rangle$ to perform computation in the quantum computer [2]. A set of two quantum states is called a "qubit" or "quantum bit" in analogy to the classical computer. Although this idea might sound like a *fantasy* at the time of the first proposal, quantum computers are now beginning to realize in various physical systems, e.g., superconducting circuits [3], semiconductors [4, 5, 6], or cold atoms [7, 8, 9].

A solid-state device using superconducting circuits is a leading candidate for the realization of quantum computers because of their high degree of freedom for designing, suppression of dissipation, and strong non-linearity. However, there still remain several problems to be overcome. One of the major problems is the loss of the devices' coherence. Since the solid devices inevitably interact with environments, the quantum coherence of qubits is lost in a finite amount of time. The coherence time of superconducting qubits was of the order of 1 ns at the beginning of the development [10]. Thanks to technological development, it has been improved for these twenty years to about 100 μs [11]. This remarkable improvement of coherence time has changed the situation of the development of quantum computers significantly. Recently, big companies, such as Google, IBM, Intel, and Microsoft, also joined quantum computer development. This trend will be accelerated in the future.

It is also worth noting that qubits can be coupled to an artificial environment fabricated on superconducting circuits in a controlled way. The circuit quantum electrodynamics (circuit-QED) has been studied intensively for the system composed of superconducting qubits and transmission lines [12]. The circuit-QED is now an essential technology for control of inter-qubit coupling and quantum measurement [13, 14, 15].

1.2   Superconducting circuits as a quantum simulator

We have mentioned the superconducting qubit as a leading ingredient of the quantum computer. To operate *correctly* it as the quantum computer, it is needed to put qubits on an ideal surrounding. However, in realistic systems, there are inevitable troublesome sources, such as disorder of circuits and interaction with the environments. For the realization of the quantum computer, they have to be suppressed as far as possible. However, in this thesis, we would like to promote the opposite direction. Namely, we focus on many-body effects induced by the presence of *bad* situation, such as strong coupling to the environment and randomness of the system. The superconducting circuits indeed provide an attractive stage to investigate fundamental physics related to many-body problems that emerge in such bad situations because of their high feasibility and controllability. In this sense, the superconducting circuit can be regarded as an ideal "quantum simulator" for solving the fundamental problems in quantum physics.

In the subsequent three subsections, we briefly overview many-body phenomena in superconducting circuits from three viewpoints. A detailed description, including experimental situations, will be given in Chapter 2.

1.2.1   Circuit-QED

Generally, it is challenging to realize a small quantum system strongly coupled to environments. For example, the interaction strength between an atom and the light in a vacuum is characterized by the fine structure constant $\alpha = 1/137 \ll 1$. In the cavity-QED system, the atom-light interaction can be strengthened by introducing a cavity for the light. Compared with the cavity-QED, the circuit-QED realized in the superconducting circuit has several advantages for realizing strong interaction between a superconducting qubit and electromagnetic field of the superconducting resonator because the superconducting qubit has a much larger dipole moment and a higher quality factor [12]. Therefore, the circuit-QED system is an ideal platform for realizing a strong coupling regime between the qubit and the resonator. Furthermore, the circuit-QED system allows us to realize a qubit system coupled to continuum environments that is described by a fundamental open quantum system called the spin-boson model. It is notable that the spin-boson model has been studied theoretically for a long time as a useful prototype for the study of decoherence due to the environment [16, 17, 18, 19, 20, 21, 22, 23]. It is also known that the spin-boson model exhibits many-body effects such as the Kondo-like effect and the quantum phase transition. Now, the recent technological development of superconducting circuits has enabled us to directly access these many-body effects in a controllable way.

1.2.2   Josephson-junction chain

Because of the flexibility in superconducting circuits, it is not difficult to fabricate a Josephson-junction chain. Actually, the recent development of fabrication techniques has enabled us to realize the long Josephson-junction chain in which each superconducting island is coupled to two neighboring islands via the Josephson coupling [24]. The Josephson-junction chain works as a high-impedance transmission line, known as a superinductor, and is useful for various applications. Moreover,

it exhibits the many-body phenomena, such as the superconductor-insulator transition, inherent to Coulomb interaction between Cooper pairs. Although it is possible to realize the Josephson junction chain with uniform junction parameters, the disordered potential for superconducting islands is inevitable because of charged impurities near the superconducting islands in the present technology. This disorder in the one-dimensional quantum system raises the localization, such as the Anderson localization for the non-interacting particles [25, 26, 27, 28]. Therefore, the Josephson-junction chain is an important system for investigating the localization problem incorporated with the many-body effect. In particular, the disordered Josephson-junction chain is an ideal system to study a compressible insulating state, which is called "Bose glass" [29, 30, 31, 32].

1.2.3 Quantum heat transport

Recent development in the technology of heat measurement has enabled us to study heat transport in superconducting devices [33, 34, 35]. The superconducting circuit provides an ideal platform to study quantum heat transport via a small quantum system. Heat transport in the superconducting circuit is mainly induced by energy transfer between two or more thermal baths of photons at low temperatures where phonon transport is negligible. In the analogy of the electronic devices, various quantum heat devices such as a quantum heat rectifier, a quantum heat valve, a quantum heat transistor, and a quantum heat engine have been proposed, and some of them have been implemented on the superconducting circuits [35].

Heat transport through a single superconducting qubit is one of the most fundamental problems in the study of quantum heat transport. This kind of heat transport can be described by the spin-boson model, which exhibits many-body effects as already described. The transport processes in heat transport through the single superconducting qubit (the two-level system) have been studied theoretically in the whole parameter region using the perturbative methods [36, 37] and the numerical simulations [23, 38]. From the viewpoint of the function as quantum heat devices, the system described by the spin-boson model is so simple that there is no room to demonstrate useful functions by controlling experimental parameters. Therefore, to gain a useful function in quantum heat devices, we need to expand the experimental setup beyond the single superconducting qubit.

1.3 Purposes

In this thesis, we theoretically study three types of many-body effects in superconducting circuits. First, we consider a single superconducting qubit (a two-level system) coupled to the environment based on the spin-boson model. In general, the environment of the spin-boson model is categorized into three types, i.e., sub-Ohimc, Ohmic, and super-Ohmic baths (see Chapter 2 for a detail). In this thesis, we focus on quantum phase transition in the sub-Ohmic spin-boson model and study how quantum critical phenomena are observed in microwave spectroscopy, employing the quantum Monte Carlo simulation and the renormalization-group analysis. In addition, we propose superconducting circuits which realize the sub-Ohmic spin-boson model.

Second, we study properties of microwave spectroscopy in a disordered Josephson-junction chain with emphasis on the deep insulating phase where the disorder of the system and the elasticity due to the long-range Coulomb interaction compete with

each other. By studying the frequency dependence of the microwave transmission, we find that the contribution of the forward and backward scatterings can be discussed separately and that the model for the Josephson-junction chain has a different universality from the known disordered model in the Bose glass phase.

Finally, we study quantum heat transport through a superconducting qubit embedded between two harmonic resonators, which is described by the quantum Rabi model. We show that this system has a sufficiently large degree of freedom for control of heat current compared with the standard spin-boson model. By employing the non-perturbative approximation called the noninteracting-blip approximation, we calculate the linear thermal conductance and discuss its temperature dependence. We seek out a parameter region where the transport property is peculiar to multi-level systems and clarify its mechanism. We find that the linear thermal conductance can be sensitive to a controllable parameter, which is advantageous for the application of quantum heat devices.

1.4   Outline

This thesis is organized as follows. In Chapter 2, we review how to treat the superconducting circuit theoretically. We explain theoretical descriptions for resonators, transmission lines, Josephson junctions, superconducting qubits, hybrid systems, and Josephson junction chains. We also review recent experiments for superconducting circuits and clarify the problems to be solved. In Chapter 3, we study the microwave reflection in superconducting circuits described by the sub-Ohmic spin-boson model [39]. We propose a circuit model to realize a sub-Ohmic spin-boson model and discuss quantum critical behavior through frequency dependence of the reflection amplitude in microwave spectroscopy. In Chapter 4, we investigate the microwave transmission through a disordered Josephson-junction chain [40]. By combining analytical methods and numerical calculation, we clarify the frequency dependence of the transmission in the localized regime and present several pieces of information on the transmission, the Lyapunov exponent, and the reflection phase. In Chapter 5, we study quantum heat transport through the quantum Rabi model [41]. Using the Keldysh formalism and the non-perturbative approach, we calculate the linear thermal conductance and show its temperature dependence in detail and clarify useful properties as quantum heat devices. Finally, we summarize our works and give future perspectives for them in Chapter 6.

Chapter 2

Review of Superconducting Circuits

In this chapter, we introduce various models for superconducting circuits, which will be used in the theoretical studies described in later chapters. First, we explain basic linear superconducting elements, an *LC*-circuit and a transmission line, in Section 2.1. We also introduce three types of superconducting qubits (charge qubit, transmon qubit, and flux qubit) in Section 2.3. Finally, we introduce three types of hybrid superconducting circuits, i.e., a dissipative superconducting qubit, a Josephson-junction chain, and quantum heat devices and briefly review recent experiments regarding each circuit.

2.1 Linear circuits

2.1.1 *LC*-circuit

First, we consider the *LC*-circuit, which is the simplest electrical circuit composed of an inductor with the inductance L and a capacitor with the capacitance C in parallel (see Fig. 2.1 (a)) [42]. The equations of motion for the voltage V and the current I of the *LC*-circuit are given by using the Kirchhoff's circuit laws

$$I(t) = -C\frac{dV(t)}{dt}, \tag{2.1}$$

$$V(t) = L\frac{dI(t)}{dt}. \tag{2.2}$$

From these equations of motion, we can obtain an equation for the current

$$\frac{d^2I(t)}{dt^2} = -\omega_0^2 I(t) \tag{2.3}$$
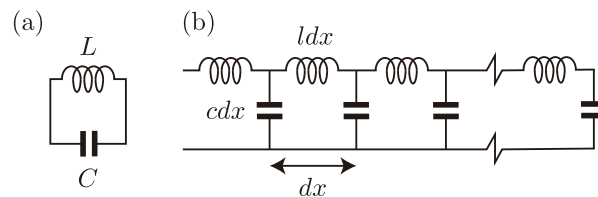
FIGURE 2.1: (a) *LC*-circuit and (b) lumped element model of the transmission line.

with $\omega_0 = 1/\sqrt{LC}$. This equation means that the current of the LC-circuit oscillates with the angular frequency ω_0.

Energies stored at the capacitor and the inductor are given by $(1/2)CV^2$ and $(1/2)LI^2$, respectively. Using relations between the charge and the voltage ($Q = CV$) and the charge and the current ($I = -\dot{Q}$), the total energy is expressed in terms of the charge as

$$\mathcal{H} = \frac{1}{2C}Q^2 + \frac{L}{2}\dot{Q}^2. \tag{2.4}$$

Now, introducing a flux variable ϕ defined as $\dot{\phi} = V$, which is conjugate to the charge,

$$[\phi, Q] = i\hbar, \tag{2.5}$$

the total energy is rewritten as

$$\mathcal{H} = \frac{1}{2C}Q^2 + \frac{1}{2L}\phi^2. \tag{2.6}$$

This Hamiltonian is identical to one of a harmonic oscillator with the correspondence $(p, x, m, k) \leftrightarrow (Q, \phi, C, L^{-1})$. Using this identity, we can quantize the LC-circuit in the same manner as the harmonic oscillator. Introducing bosonic annihilation and creation operators a and $a^\dagger$, respectively, which satisfy the commutation relation $[a, a^\dagger] = 1$,

$$\phi = \sqrt{\frac{\hbar Z_0}{2}} \left(a + a^\dagger \right), \tag{2.7}$$

$$Q = -i\sqrt{\frac{\hbar}{2Z_0}} \left(a - a^\dagger \right), \tag{2.8}$$

with an impedance of the LC-circuit $Z_0 = \sqrt{L/C}$, the Hamiltonian reads

$$\mathcal{H} = \hbar\omega_0 \left(a^\dagger a + \frac{1}{2} \right), \tag{2.9}$$

which means that the LC-circuit is a resonator with eigen angular frequency ω_0.

2.1.2 Transmission line

A transmission line is a useful ingredient of superconducting circuits in which electromagnetic waves can propagate freely (see Fig. 2.1 (b)). The transmission line is a natural extension of the LC-circuit and its Hamiltonian is obtained from the continuum limit of a series of the LC-circuits as

$$\mathcal{H} = \int_0^d dx \left\{ \frac{1}{2c} [Q(x)]^2 + \frac{1}{2l} [\partial_x \phi(x)]^2 \right\}, \tag{2.10}$$

where $Q(x)$ and $\phi(x)$ are the charge and flux variables which satisfy the commutation relation $[\phi(x), Q(y)] = i\hbar\delta(x - y)$. In a similar procedure to the LC-circuit, we can rewrite the Hamiltonian of the transmission line in terms of the bosonic annihilation and creation operators a_n and $a_n^\dagger$, respectively, which satisfy the commutation
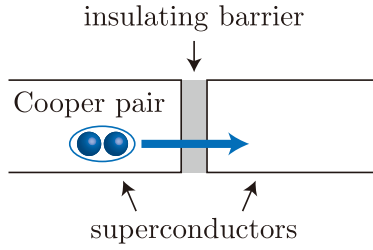
FIGURE 2.2: Josephson junction. Superconductors are interrupted by a thin insulating barrier. Copper pairs induce the supercurrent without any voltage.

relation $[a_n, a_m^\dagger] = \delta_{n,m}$, as

$$\mathcal{H} = \sum_k \hbar\omega_k \left(a_k^\dagger a_k + \frac{1}{2} \right), \tag{2.11}$$

where $\omega_k = |k|/\sqrt{lc}$ is the natural frequency of the kth mode. This form of the Hamiltonian means that transmission line is equivalent to a collection of harmonic oscillators. For a detailed derivation from the Lagrangian, see Appendix A.

2.2 Josephson junction

Next, we introduce a Josephson junction, which is a non-linear circuit ingredient to bring fruitful physics and complex functions of devices. A Josephson junction consists of two superconductors interrupted by a thin insulating barrier [43, 44] as shown in Fig 2.2. Through the Josephson junction, a supercurrent can flow without voltage drop across the barrier and its amplitude is given by the first Josephson relation

$$I_\mathrm{s} = I_\mathrm{c} \sin\varphi, \tag{2.12}$$

where φ is the phase difference between the two superconductors, which is called the Josephson phase and I_c is the critical current. When the constant voltage difference V is applied to the Josephson junction, the time evolution of the Josephson phase is governed by the second Josephson relation,

$$\frac{d\varphi(t)}{dt} = \frac{2e}{\hbar} V. \tag{2.13}$$

From these relations, (2.12) and (2.13), we can see that the Josephson junction behaves as an inductor with the Josephson inductance

$$L_\mathrm{J} \equiv \frac{V}{dI/dt} = \frac{\hbar}{2eI_\mathrm{c}\cos\varphi} = \frac{\hbar}{2eI_\mathrm{c}\sqrt{1 - (I/I_\mathrm{c})^2}}. \tag{2.14}$$

This relation indicates the non-linearity of the Josephson junction, which plays a crucial role in superconducting circuits. We note that for $I_\mathrm{c} \gg I$, the Josephson inductance becomes independent of the bias current as $L_\mathrm{J} = \hbar/(2eI_\mathrm{c})$. This linear inductor is useful for making lossless and high-impedance transmission lines.

(a)   (b)

E_J ✖ ═ C_J ⊠ $E_\mathrm{J}, C_\mathrm{J}$
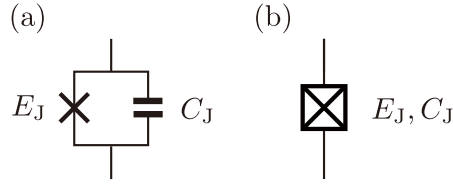
FIGURE 2.3: Symbols for the Josephson junction. (a) The Josephson junction with the capacitance C_J. (b) Symbol putting together the Josephson energy E_J and the self-capacitance for simplicity.

The energy stored in a Josephson junction can be calculated by integrating the electrical power in the Josephson junction with respect to time,

$$U = \int_0^t dt' \, V I_\mathrm{s} = \frac{\hbar}{2e} I_\mathrm{c} \int_0^t dt' \, \frac{d\varphi(t)}{dt} \sin\varphi(t) = E_\mathrm{J}(1 - \cos\varphi), \tag{2.15}$$

where $E_\mathrm{J} = (\hbar/2e) I_\mathrm{c}$ is a Josephson energy. The Josephson inductance can be rewritten with the Josephson energy as

$$L_\mathrm{J} = \left(\frac{\hbar}{2e}\right)^2 \frac{1}{E_\mathrm{J}}. \tag{2.16}$$

Besides the inductance, the Josephson junction has a capacitance, C_J, due to its geometry of the two spatially-separated superconducting electrodes (see Fig 2.3). This defines a charging energy at the Josephson junction

$$E_\mathrm{C} = \frac{(2e)^2}{2C_\mathrm{J}}. \tag{2.17}$$

Therefore, in the linear regime, the Josephson junction is equivalent to an LC-circuit with a resonance frequency

$$\omega_\mathrm{p} = \frac{1}{\sqrt{L_\mathrm{J} C_\mathrm{J}}}. \tag{2.18}$$

This frequency is called the plasma frequency of the Josephson junction.

Here, we present a remark regarding operators used to quantize the electrical circuit. For the linear circuits, we used the flux ϕ and the charge Q as conjugate variables (2.5). However, when treating the Josephson junction, the charge is quantized in units of $2e$ because Cooper pairs pass across the insulating barrier and contribute to the supercurrent. Then, it is convenient to use the number of Cooper pairs,

$$n = \frac{Q}{2e}, \tag{2.19}$$

instead of the charge. Moreover, the phase variable φ is used as the conjugate variable to n. The phase is related to the flux through the second Josephson relation (2.13) as

$$\varphi = \frac{2e}{\hbar} \phi. \tag{2.20}$$
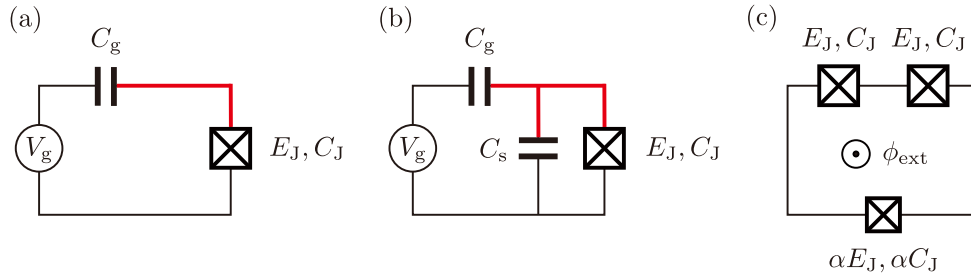
FIGURE 2.4: Circuits for three kinds of superconducting qubits; (a) charge qubit, (b) transmon qubit, (c) flux qubit. The red lines represent the Cooper-pair box.

Thus, the phase and the number of Cooper pairs satisfy the following commutation relation:

$$[n, \varphi] = i. \tag{2.21}$$

This non-linear element brings a quantum many-body effect under the dissipation. When a single Josephson junction is Ohmically shunted by a resistor, the Josephson junction shows a quantum phase transition due to the dissipation by the resistor, which is known as Schmid transition [45]. When the resistance R is larger than a resistance quantum, $R_{\mathrm{Q}} = h/(2e)^2$, the Josephson junction becomes insulating at zero temperature while when $R < R_{\mathrm{Q}}$, it becomes superconducting. This transition is related to the charge localization and has been studied theoretically in many literature [46, 47, 48, 49]. Recently, by replacing the normal resistor with the transmission line with the tunable impedance on superconducting circuits, the dynamical property was addressed in the wide parameter region [50]. We note that the Schmid transition has a different universality from a quantum phase transition in the Ohmic spin-boson model, which will be discussed in Section 2.5.

2.3 Superconducting qubits

A qubit is realized by a small quantum system consisting of two states. Among possible implementations of qubits in physical systems, a superconducting qubit is one of the most hopeful candidates due to its high feasibility and readout accuracy.

Generally, there are many states more than two in closed superconducting circuits. To use them as qubits, they have to be reduced to the effective two-state systems, i.e., the lowest two energy states are separated well from other higher states by utilizing the non-linearity of the Josephson junctions. In this section, we review three types of superconducting qubits, i.e., a charge qubit, a transmon qubit, and a flux qubit.

2.3.1 Charge qubit

The charge qubit is the simplest superconducting qubit which has been first implemented experimentally [10]. The charge qubit consists of a single Josephson junction with the large charging energy, the gate capacitance C_{g}, and the gate voltage V_{g} as shown Fig. 2.4 (a). The tiny superconducting island surrounded by the Josephson junction and the gate capacitance is called a Cooper-pair box (indicated by the red line in Fig. 2.4 (a)). For the charge qubit, it is convenient to adopt the charge states as
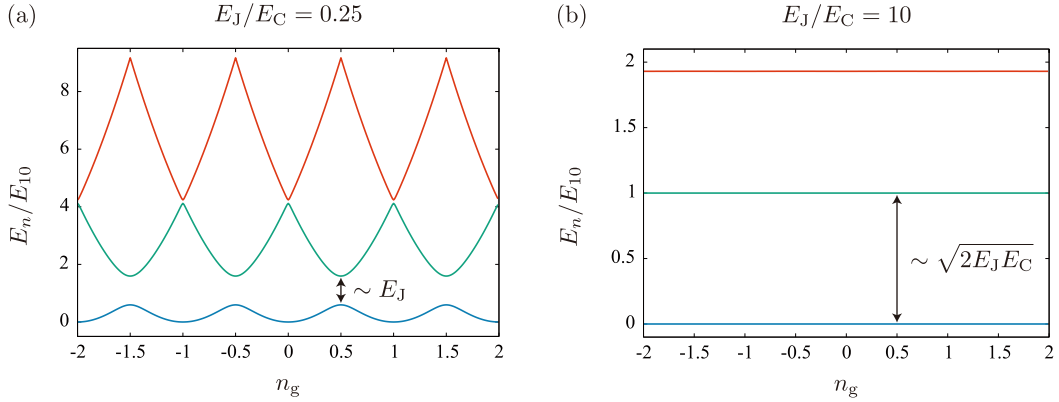
FIGURE 2.5: Energy spectrum ($n = 0$; blue, 1; green, 2; red) of Hamiltonian (2.24) as a function of the number of Cooper pairs induced by the gate voltage n_g for different $E_J/E_C =$ (a) 0.25; charge qubit, (b) 10; transmon qubit. The energy levels are normalized by the first transition energy $E_{10} = E_1 - E_0$ at $n_g = 1/2$. The minimum energy is set to the origin of energy.

basis states, where the states of the qubit are characterized by the number of Cooper pairs across the Josephson junction.

The Hamiltonian of the charge qubit is given by

$$\mathcal{H} = \frac{(Q - Q_g)^2}{2(C_J + C_g)} + E_J \left(1 - \cos\varphi\right), \tag{2.22}$$

where Q is an excess charge in the Cooper-pair box, i.e., the charge measured from its neutral state and φ is the phase difference across the Josephson junction. For convenience, we introduce new variables, the number of excess Cooper pairs, $n = Q/(2e)$ and $n_g = Q_g/(2e)$. The latter can be tuned by the gate voltage as $n_g = C_g V_g/(2e)$. The operator $e^{\pm i\varphi}$ changes the number of Cooper pairs in the Cooper-pair box by ∓ 1 because the phase and the charge are conjugate to each other (see Eq. (2.21)). The *cos*-term in the Josephson energy is then expressed in the charge basis $\{|n\rangle\}$ as

$$\langle n| \cos\varphi |m\rangle = \langle n| \frac{e^{i\varphi} + e^{-i\varphi}}{2} |m\rangle = \frac{\delta_{n,m+1} + \delta_{n,m-1}}{2}. \tag{2.23}$$

Therefore, the Hamiltonian of the charge qubit is written on the charge basis as

$$\mathcal{H} = \sum_{n=-\infty}^{\infty} E_C(n - n_g)^2 |n\rangle \langle n| - \sum_{n=-\infty}^{\infty} \frac{E_J}{2} \left(|n\rangle \langle n+1| + |n+1\rangle \langle n|\right). \tag{2.24}$$

where $E_C = (2e^2)/(C_J + C_g)$ and we have dropped the constant term.

The energy spectrum of the Hamiltonian (2.24) is shown as a function of n_g in Fig. 2.5. At large charging energies, $E_J/E_C < 1$, it is clear that the charging energy makes the energy spectrum with periodic parabolas and the Josephson energy opens an energy gap E_J at crossing points. From Fig. 2.5 (a), one can observe two features of the energy spectrum for the charge qubit. First, in contrast with the *LC*-circuit (see Eq. (2.9)), the energy spectrum has an anharmonicity due to the non-linearity of the Josephson junction. This anharmonicity plays a crucial role in using this circuit as a qubit. Second, the energy spectrum is not flat. This indicates that the charge qubit is

sensitive to the charge noise, resulting in a reduction in the coherence time.

When we set n_g to a half-integer, which is called a sweet spot, the lowest two energy levels are separated well from other energy levels. By neglecting higher energy levels except for the lowest two levels, the Hamiltonian of the charge qubit becomes

$$\mathcal{H} = \frac{E_C}{4} \left(|0\rangle \langle 0| + |1\rangle \langle 1| \right) - \frac{E_J}{2} \left(|0\rangle \langle 1| + |1\rangle \langle 0| \right). \qquad (2.25)$$

From this form, it is clear that the circuit can be reduced to a quantum two-level system; two states being degenerate in the charge basis, $|0\rangle$ or $|1\rangle$, correspond that the number of excess Cooper pairs in the Cooper-pair box is 0 or 1. Since the spectrum curvature around sweet spots is small, the effect of the charge noise can be reduced there.

2.3.2 Transmon qubit

In order to overcome the problem of the short coherence time, the transmon qubit, which is an abbreviation of "transmission line shunted plasma oscillation qubit", was developed in 2007 [51, 52]. The idea to achieve a long coherence time is to increase a ratio E_J/E_C. At large ratios, $E_J/E_C \gg 1$, the energy spectrum becomes flat and the transition energy between the ground and first-excited states becomes $\sim \sqrt{2E_J E_C}$ for arbitrary values of n_g [51], as shown in Fig. 2.5 (b). This means that the transmon qubit is insensitive to the charge noise, and it allows the transmon qubit to have a long coherent time, $> 100\ \mu$s, as observed in a recent experiment [53].

To increase the ratio E_J/E_C, the Cooper-pair box is shunted by a large capacitance C_s as shown in Fig.2.4 (b). This additional capacitance lowers the charging energy $E_C = (2e^2)/(C_J + C_g + C_s)$, resulting in the increase of the ratio E_J/E_C. Note that the circuit anharmonicity is reduced by increasing the ratio E_J/E_C to realize the insensitivity to the charge noise. As a result, the transmon qubit gets a longer coherent time at the expense of its anharmonicity. One might think that we need to consider not only the two lowest levels but also the higher levels due to weak anharmonicity. Actually, since the transmon qubit is coupled to the heat bath with a wide spectrum, the thermal excitation to the higher levels is relevant in general. However, in a typical experimental situation, the splitting energy of the transmon qubit is of the order of 0.5 K, and therefore the thermal population of the third level is sufficiently small at low temperatures $\lesssim 0.2$ K.

2.3.3 Flux qubit

Finally, we explain another famous superconducting qubit called the flux qubit [54, 55]. While the charge basis is considered as a convenient basis in the charge qubit, we use the flux (or phase) basis in the flux qubit. The flux qubit consists of a closed superconducting circuit interrupted by three Josephson junctions with an external flux ϕ_{ext} through the loop as shown in Fig. 2.4 (c).

Let us start with the Lagrangian. The Lagrangian of the flux qubit is expressed by a sum of the Lagrangian for each Josephson junction as

$$\mathcal{L} = \sum_{i=1,2,3} \left[\frac{C_{J,i}}{2} \dot{\phi}_i^2 + E_{J,i} \cos\left(\phi_i/\phi_0\right) \right], \qquad (2.26)$$

where $C_{J,i}$, $E_{J,i}$, and ϕ_i are the Josephson self-capacitance, the Josephson energy, and the flux difference of the Josephson junction i, respectively, and $\phi_0 = h/(2e)$ is the
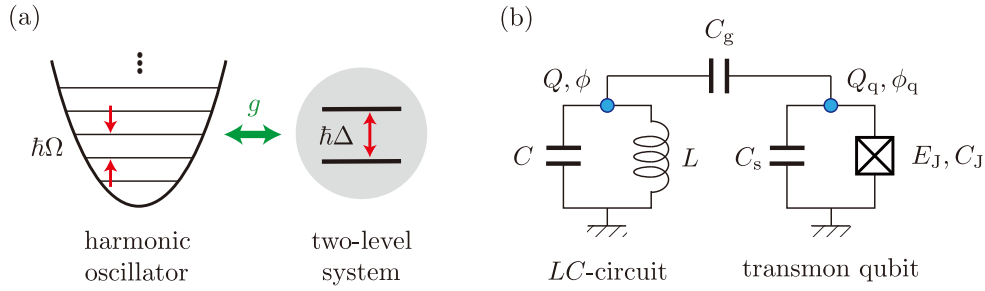
FIGURE 2.6: (a) Schematic of the quantum Rabi model and (b) its superconducting circuit. The transmon qubit is coupled capacitively to the *LC*-circuit.

flux quantum. Here, we introduce an ununiformity to the circuit by setting that the Josephson junctions $i = 1$ and 3 are identical with $E_{J,1} = E_{J,3} = E_J$ and $C_{J,1} = C_{J,3} = C_J$ and the central Josephson junction $i = 2$ has reduced parameters $E_{J,2} = \alpha E_J$ and $C_{J,2} = \alpha C_J$ with $\alpha < 1$. Since the flux through the superconducting loop is quantized due to the single-valued order parameter, the fluxes in the Josephson junctions are related to the external flux,

$$\phi_1 + \phi_2 - \phi_3 = \frac{\phi_{\text{ext}}}{2\pi}. \tag{2.27}$$

Eliminating the variable ϕ_2 by this relation and introducing new variables $\phi_\pm = (\phi_3 \pm \phi_1)/2$, the Hamiltonian can be written as [56]

$$\mathcal{H} = \frac{Q_-^2}{8(1+\alpha)C_J} + \frac{Q_+^2}{8C_J} - E_J \left[2 \cos \varphi_+ \cos \varphi_- + \alpha \cos(\phi_{\text{ext}}/\phi_0 + 2\varphi_-) \right], \tag{2.28}$$

where $\varphi_\pm = \phi_\pm/\phi_0$ is the phase variable and $Q_\pm$ are conjugate variables to the flux $\phi_\pm$. When setting the external flux to be half of the flux quantum, $\phi_{\text{ext}} = \phi_0/2$, the sum of the Josephson energies takes two minima at $\varphi_+ = 0$. The two lowest energy states correspond to clockwise or anti-clockwise circular supercurrents in the superconducting loop. The energy splitting between the two lowest energy states is induced by the quantum tunneling, which is small enough to neglect other higher energy states. Thus, the circuit for the flux qubit can be truncated into the two-level system.

2.4 Circuit-QED

We have introduced several elements of the superconducting circuits (the *LC*-circuit, the transmission line, and the superconducting qubits) so far. By combining them together, we can create an interacting quantum system without any resistive loss experimentally. This endeavor is referred to as the circuit quantum electrodynamics (circuit-QED) [12]. In this section and the next section, we briefly introduce two important models, i.e., the quantum Rabi model and the spin-boson model, both of which will be studied in the later chapters; The former is investigated from the viewpoint of heat transport in Chapter 5 and the latter in the context of the microwave scattering experiment in Chapter 3.

Quantum Rabi model

The quantum Rabi model describes a two-level system coupled to a single bosonic mode or one harmonic oscillator [57] (see Fig. 2.6 (a)). On the superconducting circuits, such a minimum hybrid system is realized by a transmon qubit capacitively coupled to an *LC*-circuit as shown in Fig. 2.6 (b). The Hamiltonian is given by

$$\mathcal{H} = -\frac{\hbar \Delta}{2} \sigma_x + \hbar \Omega b^\dagger b + \hbar g \sigma_z \left(b + b^\dagger \right) , \tag{2.29}$$

with the transition frequency of the two-level system Δ, the Pauli matrix $\sigma_{i=\{x,y,z\}}$, the resonant frequency of the bosonic mode Ω, the bosonic annihilation (creation) operator $b^\dagger$ (b), and the coupling strength g.

Although the quantum Rabi model looks very simple, the analytical solution is non-trivial [58]. When the coupling between the two-level system and the single bosonic mode is weak ($g \ll \Omega$) and the resonant frequency is in the vicinity of the transition frequency ($\Omega \sim \Delta$), we can employ the rotating wave approximation. Then, the quantum Rabi model is reduced to the Jaynes-Cummings model [59], whose Hamiltonian is given by

$$\mathcal{H} = \frac{\hbar \Delta}{2} \tau_z + \hbar \Omega b^\dagger b + \hbar g \left(\tau_+ b + \tau_- b^\dagger \right) . \tag{2.30}$$

where the Pauli matrix τ_i is obtained by rotating σ_i along y-axis by $\pi/2$, i.e., $\sigma_x = -\tau_z$, $\sigma_y = \tau_y$, $\sigma_z = \tau_x$. The Jaynes-Cummings model has been investigated for a long time in the field of quantum optics because the rotating-wave approximation is valid for usual experimental conditions. However, as the coupling increases, the counter-rotating terms cannot be neglected and therefore the rotating wave approximation breaks down. We should note that the ultra-strong coupling ($g/\Omega = 0.1 \sim 1$) or the deep-strong coupling ($g/\Omega > 1$) [60, 61] can be realized in the superconducting circuits. For example, the deep-strong coupling $g/\Omega = 1.3$ has been achieved in the recent experiment on the superconducting circuit [62]. The ultra-stong (or deep strong) coupling regime in the circuit-QED has been attracting the interest of researchers because rich physics associated with the higher-order and non-perturbative effect is expected.

Now, it is instructive to derive the Hamiltonian (2.29) of the quantum Rabi model from the superconducting circuit. Let us consider the transmon qubit with the Josephson energy E_J, the Josephson capacitance C_J, and the shunted capacitance C_s coupled to the *LC*-circuit with the inductance L and the capacitance C through a capacitance C_g, as shown in Fig. 2.6 (b). The Lagrangian of this circuit is written as

$$\mathcal{L} = \frac{C}{2} \dot{\phi}^2 - \frac{1}{2L} \phi^2 + \frac{C_q}{2} \dot{\phi}_q^2 + E_J \cos(\phi_q/\phi_0) + \frac{C_g}{2} \left(\dot{\phi} - \dot{\phi}_q \right)^2 , \tag{2.31}$$

where ϕ and ϕ_q are the fluxes at the ends of the *LC*-circuit and the transmon qubit, respectively, and $C_q = C_s + C_J$. By introducing the charge variables conjugate to the fluxes as

$$Q = \frac{\partial \mathcal{L}}{\partial \dot{\phi}} = C\dot{\phi} + C_g \left(\dot{\phi} - \dot{\phi}_q \right) , \tag{2.32}$$

$$Q_q = \frac{\partial \mathcal{L}}{\partial \dot{\phi}_q} = C_q \dot{\phi}_q + C_g \left(\dot{\phi} - \dot{\phi}_q \right) , \tag{2.33}$$

we obtain the Hamiltonian as

$$\mathcal{H} = \underbrace{\frac{1}{2C_{\text{eff}}}Q^2 + \frac{1}{2L}\phi^2}_{LC\text{-circuit}} + \underbrace{\frac{1}{2C_{\text{J,eff}}}Q_q^2 - E_J\cos(\phi_q/\phi_0)}_{\text{transmon qubit}} + \underbrace{\frac{C_g}{C_\Sigma}QQ_q}_{\text{interaction}}, \qquad (2.34)$$

where $C_\Sigma^2 = CC_g + CC_q + C_gC_q$, $C_{\text{eff}}^{-1} = [C(C_g + C_q)^2 + C_qC_g^2 + C_gC_q^2]/(2C_\Sigma^4)$, and $C_{\text{J,eff}}^{-1} = [CC_g^2 + C_q(C + C_q)^2 + C_gC^2]/(2C_\Sigma^4)$.

By quantizing the charge and flux variables of the *LC*-circuit in the same manner as Section 2.1 and replacing Q_q with $2en$, we obtain

$$\mathcal{H} = \hbar\Omega b^\dagger b + E_C n^2 - E_J\cos(\phi_q/\phi_0) + An\left(b + b^\dagger\right), \qquad (2.35)$$

where $\Omega = 1/\sqrt{C_{\text{eff}}L}$, $E_C = e^2/(2C_{\text{J,eff}})$, and $A = 2eC_g/C_\Sigma^2\sqrt{C_{\text{eff}}\hbar\Omega/2}$. Here, the constant terms have been dropped. Finally, assuming $E_J/E_C > 1$, the transmon qubit is reduced to the two-level system as explained in Section 2.3, and then we obtain the coupling strength in the model Hamiltonian (2.29) as

$$\hbar g = |e|\frac{C_g C_{\text{eff}}^{1/2}}{C_\Sigma^2}\sqrt{\hbar\Omega}\left(\frac{E_J}{2E_C}\right)^{1/4}. \qquad (2.36)$$

2.5 Spin-boson model

As described in Section 2.4, the quantum Rabi model is a two-level system coupled to a single electromagnetic mode. Here, we consider a two-level system coupled to many electromagnetic modes (harmonic oscillators), which is known as the spin-boson model [16, 17]. The spin-boson model is one of the most fundamental models for open quantum systems. The description of the environment using harmonic oscillators was originally considered in the context of the Brownian motion [63] and macroscopic quantum tunneling [64]. Subsequently, the spin-boson model was intensively studied to understand the decoherence process in the two-level system [16]. It has also been used in the fields of superconducting circuits to describe the relaxation of a qubit due to coupling to the environment [65]. The spin-boson model is described by the Hamiltonian

$$\mathcal{H} = \underbrace{-\frac{\hbar\Delta}{2}\sigma_x - \epsilon\sigma_z}_{\text{two-level system}} + \underbrace{\sum_k \hbar\omega_k b_k^\dagger b_k}_{\text{bath}} - \underbrace{\frac{\sigma_z}{2}\sum_k \hbar\lambda_k\left(b_k^\dagger + b_k\right)}_{\text{interaction}}, \qquad (2.37)$$

where $\sigma_{i=\{x,y,z\}}$ is the Pauli matrix operator, Δ and ϵ is a transition frequency and a detunning energy of the two-level system, respectively, $b_k^\dagger$ (b_k) is an annihilation (a creation) bosonic operator in the bath, ω_k is the frequency of the bosonic mode k, and λ_k is the coupling strength between the two-level system and the bosonic mode k. The properties of the bath are characterized by a spectral density

$$I(\omega) \equiv \sum_k \lambda_k^2\delta(\omega - \omega_k). \qquad (2.38)$$
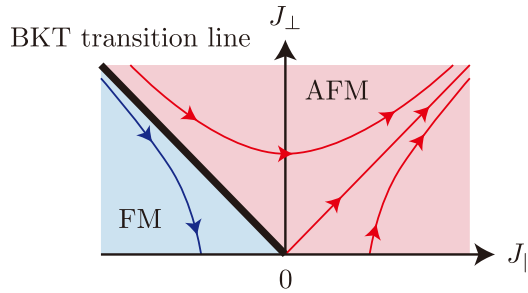
FIGURE 2.7: Renormalization flow of the anisotropic Kondo model.

The spectral density is commonly parameterized as

$$I(\omega) = 2\alpha\omega \left(\frac{\omega}{\omega_c}\right)^{s-1} e^{-\omega/\omega_c}, \tag{2.39}$$

where α is a dimensionless coupling strength and ω_c is a cutoff frequency. The property of this model strongly depends on the exponent s. The cases of $s < 1$, $s = 1$, and $s > 1$ represent sub-Ohmic, Ohmic, and super-Ohmic dissipations, respectively.

2.5.1 Kondo problem for the Ohmic case

The quantum many-body effect becomes important in the spin-boson model if the interaction between the two-level system and the environments is strong enough. This is indicated by the fact that the Ohmic spin-boson model is equivalent to the anisotropic Kondo model [16, 17]. The Kondo problem has been a central topic in condensed matter physics since the phenomenon of the electric resistivity minima in metals with magnetic impurities [66] was explained by Jun Kondo in the 1960s [67]. By using the perturbation theory, he showed that the resistivity minima are caused by the spin-exchange process between a magnetic impurity and conduction electrons in the metal [68]. Nowadays, it is known that the ground state forms a many-body singlet state between the local spin of the magnetic impurities and the conduction electrons, which is called the Kondo singlet. This has been clarified by several theoretical methods such as the poor man's scaling [69], the Wilson's numerical renormalization group [70]., the local Fermi liquid theory [71], and the exact solutions [72, 73]. The many-body effect induced by an interaction between magnetic impurities and conduction electrons is called the Kondo effect. Recently, the Kondo effect has been studied in various fields, e.g., metal surfaces [74, 75], quantum dots [76, 77], and cold atoms [78].

The Hamiltonian of the anisotropic Kondo model is given by

$$\mathcal{H} = \frac{J_\parallel}{4L}\sigma_z \sum_{k,k',s} s c^\dagger_{k,s} c_{k',s} + \frac{J_\perp}{2L} \sum_{k,k'} \left(\sigma_+ c^\dagger_{k,\downarrow} c_{k',\uparrow} + \sigma_- c^\dagger_{k,\uparrow} c_{k',\downarrow}\right) + \sum_{k,s} \epsilon_{k,s} c^\dagger_{k,s} c_{k,s}, \tag{2.40}$$

where $\sigma_\pm = (\sigma_x \pm i\sigma_y)/2$, L is a system size, and $c_{k,s}$ ($c^\dagger_{k,s}$) is an annihilation (a creation) operator of the conduction electron with the wavenumber k and the spin $s(=\uparrow,\downarrow)$, and $\epsilon_{k,s}$ is an energy of the conduction electron measured from the Fermi energy. The $J_\parallel$ term describes the spin-conserved scattering and the $J_\perp$ term describes the spin-flip one. The anisotropic Kondo model has a quantum phase transition between the ferromagnetic ($J_\parallel < 0$) and antiferromagnetic ($J_\parallel > 0$) phases at zero temperature as indicated by the renormalization group analysis (see the flow
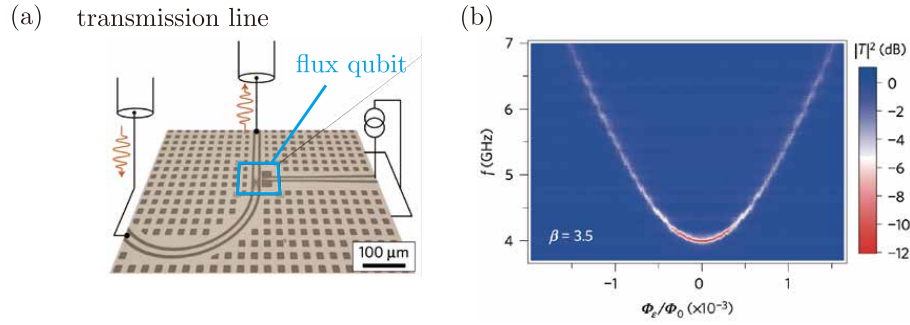
FIGURE 2.8: Microwave spectroscopy of the Ohmic spin-boson model. (a) Schematic of the spin-boson model in a superconducting circuit consisting of the flux qubit and a transmission line. (b) The microwave transmission spectrum as a function of the probe frequency f and the external flux Φ_ε. These figures are taken from Ref. [81].

diagram in Fig. 2.7). This transition belongs to the Berezinskii-Kosterlitz-Thouless (BKT) universality class [79, 80]. In the antiferromagnetic phase, the divergence of the coupling strengths along the renormalization flow indicates the formation of the Kondo singlet where the local spin is screened completely by the conduction electrons.

By using the bosonization technique [18], the anisotropic Kondo model can be mapped to the Ohmic spin-boson model with the following correspondence:

$$\frac{\Delta}{\omega_c} = \rho J_\perp \cos^2\left[\arctan\left(\frac{\pi \rho J_\parallel}{4}\right)\right], \tag{2.41}$$

$$\alpha = \left[1 - \frac{2}{\pi}\arctan\left(\frac{\pi \rho J_\parallel}{4}\right)\right]^2, \tag{2.42}$$

where ρ is a density of states of the conduction electrons. From this equivalence, the Ohmic spin-boson model also has a quantum phase transition at $\alpha = 1$, which corresponds to $J_\parallel = 0$ in the anisotropic Kondo model.

2.5.2 Recent experiment for the Ohmic case

The superconducting circuit is an ideal platform to investigate the spin-boson model using microwave spectroscopy experimentally because a typical superconducting qubit has an energy scale compatible with the microwave ($\Delta/2\pi \sim 10$ GHz). Moreover, the superconducting qubit coupled to the transmission line can be controlled precisely, and therefore we can obtain accurate experimental data.

In 2017, Pol Forn-Díaz et al. have realized a superconducting circuit described by the Ohmic spin-boson model using a flux qubit and a transmission line. They have observed clearly that the microwave transmission shows the parabolic trace (sharp dips), corresponding to the splitting tunneling frequency of the qubit, as a function of the probe frequency and the external flux, which controls the splitting tunneling frequency of the qubit (see Fig. 2.8) [81]. This sharp dip indicates that the quantum coherence of the two states of the flux qubit remains because the coupling between the flux qubit and the transmission line is weak enough ($\alpha = 0.07$). So far, the signatures of the Kondo effect have not been observed experimentally yet, but it will be done in the near future. Recently, the experimental attempts to observe many-body effects using microwave spectroscopy are actively performed [24, 82].
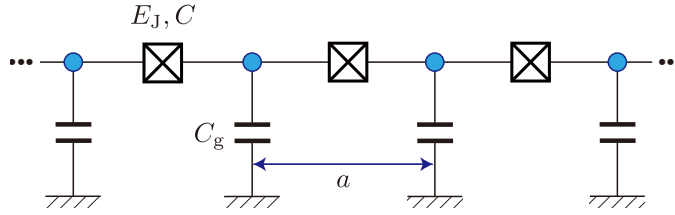
FIGURE 2.9: Josephson-junction chain consisting of circuit elements, Josephson junctions with the Josephson energy E_J and the Josephson capacitance C_J, ground capacitances C_g. The elementary cell length is a. The blue dots represent the superconducting islands.

As described above, the Ohmic spin-boson model has been studied well both theoretically and experimentally because it is related to the Kondo problem [21, 23] and the strategy of its realization has been established in the superconducting circuit using standard superconducting elements [81, 83]. Compared with the Ohmic case, there is little known about the microwave spectroscopic properties for the non-Ohmic case (the sub-Ohmic and super-Ohmic cases) in the superconducting circuits. Particularly, the sub-Ohmic spin-boson model shows a quantum phase transition and then is an important model to study the dissipative quantum transition in the well-controllable system. We study quantum critical phenomena through microwave spectroscopy in Chapter 3.

2.6 Josephson-junction chain

In the previous section, we considered the spin-boson model which is a dissipative zero-dimensional object. Here, we consider a one-dimensional object, i.e., the Josephson-junction chain, shown in Fig. 2.9. The one-dimensional Josephson-junction chain is important not only for many practical applications in superconducting quantum circuits but also for fundamental quantum physics. Actually, the Josephson-junction chain shows several many-body effects due to the Coulomb interaction between Cooper pairs.

2.6.1 Superinductor

In the linear regime, the Josephson junction behaves as the inductance, as discussed in Section 2.2, and therefore the one-dimensional Josephson-junction array can be regarded as a transmission line with the high impedance. This high-inductance low-loss element is known as a superinductor.

Using Kirchhoff's current law to the lumped-element model, we can easily obtain the dispersion relation of the Josephson-junction chain as

$$\omega(k) = \frac{v|k|}{\sqrt{1 + (kv/\Omega)^2}},$$
(2.43)

where $v = a\sqrt{2E_J E_g}/\hbar$ is the plasmon velocity, $\Omega = \sqrt{2E_J E_C}/\hbar$ is the plasma frequency, and a is the elementary unit length. Here, E_J is the Josephson junction energy, $E_g = (2e)^2/(2C_g)$ is the charging energy at the ground capacitance C_g, and $E_C = (2e)^2/(2C)$ is the charging energy at the Josephson capacitance C. As shown in Fig. 2.10, for the low frequency, we obtain the linear dispersion relation, $\omega(k) \approx v|k|$. These sound-like modes are called plasmons. For typical values of
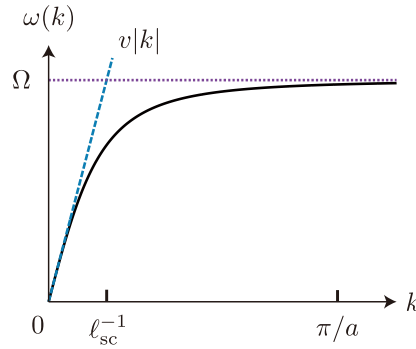
FIGURE 2.10: Dispersion relation of the Josephson-junction chain. v is the plasmon velocity, Ω is the plasma frequency, a is the elementary cell length, and ℓ_{sc} is the screening length.

$a \sim 1\ \mu\mathrm{m}$, $E_{\mathrm{J}} \sim 1\ \mathrm{GHz}$, and $C_{\mathrm{g}} \sim 0.1\ \mathrm{fF}$ [24], the plasma velocity can be estimates as $v \sim 10^6\ \mathrm{ms}^{-1}$. Compared with the velocity of light in a vacuum, the photonic modes in the Josephson-junction chain (plasmons) are slower by two orders. The ultraslow plasmons lead to a high impedance $Z \sim 10\ \mathrm{k\Omega}$ for the Josephson-junction chain. As in the vacuum quantum electrodynamics, quantum fluctuations of fields in the Josephson-junction chain are controlled by the effective fine structure constant $\alpha = Z/R_{\mathrm{Q}}$, where $R_{\mathrm{Q}} = h/(2e)^2 \approx 6.5\ \mathrm{k\Omega}$ is the resistance quantum for Cooper pairs [84]. While in the vacuum quantum electrodynamics, the fine structure constant is small ($\alpha = 1/137$ corresponding to $Z \approx 377\ \Omega$), the Josephson-junction chain can have a large effective fine constant α is of the order of 1. Thus, the Josephson-junction chain can achieve a one-dimensional superconducting element with strong quantum fluctuations.

When focusing on the low-frequency modes with the linear dispersion relation, we need to introduce the ultraviolet cutoff. It is the plasma frequency at which the dispersion relation becomes flat $\omega(k) \approx \Omega$ as shown in Fig. 2.10. This means that the plasmon does not propagate through the Josephson-junction chain due to the charge screening by the surrounding medium. Moreover, there is another cutoff scale that comes from the discreteness of the Josephson-junction chain where elementary circuits are located with the spacing of a. The shortest wavelength is $\lambda = 2a$ which means that the plasmons oscillate with π between the nearest-neighbor cells and corresponds to $k = 2\pi/\lambda = \pi/a$.

2.6.2 Lagrangian

In 1984, Mark Bradley and Sebastian Doniach theoretically discussed the Josephson-junction chain in their pioneering work and predicted that the Josephson-junction chain exhibits the superconductor-insulator transition (SIT) at zero temperature [30]. This phase transition is driven by the competition between the charge fluctuation and the phase fluctuation and belongs to the Berezinski–Kosterlitz–Thouless (BKT) universality class. For $E_{\mathrm{J}} \ll E_{\mathrm{g}}$, the Josephson-junction chain becomes an insulator because the charge fluctuation is strongly suppressed by the Coulomb blockade. On the contrary, for $E_{\mathrm{J}} \gg E_{\mathrm{g}}$, the Josephson-junction chain is in the superconducting phase due to large charge fluctuation.

The Lagrangian for the one-dimensional Josephson-junction chain of the length d is given by

$$\mathcal{L} = \int_0^d dx \left\{ \frac{\hbar}{2\pi K v} \left[\dot{\theta}(x,t) \right]^2 - \frac{\hbar v}{2\pi K} \left[\partial_x \theta(x,t) \right]^2 + \frac{\Lambda}{a} \cos \left[2\theta(x,t) \right] \right\}, \tag{2.44}$$

where $\theta(x,t)$ is a local field associated with the accumulated charge, i.e., $\rho(x,t) = -\hbar/(2e)\partial_x\theta(x,t)$ is the density of the Cooper pairs, and $K = \pi\sqrt{E_J/(2E_g)}$ is the Luttinger parameter (for a detailed derivation, see Appendix B). At the transmon limit ($E_J \gg E_C$), the quantum phase slip amplitude is written as [85, 86]

$$\Lambda = \frac{8}{\sqrt{\pi}} \left(2E_J^3 E_C \right)^{1/4} e^{-\sqrt{32E_J/E_C}}. \tag{2.45}$$

Note that, to derive the Lagrangian (2.44), we have used the continuous approximation which is valid for small ground capacitance $C_g \ll C$ (or $E_g \gg E_C$), corresponding to the large charge screening length $\ell_{sc} = a\sqrt{C/C_g} \gg a$ [87]. The Lagrangian for the Josephson-junction chain (2.44) is nothing but the sine-Gordon model [32]. The Luttinger parameter is related to the low-frequency impedance of the chain as $K = R_Q/(2Z)$. Namely, it is also related to the fine structure constant as $\alpha = 1/(2K)$. This relation indicates that the Luttinger parameter controls the quantum fluctuations of the Josephson-junction chain. Since the Josephson-junction chain can realize a large fine structure constant in the experiment [88], the Josephson-junction chain provides an appropriate platform to investigate the property of modes in the insulating phase experimentally [89]. In this thesis, we focus on the classical limit $K \ll 1$ ($E_J \ll E_g$) in which the Josephson-junction chain is in the deep insulating phase.

We summarize the magnitude relation between three characteristic energy scales, i.e., the Josephson energy E_J, the charging energy at the ground capacitance E_g, and the charging energy at the Josephson capacitance E_C, in this thesis:

- $E_J \ll E_g$ $\cdots$ Classical limit ($K \ll 1$). The charge fluctuation is frozen and the Josephson-junction chain is in the deep insulating phase.

- $E_C \ll E_J$ $\cdots$ Transmon limit. The energy spectrum is nearly harmonic and each energy band is narrow. The amplitude of quantum phase slips is exponentially small ($\Lambda \ll \Omega$).

- $E_C \ll E_g$ $\cdots$ Long-range Coulomb interaction ($\ell_{sc} \gg a$). The ground capacitance is small ($C_g \ll C$).

In a typical experiment [88], we can confirm that the above conditions are satisfied; $E_J/E_C \sim 20$ and $E_C/E_g \sim 10^{-4}$.

2.6.3 Superconductor-insulator transition

The sine-Gordon model (2.44) is one of the most studied models of one-dimensional field theory [32]. It is well known that the sine-Gordon model processes a quantum phase transition at $K = 2$ between massless (the gapless spectrum; $K > 2$) and massive (the gapped spectrum; $K < 2$) phases by changing the Luttinger parameter K, and it belongs to the BKT universality class. This BKT-type quantum phase transition corresponds to the SIT in the Josephson-junction chain. In Fig. 2.11, we show the renormalization group flow diagram of the sine-Gordon model on the m-K plane, where $m = 2\pi\sqrt{2\Lambda E_J}/\hbar$ is the mass. At $K < 2$, the cosine term in the
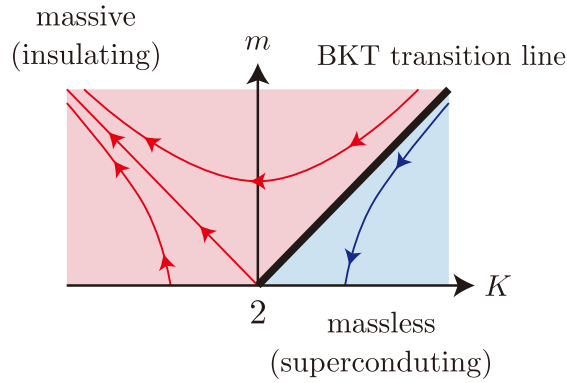
FIGURE 2.11: Flow diagram of the sine-Gordon model at zero temperature.
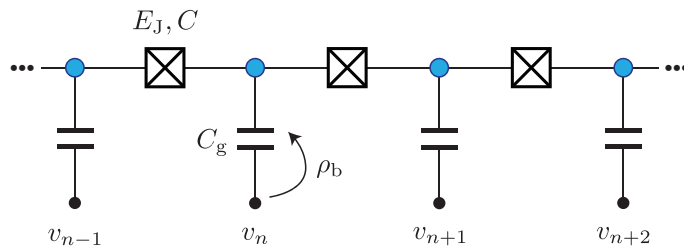
FIGURE 2.12: Josephson-junction chain with the disorder via random offset charges induced by random gate voltages v_n.

sine-Gordon model (2.44) is relevant and then the sine-Gordon model is always in the massive phase ($m \to \infty$). This phase corresponds to the insulating phase in the Josephson-junction chain. At $K > 2$, there are two fates. If the mass is larger than a critical mass m_c, the sine-Gordon model is in the massive phase (the insulating phase). If $m < m_c$, the cosine term becomes irrelevant and the sine-Gordon model is in the massless phase ($m \to 0$), which corresponds to the superconducting phase in the Josephson-junction chain. Then, the Josephson-junction chain can be effectively described by the Luttinger liquid, for which the charge density wave (CDW) can propagate ballistically [32].

2.7 Disordered Josephson-junction chain

In realistic systems, the disorder is inevitable and plays an important role in the Josephson-junction chain. Among various types of disorder [90], the most common and significant type of disorder is the random offset charges via the ground capacitance (see Fig. 2.12).

2.7.1 Random offset charges

In the presence of the random offset charges, the charging energy at the ground capacitances (B.5) is modified as

$$E_{\text{Coulomb}} = \int_0^d dx \, a E_g \left[\partial_x q(x,t) - \rho_b(x) \right]. \tag{2.46}$$

Here, $\rho_b(x)$ is the time-independent density of coarse-grained offset charges with short range correlations $\langle \rho_b(x)\rho_b(y)\rangle \propto \delta(x-y)$, where $\langle \cdots \rangle$ indicates disorder averaging. Note that there are three characteristic timescales; the time scale of offset charge fluctuation τ_c, that of the plasmon propagation $\tau_{plasmon}$, and that of experimental measurement τ_{exp}. In the experiment, the timescale for the variation of the configuration of the offset charges is $\tau_c \sim 1$ min [91]. Then, the timescale for scrambling the random offset charges in the Josephson-junction chain can be estimated as $\tau_c/N \sim 0.05$ sec, which is much larger than $\tau_{plasmon}$. Therefore, we can assume that the random offset configuration is static in all subsequent calculations, i.e., the density of states of the random offset charges is independent of time. On contrary, the time for gathering and averaging each experimental data, τ_{exp}, is sufficiently longer than τ_c/N, which justified that observables are given by the disorder averaged values with respect to the random offset charge configuration.

Now, by introducing a phase field of the quantum phase slip amplitude (the Aharonov-Casher phase) [92, 93]

$$\chi(x) = 2\pi \int^x dy\, \rho_b(y),\tag{2.47}$$

the total Lagrangian is expressed by the random phase sine-Gordon model:

$$\mathcal{L} = \int_0^d dx \left\{ \frac{\hbar}{2\pi Kv} \left[\dot{\theta}(x,t)\right]^2 - \frac{\hbar v}{2\pi K} \left[\partial_x\theta(x,t)\right]^2 + \frac{\Lambda}{a} \cos\left[2\theta(x,t) + \chi(x)\right] \right\}.\tag{2.48}$$

The random phase field is characterized by vanishing average,

$$\langle \cos\chi(x)\rangle = \langle \sin\chi(x)\rangle = 0,\tag{2.49}$$

and variance,

$$\sigma^2 = \int_0^d dx\ \langle \cos\chi(x)\cos\chi(0)\rangle = \int_0^d dx\ \langle \sin\chi(x)\sin\chi(0)\rangle.\tag{2.50}$$

2.7.2 Superfluid-Bose glass transition

Even when the random offset charges exist in the Josephson-junction chain, the SIT still occurs. However, in this case, the insulating phase becomes a compressible state, which is called Bose glass [31], instead of the incompressible Mott insulating state realized in the absence of disorder. The disorder reduces the effect of the quantum phase slips.

In 1988, Thierry Giamarchi and Heinz-Jürgen Schulz treated the one-dimensional bosonic disordered model perturbatively and provided the renormalization group equations (the Giamarchi-Schulz scaling) [31]:

$$\frac{dK}{dl} = -\frac{K^2}{2}D, \quad \frac{dD}{dl} = (3-2K)D,\tag{2.51}$$

where D describes the evolution of the quantum phase slip probability. The Giamarchi-Schulz scaling (2.51) indicates that the transition between the superfluid and Bose glass occurs at $K_c = 3/2$, which corresponds to $E_g = (2\pi^2/9)E_J$ and $Z \sim 2.2$ kΩ.
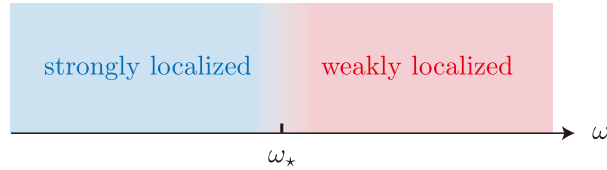
FIGURE 2.13: Two frequency regimes in the disordered Josephson-junction chain in the deep insulating phase ($K \ll 1$); the strongly localized ($\omega \ll \omega_\star$) and weakly localized ($\omega \gtrsim \omega_\star$) regimes. In the strongly (weakly) localized regimes, the collective pinning effect is strong (weak).

2.7.3 Classical limit

In the classical limit ($K \to 0$), the kinetic term in the total Lagrangian (2.48) can be neglected. Then, the disordered Josephson-junction chain is reduced to a problem for the interplay of elasticity and disorder that is equivalent to that of the pinning CDW [94].

Now, we introduce the Larkin length $R_\star$ [95, 96, 97] on which the static spatial order is destroyed. For the field variable variation in the length scale of R, the elastic energy and the pinning energy are estimated $\sim \hbar v/(KR)$ and $\sim \Lambda\sqrt{R/a}$, respectively. We further incorporate quantum fluctuations due to the quantum phase slips by replacing Λ with the renormalized phase slip amplitude $\Lambda(R/\ell_{sc})^{-K}$. Then, the generalized Larkin length [98] is defined as the length scale at which the elastic energy and the pinning energy are compatible:

$$R_\star = \left(\frac{\hbar v}{2\pi K \Lambda \sigma} \right)^{2/(3-2K)} . \tag{2.52}$$

Its corresponding frequency $\omega_\star = v/R_\star$ is called the Larkin frequency. The divergence of the Larkin length (2.52) at $K = 3/2$ indicates the superfluid-Bose glass transition.

Elastic properties on a length scale shorter than the Larkin length ($R \lesssim R_\star$) are not much affected by the collective pinning. This regime corresponds to excitations with high frequencies $\omega \gtrsim \omega_\star$, leading to the almost-ballistic propagation of plasmons (see Fig. 2.13). On the contrary, at low frequencies $\omega \ll \omega_\star$, the collective pinning effect due to the disorder drastically changes the excitation spectrum of the system. In this regime, the density of plasmon modes is determined by the statistics of distinctive configurations of disorder, which leads to the strong suppression of the density of modes at low frequencies as [99, 100, 101, 102]

$$\nu(\omega) \propto \omega^4, \tag{2.53}$$

for a long chain ($d \gg R_\star$).

We note that the collective pinning regime corresponds to $R_\star \gg \sigma^2$ in the classical limit. Therefore, one may cross over from the collective pinning regime to the individual pinning regime by increasing the quantum phase slip amplitude Λ. When we go beyond the classical limit ($K \ll 1$), it is known that quantum fluctuations due to the effect of a finite K increase the Larkin length [103].
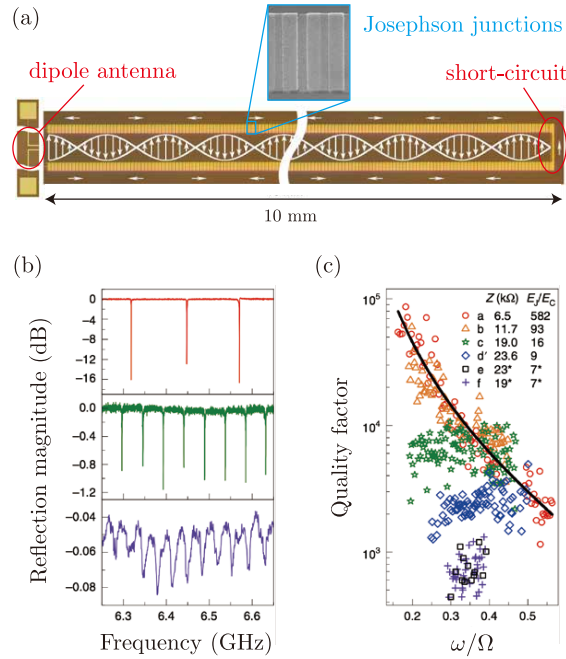
FIGURE 2.14: (a) A Josephson-junction chain. Two chains consisting of more than 33,000 Josephson junctions are spaces parallel closely. At the right end, the short-circuit is terminated and, at the left end, a dipole antenna is connected. (b) The frequency of the reflection magnitude for different devices. The Luttinger parameters are $K = 0.5$ (red), 0.171 (green), and 0.171 (purple). The ratios of the Josephson energy and the charging energy are $E_J/E_C = 582$ (red), 16 (green), and 7 (purple). (c) The frequency dependence of the quality factor for various devices. These figures are taken from Ref. [89].

2.7.4 Recent experiment

We introduce a recent experiment on ac transport through the disordered Josephson-junction chain. Even in the deep insulating phase, ac current can flow like a superconductor for $\omega \gg k_B T/\hbar$. Nevertheless, we can observe traces of insulators in the frequency dependence of the ac transport. By varying the probe frequency, the interaction can be controlled effectively in the sense of the renormalization group.

Recently, Roman Kuzmin et al. have investigated the scattering reflection off a Josephson junction using microwave spectroscopy to reveal the insulating states for $K < 3/2$ [89]. They have fabricated a long double-chain consisting of more than 33,000 junctions, as shown in Fig. 2.14 (a). When the ground capacitance of the superconducting islands is much smaller than the junction capacitance, the double-chain can be mapped into a single-chain problem by considering only asymmetric modes coupled to a dipole antenna [90]. By performing the microwave spectroscopic measurement for this Josephson-junction chain, they obtained the reflection magnitude as a function of frequency for different devices, as shown in Fig. 2.14 (b). At $K \simeq 0.5$ and $E_J/E_C \simeq 500$ (red color), we can observe the well-resolved plasmon spectrum and no signature of the insulating states despite in a smaller K than the insulator transition value, $K_c = 3/2$. We define a quality factor by the ratio of the mode frequency to its line width. As the frequency decreases, the quality factor grows and reaches a high value $\sim 10^5$, as shown in Fig. 2.14 (c). This large quality factor can be explained by the dielectric loss in the Josephson-junction capacitance (solid line

in Fig. 2.14 (c)). On contrary, at $K \simeq 0.171$ and $E_J/E_C \simeq 7$ (purple color), the well-resolved plasmons do not appear. Instead of them, we can observe the inhomogeneous broadening of the standing waves after disorder averaging in the reflection magnitude. This inhomogeneous broadening, which is caused by the pinning effect of the CDW, is a signature of the insulating phase. It is remarkable that, opposite to the well-resolved plasmon region, the quality factor decreases as the frequency is lowered. This characteristic behavior of the quality factor is observed in the insulating states. Actually, in the limit of $\omega \to 0$, the quality factor is expected to approach zero, indicating strong suppression of the dc transport. Finally, we note that the device showing the signature of the insulating phase indeed has large dc resistance of the order of 1 MΩ, which is inconsistent with a superconductor.

Recently, Manuel Houzet and Leonid Glazman have theoretically clarified the collective pinning effect of the CDW through the microwave reflection off the Josephson junction chain in the deep insulating phase [98]. However, since the reflection is related to the local density of modes at the edge of the chain, little is known about the statistical properties of plasmon waves traveling along the entire chain. Moreover, from the reflection, we cannot distinguish the forward and backward scatterings.

In Chapter 4, we investigate the transmission of a long Josephson-junction chain in the deep insulating phase and discuss the contributions of the forward and backward scatterings as well as the statistics of the transmission [40].

2.8   Quantum heat transport

Finally, we introduce recent studies on quantum heat transport in superconducting circuits, which have been stimulated by the development of the technology of calorimeters in the last decade [33, 34, 35]. The superconducting circuit is also a useful platform to study quantum heat transport because of flexible designing and fine-tuning by external fields. In the superconducting circuit, a circuit element (e.g., a superconducting qubit, a superconducting resonator, or their hybridized circuit) mediates heat by microwave photons between two photon baths (e.g., transmission lines). Below, we introduce two recent experiments on quantum heat transport through a resonator-qubit-resonator assembly.

In 2018, Jukka Pekola's group has observed tunable heat transport through a resonator-qubit-resonator assembly as a quantum heat valve [104] (see Fig. 2.15). Two resonators have identical resonant frequencies $f_r = 6.4$ GHz and are coupled to each other via a transmon qubit, whose splitting frequency f_q can be controlled by external magnetic flux Φ, with the coupling strength g. To study heat transport, the two resonators are terminated by normal-metal resistors acting as heat baths with the coupling strength γ, as shown in Fig. 2.15. When treating this circuit, there are two regimes, i.e., the quasi-Hamiltonian (global) regime (Fig. 2.15 (a); $\gamma \ll g$) and the non-Hamiltonian (local) regime (Fig. 2.15 (b); $\gamma \gg g$). This separation is associated with the location of the Heisenberg cut between the classical and quantum worlds [105]. In the quasi-Hamiltonian (QH) regime, the hybridized system composed of the qubit and the resonators couples to the bare heat baths. Since the hybridized system shows the multilevel structure, the power is affected strongly by this multilevel structure as indicated by the QH model in Fig. 2.15 (a). In the non-Hamiltonian regime, the qubit is coupled to dissipative resonators whose spectral density is Lorentzian centered around the resonance frequency f_r. Here, the heat current flows only for $f_q = f_r$, and thus the system acts as the quantum heat valve. In the bottom panel of Fig. 2.15 (b), we show the experimental (left side) and
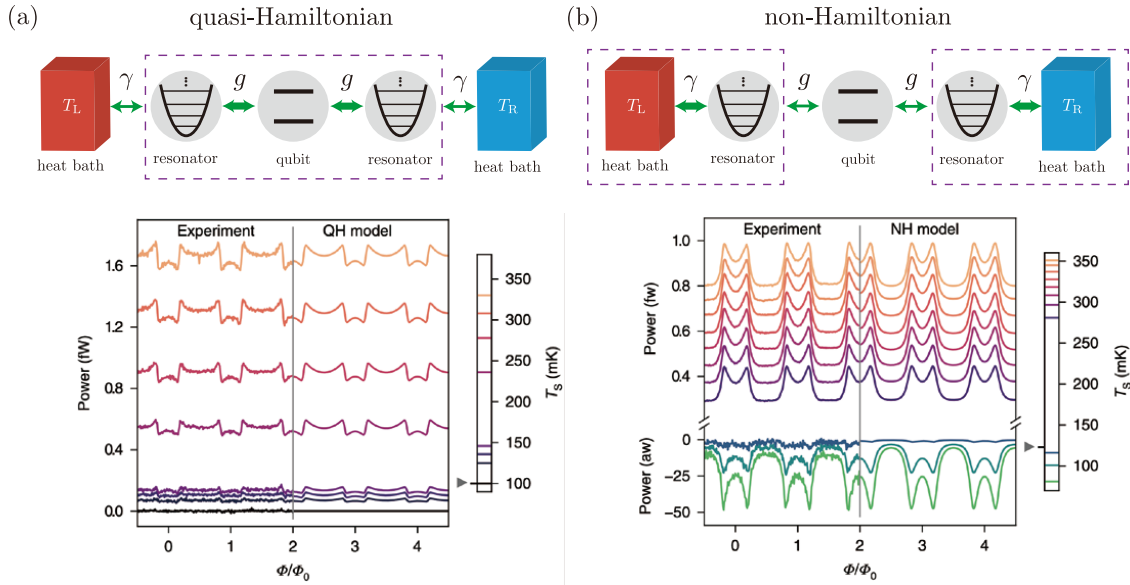
FIGURE 2.15: Quantum heat valve. A transmon qubit (two-level system) is capacitively embedded between two superconducting transmission lines (harmonic resonators). Each transmission line is terminated by a normal-metal resistor (heat bath). Panels (a) and (b) show the schematics of the model (top panels) and the external flux dependence of the heat current flowing into the right (drain) heat bath for different left (source) heat bath temperatures (lower panels) in the quasi-Hamiltonian (global) and non-Hamiltonian, respectively. The data plots are taken from Ref. [104].

theoretical (right side) results for the power as a function of the external flux for different temperatures. It is observed that the power has several Lorentzian peaks centered at fluxes corresponding to $f_q = f_r$. In both of the quasi-Hamiltonian and non-Hamiltonian regimes, the theoretical calculation shows good agreement with the experimental results.

Moreover, by breaking the symmetry of the circuit and using the non-linearity of the central element, the photonic heat rectification has been demonstrated [106] in a similar circuit to that in Ref. [104] (see Fig. 2.15). As shown in Fig. 2.16 (a), a transmon qubit is coupled to two unequal harmonic resonators, whose frequencies are 2.8 GHz and 6.7 GHz, terminated by heat baths. In the same way as the quantum heat valve, the splitting tunneling frequency of the transmon qubit can be tuned by the external flux. Fig. 2.16 (b) shows the external flux dependence of the heat current in forward (purple lines) and backward (green lines) directions for different three temperatures. The forward direction corresponds to the flow from the left bath to the right bath when $T_L = T_R + |\Delta T|$, while the backward direction corresponds to the flow in the opposite direction when $T_L = T_R - |\Delta T|$. In Fig. 2.16 (c), we show that, from the data in Fig. 2.16 (b), the external flux dependence of rectification ratio, $\mathcal{R} = |P_f|/|P_b|$, where P_f and P_b are the heat currents in the forward and backward directions, respectively. From this figure, one can see that the flux-tunable photonic heat rectification achieves 10% at maximum.

Quantum heat transport has also been studied in a number of theoretical works for the last twenty years, and various quantum heat devices such as a quantum heat valve [104], a quantum rectifiers [36, 106], a quantum heat transistor [107, 108], a quantum refrigerator [109], and a quantum heat engine [110, 111, 112] have been
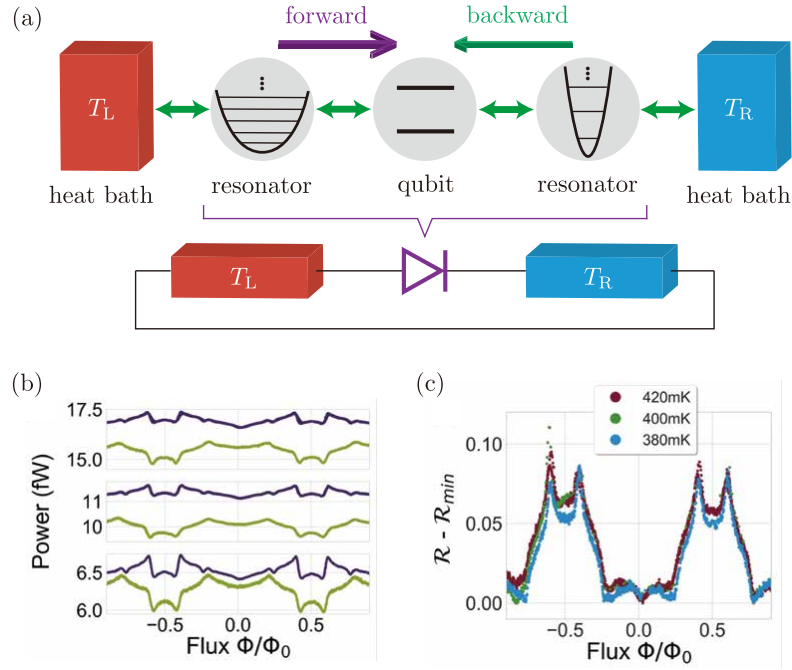
FIGURE 2.16: Quantum heat rectification. (a) Schematic of the photon diode. The circuit structure is similar to that in Fig. 2.15 but two resonators are unequal, their resonant frequencies are 2.8 GHz (left resonator) and 6.7 GHz (the right one), to break the symmetry of the circuit. The forward and reverse directions are drawn in purple and green arrows, respectively. (b) The heat current as a function of the external flux in the forward (purple lines) and backward (green lines) directions for different temperatures (380 mK, 400 mK, and 420 mK from bottom to top). (c) The external flux dependence of the rectification ratio from data in panel (b), where it is subtracted by minimal value $\mathcal{R}_{\min}$. The data plots are taken from Ref. [106].

proposed. The most fundamental model for quantum heat transport is a single superconducting qubit (a two-level system) coupled to two baths described by the spin-boson model [23, 38]. However, the single superconducting qubit is too simple to work functionally as a quantum heat device. We also note that the center part of superconducting circuits in the two experiments on a resonator-qubit-resonator assembly, which are explained in the previous two paragraphs, looks like the quantum Rabi model introduced in Section 2.4. We point out that little is still known about quantum heat transport through a resonator-qubit-resonator assembly in the ultra-strong (or deep-strong) coupling regime.

In Chapter 5, we consider quantum heat transport through a superconducting qubit embedded between two harmonic resonators, which is described by the quantum Rabi model. We show that the heat transport becomes sensitive to control parameters in the ultra-strong (or deep-strong) coupling regime. This property is advantageous for the application of quantum heat devices.

Chapter 3

Microwave Scattering through a Superconducting Qubit

In this chapter, we study the microwave scattering in superconducting circuits described by the sub-Ohmic spin-boson model. First, we review quantum phase transition in the sub-Ohmic spin-boson model in Section 3.1. Next, we move to new results obtained in Ref. [39]. We present a superconducting circuit to realize the sub-Ohmic spin-boson model and formulate the microwave scattering in this circuit in Section 3.2. Using the continuous-time quantum Monte Carlo simulation introduced in Section 3.3, we show that quantum critical phenomena emerge in the frequency dependence of the microwave reflection in Section 3.4.

3.1   Sub-Ohmic spin-boson model

As described in Section 2.5, the spin-boson model is a fundamental model for describing a two-level system coupled to bosonic environments [16, 17]. We write the Hamiltonian again, which consists of three terms, the two-level system $\mathcal{H}_{\mathrm{TLS}}$, the bosonic bath $\mathcal{H}_{\mathrm{B}}$, and their interaction $\mathcal{H}_{\mathrm{I}}$,

$$\mathcal{H} = \mathcal{H}_{\mathrm{TLS}} + \sum_{\nu} \mathcal{H}_{\mathrm{B},\nu} + \sum_{\nu} \mathcal{H}_{\mathrm{I},\nu}, \tag{3.1}$$

$$\mathcal{H}_{\mathrm{TLS}} = -\frac{\hbar\Delta}{2}\sigma_x - \epsilon\sigma_z, \tag{3.2}$$

$$\mathcal{H}_{\mathrm{B},\nu} = \sum_{k} \hbar\omega_{\nu,k} b^{\dagger}_{\nu,k} b_{\nu,k}, \tag{3.3}$$

$$\mathcal{H}_{\mathrm{I},\nu} = -\frac{\sigma_z}{2} \sum_{k} \hbar\lambda_{\nu,k} \left(b^{\dagger}_{\nu,k} + b_{\nu,k} \right), \tag{3.4}$$

and the spectral density is

$$I_{\nu}(\omega) = 2\alpha_{\nu}\omega \left(\frac{\omega}{\omega_{\mathrm{c}}} \right)^{s_{\nu}-1} e^{-\omega/\omega_{\mathrm{c}}}, \tag{3.5}$$

where ν $(= \mathrm{L},~\mathrm{R})$ is the bath index and other parameters and operators are the same as Section 2.5.

In this thesis, we focus on the sub-Ohmic case $(s < 1)$, which has a second-order phase transition at zero temperature [19, 20, 113, 114, 115, 116, 117, 118]. The quantum phase transition in the sub-Ohmic spin-boson model occurs when the coupling strength between the two-state system and the environments is tuned to a critical point α_{c}. For $\alpha < \alpha_{\mathrm{c}}$, the ground state is described by a coherent superposition of two wavefunctions localized at each well of the two-level system, which is called
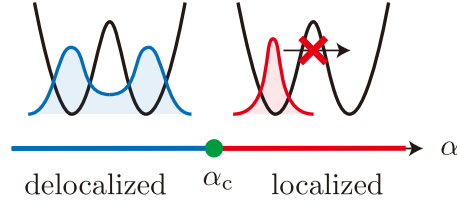
FIGURE 3.1: Schematic of the quantum phase transition in the sub-Ohmic spin-boson model at zero temperature. For $\alpha < \alpha_c$, the ground state is a superposition of two states localized at each well (the delocalized phase). For $\alpha > \alpha_c$, their coherence is broken and the state of the system is localized at one of the two wells due to the disappearance of quantum tunneling (the localized phase).
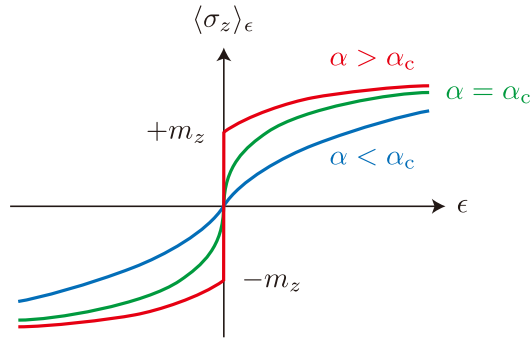
FIGURE 3.2: The detunning energy ϵ dependence of the population $\langle \sigma_z \rangle_\epsilon$ for $\alpha < \alpha_c$ (blue line), $\alpha = \alpha_c$ (green line), and $\alpha > \alpha_c$ (red line). At the critical point, $\alpha = \alpha_c$, while the population is continuous, its derivative of ϵ diverges at $\epsilon = 0$. As the coupling increasing, $\alpha > \alpha_c$, the population jumps discontinuously at $\epsilon = 0$.

as a delocalized phase (see Fig. 3.1). For the stronger coupling, $\alpha > \alpha_c$, the ground state becomes two-fold degenerate because the coherent superposition is completely broken due to the disappearance of quantum tunneling between the two wells. This phase is called a localized phase.

The population of the two-level system $\langle \sigma_z \rangle_\epsilon$ as a function of the detunning energy ϵ for $\alpha < \alpha_c$, $\alpha = \alpha_c$, and $\alpha > \alpha_c$ is shown in Fig 3.2. We regard $\langle \sigma_z \rangle_\epsilon$ as the "magnetization" in the analogy of the order parameter in a magnetic phase transition. We also define the static "spin susceptibility" by the first derivative of the magnetization at $\epsilon = 0$ as

$$\chi_0 \equiv \lim_{\epsilon \to 0} \frac{\langle \sigma_z \rangle_\epsilon}{\epsilon}, \tag{3.6}$$

where $\langle \cdot \rangle$ indicates the thermal average. The static spin susceptibility is finite for $\alpha < \alpha_c$, increases as α approaches α_c from below, and finally diverges at the critical point $\alpha = \alpha_c$. In the localized phase ($\alpha > \alpha_c$), the magnetization $\langle \sigma_z \rangle_\epsilon$ jumps discontinuously from $-m_z$ to $+m_z$ at $\epsilon = 0$, where the constant value $m_z \equiv \lim_{\epsilon \to 0+} \langle \sigma_z \rangle_\epsilon$ corresponds to the spontaneous magnetization.

The thermal equilibrium properties at the quantum critical point ($\alpha = \alpha_c$) have been studied in several theoretical works [116, 19]. The critical exponent of the

imaginary-time spin-spin correlation function, η, is defined as

$$C(\tau) \equiv \langle \sigma_z(\tau)\sigma_z(0)\rangle \sim \tau^{-\eta+1}. \tag{3.7}$$

For $0 < s \leq 0.5$, quantum critical behavior is described by the mean-field theory, giving a critical exponent [119]

$$\eta = 2 - s. \tag{3.8}$$

This critical exponent has been confirmed by the quantum Monte Carlo simulation [19] and the numerical renormalization group calculations [115, 116, 117, 20]. In contrast, for $0.5 < s < 1$, the critical exponents are non-trivial function of s [120]. So far, experimental realization of the sub-Ohmic spin-boson model has been discussed only for $s = 0.5$ using the transmission line with resistances [121, 122]. However, the sub-Ohmic bath with arbitrary s has not been discussed.

In the rest of this chapter, we propose a superconducting circuit to realize the sub-Ohmic spin-boson model with arbitrary s and investigate quantum critical phenomena from the viewpoint of the microwave scattering on that superconducting circuit [39].

3.2 Formalism for microwave scattering

In this section, we introduce a superconducting circuit to realize the sub-Ohmic spin-boson model using a charge qubit and an *RLC* transmission line and formulate the scattering problem on this superconducting circuit.

3.2.1 Circuit model

Let's consider a superconducting circuit as shown in Fig. 3.3 for a realization of the sub-Ohmic spin-boson model. In this circuit, to investigate the microwave scattering off the sub-Ohmic spin-boson model, the Ohmic bath is also weakly coupled to the two-level system as a probe system.

First, we consider a charge qubit as a two-level system. As discussed in Section 2.3, the charge qubit composed of two Josephson junctions with Josephson energies $E_{J,\nu}$ and self-capacitances $C_{J,\nu}$ ($\nu = L, R$). The charge states of the qubit is controlled by a gate voltage V_g via a gate capacitance C_g. Then, the Hamiltonian of the charge qubit is given by Eq. (2.24) with a modified charging energy $E_C = (2e^2)/C_\Sigma$ where $C_\Sigma = C_{J,L} + C_{J,R} + C_g$. Assuming small Josephson junction energies, $E_{J,L}, E_{J,R} \ll E_C$, and setting the offset charge as $n_g = 0.5$, we can reduce the superconducting circuit to the two-level system as discussed in Section 2.3, and then the Hamiltonian can be written as

$$\mathcal{H}_{\text{TLS}} = -\frac{\hbar\Delta}{2}\sigma_x - \epsilon\sigma_z, \tag{3.9}$$

where the first term describes the Josephson energy and the second term corresponds to detunning from the degenerate gate voltage $n_g = 0.5$. Here, $\Delta \equiv E_J/\hbar$ is the tunneling frequency. The Pauli operators $\sigma_{i=x,y,z}$ have a two-dimensional Hilbert space and the eigenstates of σ_z correspond to the two charge states, $|n = 0\rangle$ and $|n = 1\rangle$, in the island. In this thesis, we consider the symmetric case ($\epsilon = 0$) and use only the detunning energy to define the static susceptibility (3.6).
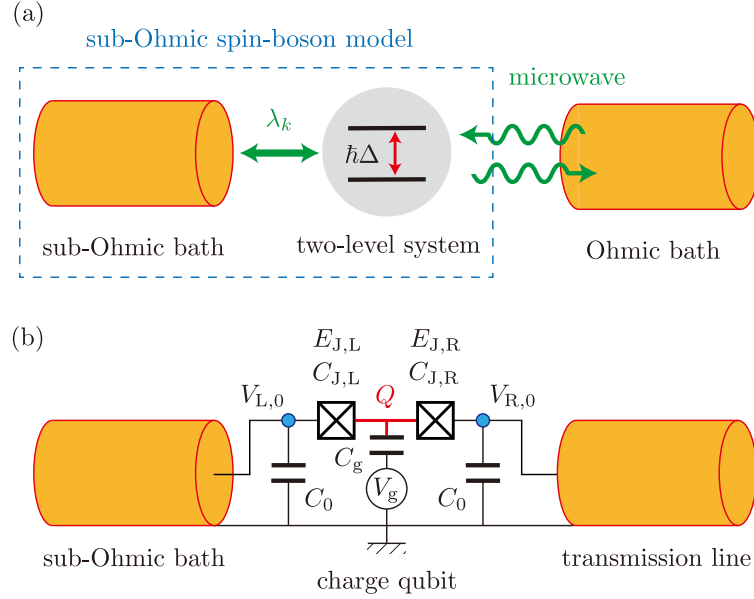
FIGURE 3.3: (a) A schematic of the model considered in this chapter. The spin-boson model, consisting of a two-level system and a sub-Ohmic bath, is coupled to an Ohmic bath as a probe. (b) A superconducting circuit realizes the model in panel (a). The two-level system and the Ohmic bath are realized by the charge qubit and the transmission line, respectively. The realization of the sub-Ohmic bath will be discussed later.

Second, we consider the sub-Ohmic bath coupled to the charge qubit, i.e., a system described by the spin-boson model with $s_L = s < 1$. Explicit construction of the sub-Ohmic bath using an *RLC* transmission line will be discussed in the next subsection. The interaction between the charge qubit and the sub-Ohmic bath can be expressed as

$$\mathcal{H}_{I,L} = \frac{eC_{J,L}}{C_\Sigma} \sigma_z V_{L,0}, \tag{3.10}$$

$$V_{L,0} = -\frac{C_\Sigma}{2eC_{J,L}} \sum_k \hbar \lambda_{L,k} \left(b_{L,k} + b_{L,k}^\dagger \right), \tag{3.11}$$

where $V_{L,0}$ is the voltage at the end of the sub-Ohmic bath (see Fig. 3.3 (b)). This form of the interaction corresponds to the system-environment coupling in the spin-boson model. Here, we introduce the retarded voltage-voltage correlation function defined by

$$G_V^R(t) \equiv -\frac{i}{\hbar} \theta(t) \langle [V_{L,0}(t), V_{L,0}(0)] \rangle_{B,L}, \tag{3.12}$$

where $\theta(t)$ is the Heaviside step function, $V_{L,0}(t) = e^{i\mathcal{H}_{B,L}t/\hbar} V_{L,0} e^{-i\mathcal{H}_{B,L}t/\hbar}$, and $\langle \cdots \rangle_{B,L}$ indicates an ensemble average with respect to the sub-Ohmic bath, $H_{B,L}$. Comparing the definition of the spectral density (2.38) and the imaginary part of the Fourier transformation of $G_V^R(t)$, the spectral density can be expressed as

$$I_L(\omega) = -\frac{1}{\pi\hbar} \left(\frac{2eC_{J,L}}{C_\Sigma} \right)^2 \text{Im} \left[G_V^R(\omega) \right]. \tag{3.13}$$

Moreover, using the linear response theory [123], the voltage-voltage correlation function, $G_V^R(\omega)$, is related to the impedance of the sub-Ohmic bath, $Z_{B,L}(\omega)$, as $G_V^R(\omega) = -i\omega Z_{sub}(\omega)$. The relation allows the spectral function to be written in terms of circuit parameters as

$$I_L(\omega) = \frac{1}{\pi\hbar} \left(\frac{2eC_{J,L}}{C_\Sigma} \right)^2 \omega \mathrm{Re}\left[Z_{B,L}(\omega) \right]. \tag{3.14}$$

Note that this expression of the spectral density using the impedance of the bath is valid for arbitrary baths.

Finally, let us consider a transmission line as an Ohmic bath. It is coupled to the two-level system weakly as a probe system for the microwave scattering. The transmission line is described by a continuum limit for a series of *LC*-circuits as discussed in Section 2.1. Here, we briefly repeat the theoretical description. The Hamiltonian of the transmission line is given as

$$\mathcal{H}_{B,R} = \int_0^d dx \left\{ \frac{1}{2c} [Q(x)]^2 + \frac{1}{2l} [\partial_x \phi(x)]^2 \right\}, \tag{3.15}$$

where c and l are the capacitance and the inductance per unit length, respectively, and d is the length of the transmission line. The charge density operator $Q(x)$ and the flux operator $\phi(x)$ at position x are conjugate to each other, $[\phi(x), Q(y)] = i\hbar\delta(x - y)$. By introducing bosonic annihilation and creation operators as

$$b_{R,k} = \frac{1}{\sqrt{\hbar\omega_{R,k}d}} \int_0^d dx\, e^{-ikx} \left[\frac{Q(x)}{\sqrt{2c}} - i\sqrt{\frac{k^2}{2l}}\phi(x) \right], \tag{3.16}$$

$$b_{R,k}^\dagger = \frac{1}{\sqrt{\hbar\omega_{R,k}d}} \int_0^d dx\, e^{+ikx} \left[\frac{Q(x)}{\sqrt{2c}} + i\sqrt{\frac{k^2}{2l}}\phi(x) \right], \tag{3.17}$$

respectively, the Hamiltonian can be rewritten in the diagonal form:

$$\mathcal{H}_{R,B} = \sum_k \hbar\omega_{R,k} b_{R,k}^\dagger b_{R,k}, \tag{3.18}$$

where $\omega_{R,k} = |k|/\sqrt{lc}$. One can easily check that the commutation relation $[b_{R,k}, b_{R,k'}^\dagger] = \delta_{k,k'}$ holds.

Since this transmission line is capacitively coupled to the charge qubit, the coupling Hamiltonian can be written as

$$\mathcal{H}_{I,R} = \frac{eC_{J,R}}{C_\Sigma} \sigma_z V_R(x = 0), \tag{3.19}$$

with the voltage in the transmission line

$$V_R(x) = \sum_k \sqrt{\frac{\hbar\omega_{R,k}}{dc}} \left(b_{R,k} e^{ikx} + b_{R,k}^\dagger e^{-ikx} \right). \tag{3.20}$$

Thus, we obtain the spin-boson-type interaction as

$$\lambda_{R,k} = -\frac{2eC_{J,R}}{C_\Sigma} \sqrt{\frac{\omega_{R,k}}{\hbar dc}}. \tag{3.21}$$
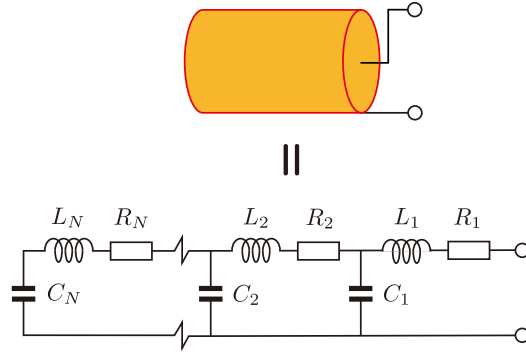
FIGURE 3.4: An *RLC* transmission line to realize the sub-Ohmic bath.

Plugging $\lambda_{R,k}$ into the definition of the spectral density (2.38), we obtain the Ohmic spectral density of the transmission line as

$$I_R(\omega) = \frac{1}{\pi\hbar}\sqrt{\frac{l}{c}}\left(\frac{2eC_{J,R}}{C_\Sigma}\right)^2 \omega = \alpha_R\omega, \tag{3.22}$$

in the limit $d \to \infty$. This means that the transmission line plays the role of the Ohmic bath, i.e., $s_R = 1$. Note that the spectral function of the transmission line can be also obtained from the general form (3.14) by substituting the impedance of the transmission line $Z_{B,R}(\omega) = \sqrt{l/c}$.

3.2.2 Realization of the sub-Ohmic bath

Here, we provide a strategy to realize the sub-Ohmic bath using an *RLC* transmission line as shown in Fig. 3.4. As mentioned in the previous subsection, the spectral density is related to the total impedance,

$$Z_L^{-1}(\omega) = Z_0^{-1}(\omega) + i\omega C_0, \tag{3.23}$$

where $Z_0(\omega)$ is the impedance of the *RLC* transmission line and C_0 is the capacitance at the end of the *RLC* transmission line close to the charge qubit. The relation (3.14) allows the spectral density of the *RLC* transmission line to be written as

$$I_L(\omega) = \frac{1}{\pi\hbar}\left(\frac{2eC_{J,L}}{C_\Sigma}\right)^2 \tilde{I}_L(\omega), \quad \tilde{I}_L(\omega) = \omega\mathrm{Re}\left[Z_L(\omega)\right]. \tag{3.24}$$

Therefore, to realize the sub-Ohmic bath, one needs to design the *RLC* transmission line with appropriately frequency-dependent impedance. By solving the recurrence relation for $j \in [1, N]$:

$$Z_0(\omega) = Z_{L,1}(\omega), \tag{3.25}$$

$$Z_{L,j}(\omega) = R_{L,j} + i\omega L_{L,j} + \frac{1}{Z_{L,j+1}^{-1}(\omega) + i\omega C_{L,j}} \tag{3.26}$$

with $Z_{L,N+1}^{-1}(\omega) = 0$, we obtain the impedance of the *RLC* transmission line, $Z_0(\omega)$, numerically.

   We first consider a simple circuit to realize the sub-Ohmic bath with $s = 0.5$. Then, we expand the circuit model for an arbitrary value of s smaller than 0.5. Finally, we mention an *RLC* transmission line for arbitrary s in the range $0 < s < 1$.
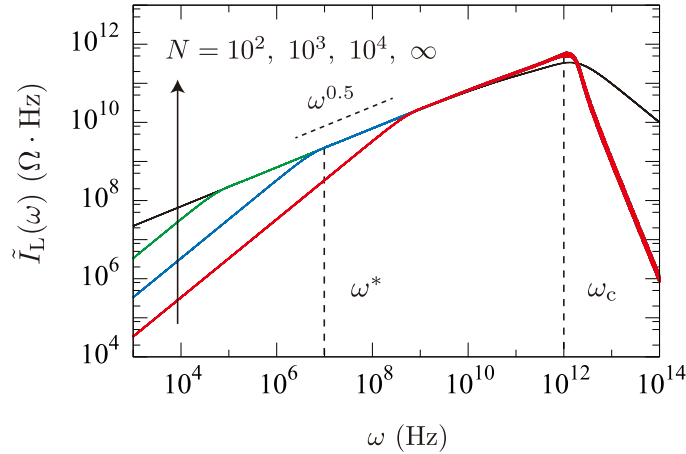
FIGURE 3.5: Spectral density of the *RLC* transmission line as a function of frequency for different N. The exponent of the spectral density is 0.5. The circuit elements are set as $R = 1$ Ω, $L = 1$ pH, $C = 1$ pF, $C_0 = 1$ pF.

(i) case for s = 0.5

Let us first consider a uniform *RLC* transmission line:

$$R_j = R, \quad L_j = L, \quad C_j = C. \tag{3.27}$$

Figure 3.5 shows the dimensionless spectral density of the *RLC* transmission line, $\tilde{I}_L(\omega)$, for $N = 10^2$, 10^3, 10^4, and ∞ by solving the recurrence relation (3.26) numerically. Here, the circuit parameters are set as $R = 1$ Ω, $L = 1$ pH, $C = 1$ pF, and $C_0 = 1$ pF. Note that the case of $N = \infty$ has been discussed in Ref. [121]. Figure 3.5 indicates that the circuit realizes the sub-Ohmic bath with $s = 0.5$ for the frequency range, $\omega^* \ll \omega \ll \omega_c$, where ω^* and ω_c are the low- and high-frequency cutoffs, respectively. From the recurrence relation in Eq. (3.26), these cutoffs can be estimated as $\omega^* = \pi^2/(N^2 RC)$ and $\omega_c = C/(RC_0^2)$, respectively, which are shown for $N = 10^3$ in Fig. 3.5. Moreover, to observe the robustness in this circuit, we added 10% relative randomness to the circuit parameters. As shown in Fig. 3.5, the fluctuation due to the randomness is not visible. Thus, this uniform *RLC* transmission line is robust to the randomness in the circuit elements.

(ii) case for 0 < s < 0.5

We next propose an *RLC* transmission line with spatial dependence circuit elements,

$$R_j = R \left(\frac{j}{N} \right)^n, \quad L_j = 0, \quad C_j = C. \tag{3.28}$$

Here, n is a positive real number. Figure 3.6 shows the dimensionless spectral density, $\tilde{I}_L(\omega)$, for $n = 2$ and $N = 10^2$, which is obtained by solving the recurrence relation (3.26) numerically. The circuit parameters are set as $R = 50$ mΩ, $L = 0$ H, $C = 0.2$ μF, and $C_0 = 0$ F. According to this figure, the present circuit realizes the sub-Ohmic bath for the frequency range of $\omega^* \ll \omega \ll \omega_c$, where ω^* and ω_c are the low- and high-frequency cutoffs, respectively. Randomness in the circuit leads to small fluctuations but does not change the overall feature of the spectral density for the case of no randomness by comparing the circuit with 10% relative randomness
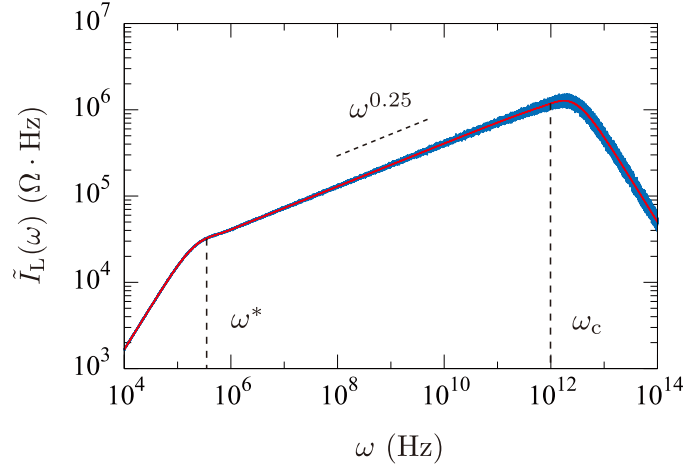
FIGURE 3.6: The frequency dependence of the spectral density of the *RLC* transmission line for $n = 2$ with the exponent 0.25. The circuit parameters are $R = 50$ mΩ, $L = 0$ H, $C = 0.2$ μF, $C_0 = 0$ F, $N = 10^2$.

(blue line) and without randomness (red line). It is noteworthy that the sub-Ohmic bath can be realized for a wider frequency range extending to $N = 10^2$, which is much less than the case for $s = 0.5$.

From Eq. (3.26), we can derive, for an arbitrary positive value of n, the spectral density as (see Appendix C for the detailed derivation)

$$\tilde{I}_{\mathrm{L}}(\omega) \propto \omega^{1/(n+2)}, \quad (\omega^* \ll \omega \ll \omega_{\mathrm{c}}). \tag{3.29}$$

This form means that the present *RLC* transmission line potentially realizes the sub-Ohmic bath with $s < 0.5$ because n is a real positive number. It is consistent with Fig. 3.6, in which the *RLC* transmission line with $n = 2$ realizes the sub-Ohmic bath with $s = 0.25$. The low- and high-frequency cutoffs are obtained as

$$\omega^* = \frac{1}{RC} \left(\frac{n}{2N} \right)^2 \left(1 + \frac{2\sqrt{2}}{n} \right)^{n+2}, \quad \omega_{\mathrm{c}} = \frac{1}{RC} \left(\frac{2N}{n} \right)^n, \tag{3.30}$$

respectively, and are shown in Fig. 3.6. Note that as n decreases, the frequency range in which the spectral density behaves as the sub-Ohmic bath becomes narrower.

(iii) case for 0 < s < 1

Finally, we discuss how to realize the sub-Ohmic spin-boson model with $0 < s < 1$. We assume that the resistances and inductances depend on the position as follows:

$$R_j = R \left(\frac{j}{N} \right)^n, \quad L_j = L \left(\frac{j}{N} \right)^p, \quad C_j = C, \tag{3.31}$$

where n and p are non-negative real numbers. From Eq. (3.26), we can derive an analytic expression of the spectral density

$$\tilde{I}_{\mathrm{L}}(\omega) \propto \omega^{2/(p+2)}, \quad (\omega^* \ll \omega \ll \omega_{\mathrm{c}}), \tag{3.32}$$

where the low-frequency cutoff, ω^*, is give by

$$\omega^* = \left[\left(\frac{p}{2N} \right)^{2(n-p)} \frac{R^{p+2}}{L^{n+2}C^{n-p}} \right]^{1/(2n-p+2)}, \tag{3.33}$$

and the high-frequency cutoff, ω_c, is a complex function of the circuit parameters. Note that although this circuit can realize the sub-Ohmic bath with an arbitrary value of s in the range of $0 < s < 1$, one needs a very large $N \gtrsim 10^5$, to achieve a sufficient frequency range where the spectral density behaves as the sub-Ohmic one.

3.2.3 Microwave scattering

As shown in Fig. 3.3 (a), an incident microwave enters from the transmission line into the charge qubit, and then the reflected microwave is allowed to propagate in the same transmission line in the opposite direction. Here, we formulate the microwave scattering using the input-output theory [124, 21, 22] and derive a relation between the reflection coefficient and the dynamic spin susceptibility of the sub-Ohmic spin-boson model within the linear response theory.

Let us begin with the total Hamiltonian

$$\mathcal{H} = \mathcal{H}_{\text{sub}} + \mathcal{H}_{\text{B,R}} + \mathcal{H}_{\text{I,R}}, \tag{3.34}$$

where $\mathcal{H}_{\text{sub}} = \mathcal{H}_{\text{TLS}} + \mathcal{H}_{\text{B,L}} + \mathcal{H}_{\text{I,L}}$ is the Hamiltonian of the sub-Ohmic spin-boson model. From the Heisenberg equation of motion, the time evolution of the annihilation operator of the transmission line is

$$\dot{b}_{\text{R},k}(t) = \frac{i}{\hbar} [\mathcal{H}, b_{\text{R},k}(t)] = -i\omega_{\text{R},k}b_{\text{R},k}(t) + i\frac{\lambda_{\text{R},k}}{2}\sigma_z(t), \tag{3.35}$$

where $\mathcal{O}(t) = e^{i\mathcal{H}t/\hbar}\mathcal{O}e^{-i\mathcal{H}t/\hbar}$. By integrating the Heisenberg equation of motion (3.35), its solution is given by [21]

$$b_{\text{R},k}(t) = e^{-i\omega_{\text{R},k}(t-t_0)}b_{\text{R},k}(t_0) + i\frac{\lambda_{\text{R},k}}{2} \int_{t_0}^{t} dt' \, e^{-i\omega_{\text{R},k}(t-t')}\sigma_z(t'), \tag{3.36}$$

where t_0 is a past time before any excitation mode reaches the two-state system. The first term represents the free time evolution in the transmission line and the second term describes the effect of the interaction between the charge qubit and the transmission line. Similarly, we obtain an alternative solution to Eq. (3.35) as

$$b_{\text{R},k}(t) = e^{-i\omega_{\text{R},k}(t-t_1)}b_{\text{R},k}(t_1) - i\frac{\lambda_{\text{R},k}}{2} \int_{t}^{t_1} dt' \, e^{-i\omega_{\text{R},k}(t-t')}\sigma_z(t'), \tag{3.37}$$

where t_1 is a future time after the entire excitation mode leaves the two-state system. The voltages of input and output modes are expressed as

$$V_{\text{in}}(t) = \sum_k \sqrt{\frac{\hbar\omega_{\text{R},k}}{dc}} \left[e^{-i\omega_{\text{R},k}(t-t_0)}b_{\text{R},k}(t_0) + \text{h.c.} \right], \tag{3.38}$$

$$V_{\text{out}}(t) = \sum_k \sqrt{\frac{\hbar\omega_{\text{R},k}}{dc}} \left[e^{-i\omega_{\text{R},k}(t-t_1)}b_{\text{R},k}(t_1) + \text{h.c.} \right], \tag{3.39}$$

respectively. Using Eqs. (3.36)-(3.39), the input and output voltages in the Fourier space relate to each other as follows:

$$\langle V_{\text{out}}(\omega) \rangle = \langle V_{\text{in}}(\omega) \rangle - i \frac{\pi \hbar C_\Sigma}{2 e C_{\text{J,R}}} I_{\text{R}}(\omega) \langle \sigma_z(\omega) \rangle, \tag{3.40}$$

where $\langle \cdot \rangle$ indicates an average with respect to the total Hamiltonian and $I_{\text{R}}(\omega)$ is linear to ω because the transmission line is Ohmic.

Assuming weak coupling between the charge qubit and the transmission line ($\alpha_{\text{R}} \ll 1$), the population $\langle \sigma_z(\omega) \rangle$ in Eq. (3.40) can be expressed within the linear response theory as

$$\langle \sigma_z(\omega) \rangle = -\frac{e C_{\text{J,R}}}{C_\Sigma} \chi_{\text{sub}}(\omega) \langle V_{\text{in}}(\omega) \rangle. \tag{3.41}$$

Here, $\chi_{\text{sub}}(\omega)$ is the Fourier transformation of the dynamic spin susceptibility of the sub-Ohmic spin-boson model defined as

$$\chi_{\text{sub}}(t) \equiv \frac{i}{\hbar} \theta(t) \langle [\sigma_z(t), \sigma_z(0)] \rangle_{\text{sub}}, \tag{3.42}$$

where $\langle \cdot \rangle_{\text{sub}}$ indicates an average to the Hamiltonian of the sub-Ohmic spin-boson model $\mathcal{H}_{\text{sub}}$. Hence, from Eqs. (3.40) and (3.41), we obtain a relation between the reflection coefficient and the dynamic spin susceptibility as

$$r(\omega) \equiv \frac{\langle V_{\text{out}}(\omega) \rangle}{\langle V_{\text{in}}(\omega) \rangle} = 1 + i \frac{\pi \hbar}{2} I_{\text{R}}(\omega) \chi_{\text{sub}}(\omega). \tag{3.43}$$

This form indicates that one can calculate the reflection coefficient once one gets the dynamic spin susceptibility of the sub-Ohmic spin-boson model. In this thesis, we perform the continuous-time quantum Monte Carlo simulation to obtain the dynamic spin susceptibility numerically.

3.3   Continuous-time quantum Monte Carlo method

In this section, we explain the continuous-time Monte Carlo (CTQMC) algorithm [125] and how to calculate the dynamic spin susceptibility of the sub-Ohmic spin-boson model.

3.3.1   Kink representation

First, let us write the partition function of the spin-boson model in the kink representation. The partition function is given in the imaginary time path integral form as [17, 19]

$$Z = \text{tr} \left[e^{-\beta \mathcal{H}} \right] = \int \mathcal{D} \sigma_z(\tau) \, e^{-\mathcal{S}[\sigma_z(\tau)]}, \tag{3.44}$$

$$\mathcal{S}[\sigma_z(\tau)] = -\frac{1}{4} \int_0^\beta d\tau \int_0^\tau d\tau' \, \sigma_z(\tau) K(\tau - \tau') \sigma_z(\tau'), \tag{3.45}$$

where $\sigma_z(\tau)$ is a spin path along the imaginary-time axis, $\mathcal{D}\sigma_z(\tau)$ is an integral measure for all possible paths $\sigma_z(\tau)$, $\mathcal{S}[\sigma_z(\tau)]$ is an influence function, and $K(\tau)$ is a

kernel defined as

$$K(\tau) = \int_0^\infty d\omega \, I(\omega) \frac{\cosh\left[\omega(\beta/2 - \tau)\right]}{\sinh(\beta\omega/2)}, \tag{3.46}$$

where $I(\omega)$ is the spectral density. Note that the kernel has the symmetric property, $K(\tau) = K(\beta - \tau)$, and the asymptotic form $K(\tau) \sim \tau^{-(1+s)}$ for $\omega_c^{-1} \ll \tau \ll \beta/2$.

Here, we move from the spin representation (3.44) to the kink representation. The spin path $\sigma_z(\tau)$ is characterized by an alternative configuration of kinks (jumps from $\sigma_z = -1$ to $\sigma_z = +1$; $q_i = +1$) and anti-kinks (opposite jumps; $q_i = -1$) and their positions $\tau_{i\in[1,2n]}$. Thus, the derivative of the spin path can be rewritten in terms of the kink variable q_i as

$$\frac{d\sigma_z(\tau)}{d\tau} = \sum_{i=1}^{2n} 2q_i\delta(\tau - \tau_i), \tag{3.47}$$

where n is the number of the pairs of kinks and anti-kinks. By plugging this expression into Eq. (3.44), we obtain the partition function in the kink representation as follows:

$$Z = \sum_{n=0}^{\infty} \left(\frac{\Delta}{2}\right)^{2n} \int_0^\beta d\tau_{2n} \int_0^{\tau_{2n}} d\tau_{2n-1} \cdots \int_0^{\tau_2} d\tau_1 \, \exp\left[\sum_{i,j}^{2n} q_iq_jW(\tau_i - \tau_j)\right], \tag{3.48}$$

where $W(\tau)$ is obtained from $W''(\tau) = -K(\tau)$ and reads

$$W(\tau) = \int_0^\infty d\omega \, \frac{I(\omega)}{\omega^2} \frac{\cosh(\beta\omega/2) - \cosh\left[\omega(\beta/2 - \tau)\right]}{\sinh(\beta\omega/2)}. \tag{3.49}$$

3.3.2 Calculation algorithm

We apply the CTQMC method [125] to the partition function of the spin-boson model in the kink representation. The CTQMC algorithm in this thesis employs a cluster-flip update similar to the Swendsen–Wang cluster algorithm [126]. This algorithm allows us to overcome the critical slowing down, namely, the problem that the correlation time diverges near the critical point of second-order phase transition. The cluster-flip update is constructed as follows [19] (see Fig. 3.7):

1. Insert new vertices with Poisson statics, $P(\Delta\tau) = \Gamma e^{-\Gamma\Delta\tau}$ with mean value $\Gamma^{-1} = 2/\Delta$.

2. Connect two segments (the line segments between neighboring vertices), s_i and s_j, with the probability

   $$p[s_i, s_j] = 1 - \delta_{\sigma_z(s_i),\sigma_z(s_j)} \left[1 - e^{-2A}\right], \tag{3.50}$$
   $$A = W(\tau_{i-1} - \tau_{j-1}) - W(\tau_{i-1} - \tau_j) - W(\tau_i - \tau_{j-1}) + W(\tau_i - \tau_j), \tag{3.51}$$

   where $\sigma_z(s_i)$ is the value of σ_z in the segment s_i, and positions of the vertices at the two edges of the segment s_i are denoted by τ_{i-1} and τ_i, respectively.

3. Flip each segment cluster with probability $1/2$.

4. Remove the redundant vertices within segments.
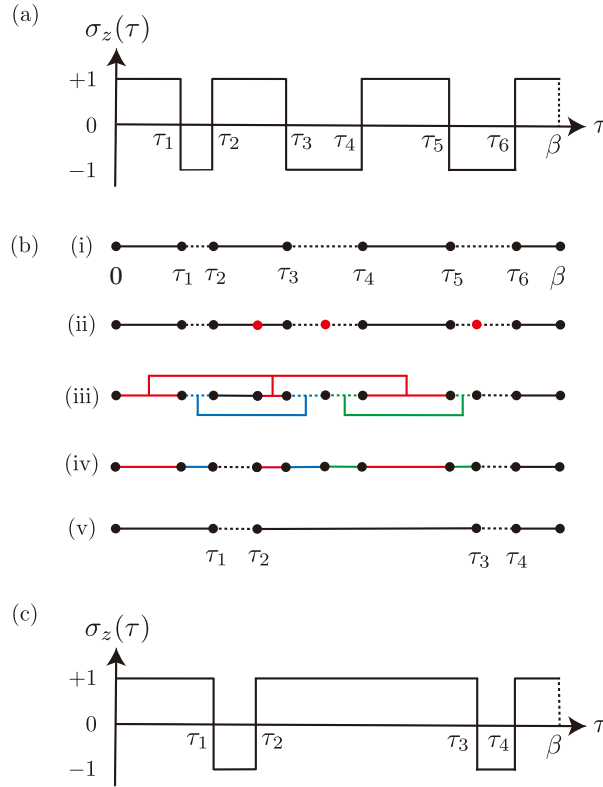
FIGURE 3.7: The configurations along the imaginary-time axis and the CTQMC update process: (a) An initial configuration in the spin representation, (b-i) the kink representation of panel (a), (b-ii) insertion of new cuts using the Poisson distribution, (b-iii) connection of segments with the probability (3.50), (b-iv) flipping each cluster with probability $1/2$, (b-v) removal of redundant cuts, and (c) the final configuration in the spin representation after the update.

The Monte Carlo data presented in this thesis represent averages over 10^5-10^6 cluster updates.

By using the CTQMC method, we can evaluate the Fourier transformation of the spin correlation function $C(\tau) = \langle \sigma_z(\tau)\sigma_z(0) \rangle_{\text{sub}}$ defined on the imaginary-time axis as follows:

$$C(i\omega_n) = \int_0^{\hbar\beta} d\tau\, e^{i\omega_n \tau} C(\tau) = \frac{1}{\hbar\beta\omega_n^2} \left\langle |\xi(i\omega_n)|^2 \right\rangle, \tag{3.52}$$

where $\langle \cdot \rangle$ denotes the CTQMC sampling average, $\omega_n = 2\pi n/(\hbar\beta)$ is the Matsubara frequency, and $\beta = 1/(k_B T)$ is the inverse temperature. Here, $\xi(i\omega_n)$ is the Fourier transformation of the derivative of the spin path, $\xi(\tau) = d\sigma_z(\tau)/d\tau$, and can be expressed in the kink representation, using Eq. (3.47), as

$$\xi(i\omega_n) = \sum_{j=1}^{2n} 2(-1)^j e^{i\omega_n \tau_j}. \tag{3.53}$$

Then, we evaluate the reflection coefficient numerically in the following way:

1. Get a set of vertex position $\{\tau_j\}$ at each configuration.

2. Calculate the Fourier transformation of the spin correlation function, $C(i\omega_n)$, using Eqs. (3.52) and (3.53).

3. Perform the analytical continuation numerically using the Padé approximation [127] and then obtain the Fourier transformation of the dynamic spin susceptibility,

$$\chi_{\text{sub}}(\omega) = C(i\omega_n \to \omega + i\delta). \tag{3.54}$$

4. Evaluate the reflection coefficient using Eq. (3.43).

Moreover, we can calculate the static spin susceptibility using the CTQMC method as follows:

$$\chi_0 = \beta \langle \bar{\sigma}_z^2 \rangle, \tag{3.55}$$

$$\bar{\sigma}_z = \frac{1}{\hbar\beta} \int_0^{\hbar\beta} d\tau\, \sigma_z(\tau) = \frac{2}{\hbar\beta} \sum_{j=0}^{2n-1} (-1)^j \tau_j + 1. \tag{3.56}$$

3.3.3 Binder analysis

Finally, we explain how to determine the critical point of the quantum phase transition for the sub-Ohmic spin-boson model [19]. To study this quantum phase transition, we use the finite size (or temperature) scaling for observable $\mathcal{A}$ in the vicinity of the critical point,

$$\langle \mathcal{A} \rangle (\beta, \alpha) = \beta^{x_{\mathcal{A}}} f_{\mathcal{A}}(\beta^{y_t^*} \delta), \tag{3.57}$$

where $\delta = (\alpha - \alpha_c)/\alpha_c$ denotes the dimensionless distance from the critical point, $x_{\mathcal{A}}$ and $f_{\mathcal{A}}$ are the scaling exponent and scaling function of the observable $\mathcal{A}$, respectively. For the sub-Ohmic spin-boson model, the exponent y_t^* is related to the correlation length exponent ν ($\xi \sim \delta^{-\nu}$ at the critical point $\delta \simeq 0$) as [19, 120, 119]

$$y_t^* = \begin{cases} \dfrac{1}{\nu}, & (0 < s \le 0.5), \\ \dfrac{1}{\nu} + \dfrac{1}{2} - s, & (s > 0.5). \end{cases} \tag{3.58}$$

Now, we introduce the Binder parameter defined as

$$B = \frac{1}{2} \left(3 - \frac{\langle \bar{\sigma}_z^4 \rangle}{\langle \bar{\sigma}_z^2 \rangle^2} \right), \tag{3.59}$$

where $\bar{\sigma}_z = (\hbar\beta)^{-1} \int d\tau\, \sigma_z(\tau)$ is the magnetization for a spin configuration. The Binder parameter takes values of 1 in the localized phase and 0 in the delocalized phase and jumps between them when the coupling strength passes across the critical point. The scaling exponent of the Binder parameter is $x_B = 0$ because it only includes the ratio of the same order of parameters. Therefore, the critical point $\delta = 0$, i.e., $\alpha = \alpha_c$, is determined as a point at which the Binder parameter is independent of the temperature at sufficiently low temperatures.
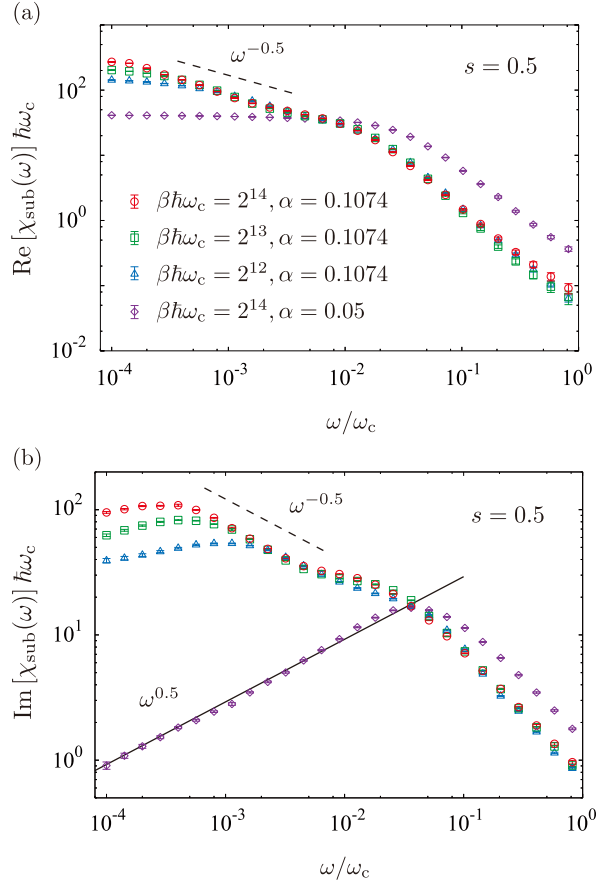
FIGURE 3.8: Frequency dependence of the dynamic spin susceptibility for $s = 0.5$ and $\Delta/\omega_c = 0.1$. (a) and (b) describe the plot of numerical results for the real and imaginary parts of the dynamic spin susceptibility, respectively, calculated by the CTQMC simulations. The three types of plots indicate the results at $\alpha = \alpha_c = 0.1074$ for different temperatures, $\beta\hbar\omega_c = 2^{12}$ (blue), 2^{13} (green), and 2^{14} (red), and the other plot at $\alpha = 0.05$ ($< \alpha_c$) and $\beta\hbar\omega_c = 2^{14}$ (purple). The black solid line in panel (b) is given by the generalized Shiba-Korringa relation (3.63).

3.4   Numerical results

In this section, we present the numerical results for the dynamic spin susceptibility and the microwave reflection at the critical point, $\alpha = \alpha_c$, and below it, $\alpha < \alpha_c$, by performing the CTQMC simulations, as explained in Section 3.3.

3.4.1   Dynamic spin susceptibility

Quantum critical regime

First, we discuss the dynamic spin susceptibility in the quantum critical regime, $\alpha = \alpha_c$. In this regime, the dynamic spin susceptibility exhibits the power-law frequency dependence reflecting the nature of the quantum phase transition,

$$\chi_{\text{sub}}(\omega) \sim \omega^{-y}. \tag{3.60}$$

(a)

(b)
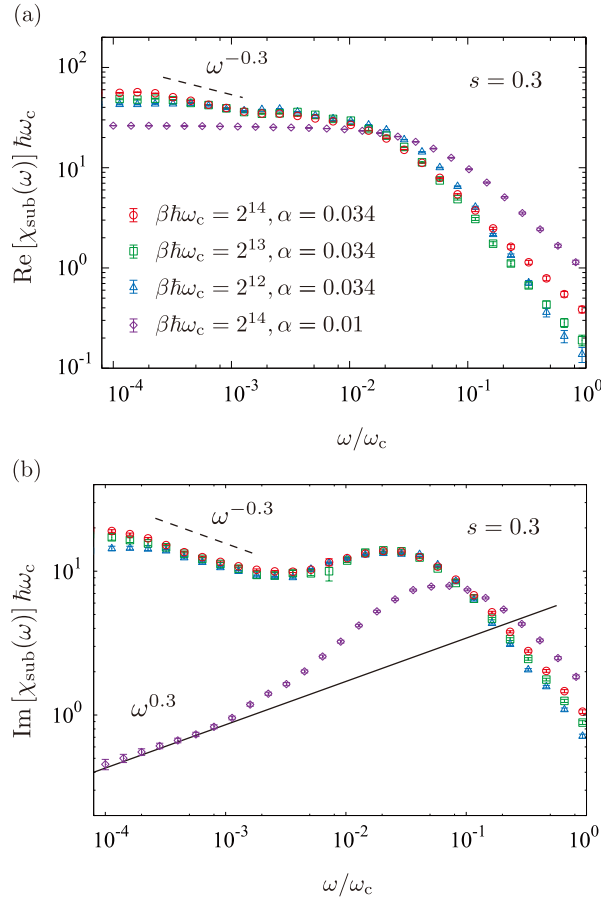
FIGURE 3.9: (a) The real and (b) imaginary parts of the dynamic spin susceptibility for $s = 0.3$ as a function of frequency, which are obtained by the CTQMC calculation. For $s = 0.3$, the critical coupling strength is $\alpha_c = 0.034$. Other parameters and plot colors are the same as those in Fig. 3.8.

Here, y is a critical exponent of the dynamic spin susceptibility and related to that of the imaginary-time spin-spin correlation function as $y = 2 - \eta$. Thus, for $0 < s \leq 0.5$, the critical exponent y can be obtained by using the mean-field result (3.8),

$$y = s. \tag{3.61}$$

Note that, as discussed in Section 2.5, the critical exponent is a complex function of s for $0.5 < s < 1$ because that case belongs to the non-trivial universality class.

To compare the analytical form (3.61) and numerical results, we first consider the case of $s = 0.5$ and $\Delta/\omega_c = 0.1$, for which the critical points are determined as $\alpha_c = 0.1074$ by the Binder analysis, as discussed in Section 3.3. Figures 3.8 (a) and (b) show the frequency dependence of the real and imaginary parts of the dynamic spin susceptibility obtained by the CTQMC simulations at $\alpha = \alpha_c$ for three different temperatures, $\beta\hbar\omega_c = 2^{12}$, 2^{13}, and 2^{14}. As shown in Fig. 3.8, the dynamic spin susceptibility is proportional to $\omega^{-0.5}$ for a frequency range, $k_BT/\hbar \ll \omega \ll \tilde{\Delta}$, where $\tilde{\Delta} \lesssim \Delta$ is the renormalized tunneling frequency dependent of s, Δ/ω_c, and α. This exponent for the low-frequency region is consistent with the critical exponent in Eq. (3.61) for $s = 0.5$. As shown in Fig. 3.9, we can observe the critical power-law behavior (3.61) even for $s = 0.3$, for which the critical point is determined as

$\alpha_c = 0.034$, although the frequency range showing the critical behavior is narrower than the case of $s = 0.5$. Note that our results are in agreement with those of previous studies [115, 128].

Delocalized regime

We next consider the delocalized regime, $\alpha < \alpha_c$, in which the ground state is described by a coherent superposition of the two charge states. At low temperatures, we can apply the generalized Shiba-Korringa relation [129, 38]

$$\lim_{\omega \to 0} \frac{\hbar \text{Im}[\chi_{\text{sub}}(\omega)]}{\omega^s} = 2\pi \alpha \omega_c^{1-s} \left(\frac{\hbar \chi_0}{2} \right)^2. \tag{3.62}$$

This relation provides the low-frequency asymptotic behavior of the dynamic spin susceptibility,

$$\text{Im}[\chi_{\text{sub}}(\omega)] \sim \frac{\hbar \pi \alpha \chi_0^2 \omega_c^{1-s}}{2} \, \omega^s. \tag{3.63}$$

This relation is extended from the Shiba-Korringa relation in the Kondo model [130], which can be described by the local Fermi liquid theory [67]. Thus, what this relation holds means the appearance of the many-body effect.

Fig. 3.8 shows the real and imaginary parts of the dynamic spin susceptibility for $s = 0.5$, $\Delta/\omega_c = 0.1$, and $\beta \hbar \omega_c = 2^{14}$ at $\alpha = 0.05$, which is sufficiently smaller than the critical point $\alpha_c = 0.1074$. The imaginary part of the dynamic spin susceptibility has a peak at a slightly higher frequency than $\tilde{\Delta}$ for the quantum critical regime while the real one has a shoulder. This indicates that the renormalization effect in $\tilde{\Delta}$ due to the sub-Ohmic bath is stronger as the coupling strength increases. At sufficiently small frequencies, $\omega \ll \tilde{\Delta}$, the numerical results for the imaginary part of the dynamic spin susceptibility exhibits the power-law frequency dependence, and its exponent is consistent with the generalized Shiba-Korringa relation (3.63), resulting in $\text{Im}[\chi_{\text{sub}}(\omega)] \propto \omega^{0.5}$ for $s = 0.5$. Note that the static spin susceptibility in the prefactor of Eq. (3.63) is determined numerically by using the CTQMC, as discussed in Section 3.3. One can observe this power-law behavior in the delocalized phase even for $s = 0.3$ in Fig. 3.9.

3.4.2 Reflection

Finally, we discuss the microwave reflection loss, $1 - |r(\omega)|^2$. From Eq. (3.43), the reflection loss can be written as

$$1 - |r(\omega)|^2 = \pi \hbar I_R(\omega) \text{Im} \left[\chi_{\text{sub}}(\omega) \right] + \mathcal{O}(\alpha_R^2). \tag{3.64}$$

Recalling that the bath R (the transmission line) is Ohmic, $I_R(\omega) \propto \omega$, and the coupling between the two-level system and the Ohmic bath is sufficiently weak, $\alpha_R \ll 1$, the reflection loss is almost proportional to $\omega \text{Im}[\chi_{\text{sub}}(\omega)]$. Furthermore, by using Eqs. (3.61), (3.60), and (3.63), we obtain the the power-law behavior of the reflection loss as follows:

$$1 - |r(\omega)|^2 \sim \begin{cases} \omega^{1-s}, & \text{for} \quad \alpha = \alpha_c, \, k_B T/\hbar \ll \omega \ll \tilde{\Delta}, \\ \omega^{1+s}, & \text{for} \quad \alpha < \alpha_c, \, \omega \ll \tilde{\Delta}. \end{cases} \tag{3.65}$$

(a)

(b)
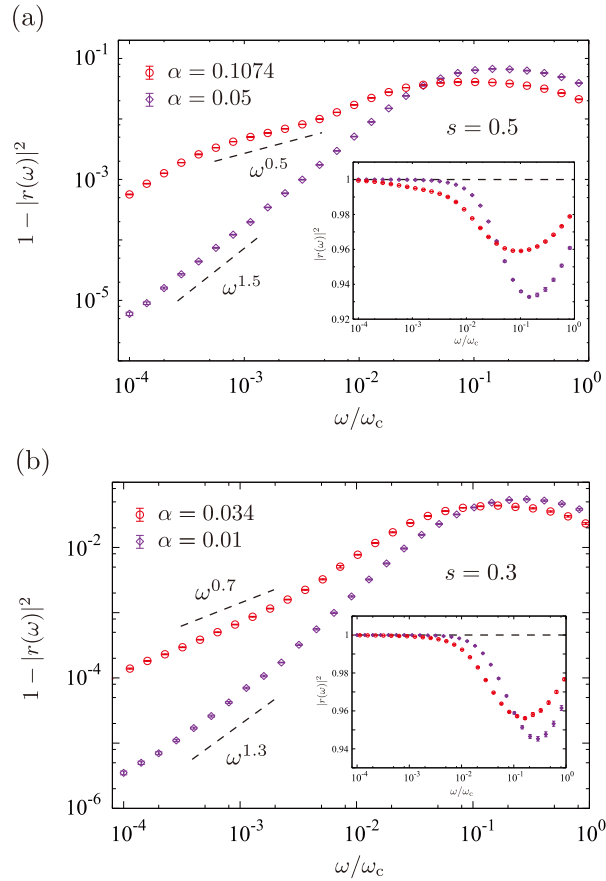
FIGURE 3.10: Frequency dependence of the reflection loss, $1 - |r(\omega)|$, calculated using the CTQMC simulations. The plots represent the numerical results for (a) $s = 0.5$ and (b) $s = 0.3$. The insets in each panel represent the reflection as a function of frequency. The other parameters are set as $\Delta/\omega_c = 0.1$ and $\beta\hbar\omega_c = 2^{14}$. The red and purple plots indicate the results at the critical point ($\alpha = 0.1074$ for $s = 0.5$ and $\alpha = 0.034$ for $s = 0.3$) and below it ($\alpha = 0.05$ for $s = 0.5$ and $\alpha = 0.01$ for $s = 0.3$), respectively.

Figure 3.10 (a) and (b) show the frequency dependence of the reflection loss for $s = 0.5$ and 0.3, respectively. The other parameters are set as $\Delta/\omega_c = 0.1$, $\beta\hbar\omega_c = 2^{14}$, and $\alpha_R = 0.01$. The insets in Fig. 3.10 represent the reflection as a function of frequency. It has a small peak for both the quantum critical regime, $\alpha = \alpha_c$, and the delocalized regime, $\alpha < \alpha_c$, near the renormalized tunneling amplitude $\tilde{\Delta}$. This indicates that the incident microwave is almost reflected but some part of the microwave with characteristic frequency $\tilde{\Delta}$ of the sub-Ohmic spin-boson model is absorbed in the two-level system. For the low frequency, $\omega \ll \tilde{\Delta}$, the reflection loss shows the power-law frequency dependence and approaches zero more slowly for the case of the quantum critical regime than the delocalized phase. Their exponents are consistent with the analytical forms (3.65) both for $s = 0.3$ and 0.5. They are signatures of the quantum phase transition and the quantum many-body effect.

At the end of this section, we add an interesting remark. The characteristic frequency behavior of the reflection loss coming from the quantum phase transition or the quantum many-body effect is dependent on s. Combining this fact and the proposition of the realization of the sub-Ohmic bath with arbitrary s using superconducting circuits in Section 3.2 leads to a possibility that one can control quantum

critical phenomena and quantum many-body phenomena in well-controllable systems.

3.5   Short summary of this chapter

We studied quantum critical phenomena of the sub-Ohmic spin-boson model through the microwave scattering based on the superconducting circuit. By considering a superconducting circuit composed of a charge qubit and an *RLC* transmission line with space-dependent elements, we show that it is effectively described by the sub-Ohmic spin-boson model. Moreover, we clarified the dynamic spin susceptibility and the microwave reflection loss at and far from the quantum phase transition by performing the continuous-time Monte Carlo method. As a result, the Fermi liquid-like feature (the Shiba-Korringa relation) and quantum critical behavior appear in their frequency dependence, depending on the exponent of the spectral density s. This indicates a possibility that quantum criticality can be studied in microwave spectroscopy for superconducting circuits in a realistic setup. In this chapter, we considered only the case of $s \leq 0.5$, which allows us to compare it with the analytical results by the mean-field universality class. It would be an important future problem to check the critical exponents from the numerical approach for a wider range of s.

Chapter 4

Transmission through a Disordered Josephson-junction Chain

In this chapter, we investigate the scattering of elastic waves through a disordered Josephson-junction chain. First, we briefly introduce the model of the disordered Josephson-junction chain in Section 4.1. Next, we move to new results obtained in Ref. [40]. We formulate the elastic scattering off the disordered Josephson-junction chain in the classical limit in Section 4.2. Using both numerical and analytical approaches, we show the results for the transmission in the weakly localized regime in Section 4.3. Finally, we present several pieces of information about the strongly localized regime and compare them with the localization model with the Gaussian white-noise disorder in Section 4.4.

4.1 Disordered Josephson-junction chain

As described in Sections 2.6 and 2.7, the disordered Josephson-junction chain of the length d can be described by the random phase sine-Gordon model (2.48) (for the corresponding circuit, see Fig. 4.1). We repeat the theoretical description of the disordered Josephson-junction chain. The Lagrangian is given as

$$\mathcal{L} = \int_0^d dx \left\{ \frac{\hbar}{2\pi K v} \left[\dot{\theta}(x,t) \right]^2 - \frac{\hbar v}{2\pi K} \left[\partial_x \theta(x,t) \right]^2 + \frac{\Lambda}{a} \cos\left[2\theta(x,t) + \chi(x) \right] \right\}, \quad (4.1)$$

where $\theta(x,t)$ is the local field associated with the accumulated charge and $v = a\sqrt{2E_J E_g}/\hbar$ is the plasmon velocity with the elementary unit length a and $E_g = (2e)^2/(2C_g)$. The Luttinger parameter $K = \pi\sqrt{E_J/(2E_g)}$ is related to the chain impedance as $Z = R_Q/(2K)$. The random phase field satisfies the following statistics; the average,

$$\langle \cos \chi(x) \rangle = \langle \sin \chi(x) \rangle = 0, \quad (4.2)$$

and variance,

$$\sigma^2 = \int_0^d dx \ \langle \cos \chi(x) \cos \chi(0) \rangle = \int_0^d dx \ \langle \sin \chi(x) \sin \chi(0) \rangle. \quad (4.3)$$

At the transmon limit ($E_J \gg E_C$), the quantum phase slips are rare events, and its amplitude is written as

$$\Lambda = \frac{8}{\sqrt{\pi}} \left(2E_J^3 E_C \right)^{1/4} e^{-\sqrt{32E_J/E_C}} \quad (4.4)$$
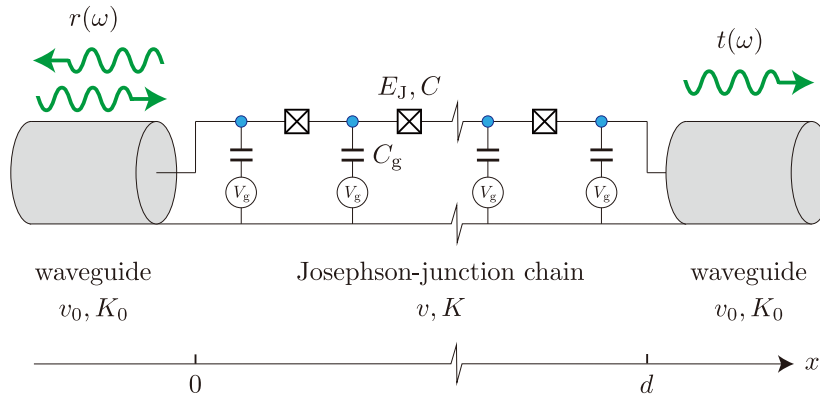
FIGURE 4.1: A disordered Josephson-junction chain of length d. The Josephson energy and the Josephson capacitance of each junction are E_J and C, respectively. The ground capacitance of each superconducting island (blue circle) is C_g. The random background charges are induced by the gate voltages V_g. An incident plasmon wave from one of the waveguides contacted to the Josephson-junction chain is either reflected to the same waveguide or transmitted to the opposite waveguide with the amplitudes $r(\omega)$ and $t(\omega)$, respectively, at frequency ω. The plasmon velocities in the waveguides and the Josephson-junction chain are v_0 and v. The impedances of the waveguides and the Josephson-junction chain are $R_Q/2K_0$ and $R_Q/2K$, respectively.

with $E_C = (2e)^2/(2C)$.

In this thesis, we focus on the classical limit ($K \to 0$). In this limit, as described in Section 2.7, the kinetic term in the Lagrangian (4.1) can be neglected. Then, our problem is reduced to the interplay between the elasticity and the disorder. On the length scale shorter than the Larkin length $R_\star$ defined in Eq. (2.52), the elastic properties still remain, which corresponds to excitations with higher frequencies ($\omega \gtrsim \omega_\star$). However, at low frequencies ($\omega \ll \omega_\star$), the collective pinning effect induced by the disorder breaks the sound-like plasmon spectrum.

4.2   Formalism for scattering problem in the classical limit

In this section, we formulate the scattering problem for the disordered Josephson-junction chain in the classical limit ($K \ll 1$), i.e., in the deep Bose-glass phase. To this end, we consider a setup where the Josephson-junction chain is coupled to two waveguides (see Fig. 4.1). Classically, an incident plasmon wave from one of the waveguides (the left one in Fig. 4.1) is either reflected to the same waveguide or transmitted to the opposite waveguide, with the respective amplitudes $r(\omega)$ and $t(\omega)$. The two waveguides are the same and have the plasmon velocity v_0 and the Luttinger parameter K_0.

Using the continuity of $\theta(x)$ and $(v/K)\partial_x\theta(x)$ at interfaces between the waveguides and the Josephson-junction chain, we find that the plasmon wave reflection and transmission at the interfaces due to the impedance mismatch ($Z \propto 1/K$) is given by

$$R_0 = \left(\frac{K - K_0}{K + K_0}\right)^2, \quad T_0 = \frac{4KK_0}{(K + K_0)^2}. \tag{4.5}$$

4.2.1 Equation of motion

In the classical limit, the field $\theta(x,t)$ can be divided into a static part $\bar{\theta}(x)$ and a small oscillation around it with frequency ω,

$$\theta(x,t) = \bar{\theta}(x) + \psi(x)e^{-i\omega t}. \tag{4.6}$$

The static field $\bar{\theta}(x)$ minimizes the classical energy functional

$$\mathcal{E}[\theta] = \int_0^d dx \left[\frac{\hbar v}{2\pi K} (\partial_x \theta)^2 - \Lambda \cos(2\theta + \chi) \right], \tag{4.7}$$

with boundary conditions $\partial_x \bar{\theta}(0) = \partial_x \bar{\theta}(d) = 0$ coming from the continuity of voltages at the both edges of the Josephson-junction chain at $x = 0$ and d:

$$\frac{v}{K}\partial_x\theta(0^+,t) = \frac{v_0}{K_0}\partial_x\theta(0^-,t), \quad \frac{v}{K}\partial_x\theta(d^-,t) = \frac{v_0}{K_0}\partial_x\theta(d^+,t), \tag{4.8}$$

respectively. The small oscillation $\psi(x)$ takes the asymptotic form of a scattering state at frequency ω in the waveguides,

$$\psi(x) = \begin{cases} e^{i\omega x/v_0} + r(\omega)e^{-i\omega x/v_0}, & (x < 0), \\ t(\omega)e^{i\omega(x-d)/v_0}, & (x > d), \end{cases} \tag{4.9}$$

where $r(\omega)$ and $t(\omega)$ are the elastic reflection and transmission amplitudes, respectively. By linearizing the equation of motion, the small oscillation $\psi(x)$ solves the Schrödinger-like wave equation

$$\omega^2 \psi(x) = -v^2 \partial_x^2 \psi(x) + \mathcal{V}(x)\psi(x), \tag{4.10}$$

with boundary conditions

$$\psi(0) = 1 + r(\omega), \tag{4.11}$$

$$\psi(d) = t(\omega), \tag{4.12}$$

$$v\partial_x\psi(0) = i\omega \frac{K}{K_0}[1 - r(\omega)], \tag{4.13}$$

$$v\partial_x\psi(d) = i\omega \frac{K}{K_0}t(\omega), \tag{4.14}$$

which come from the continuity of current

$$\partial_t\theta(0^+,t) = \partial_t\theta(0^-,t), \quad \partial_t\theta(d^-,t) = \partial_t\theta(d^+,t), \tag{4.15}$$

and voltage (4.8). Here, the effective disorder potential $\mathcal{V}(x)$ takes

$$\mathcal{V}(x) = \begin{cases} \dfrac{4\pi K v \Lambda}{\hbar} \cos\left[2\bar{\theta}(x) + \chi(x)\right], & (0 < x < d), \\ 0, & (\text{otherwise}), \end{cases} \tag{4.16}$$

and its properties will be discussed later. Note that, in the waveguides, since the effective disorder potential is vanishing, the linearized equation of motion (4.10) becomes the usual wave equation, which is consistent with the asymptotic form of the small oscillations (4.9).

4.2.2 Numerical method

Here, we describe our strategy to calculate the scattering amplitudes numerically. First, we rewrite our problem with the dimensionless variables by rescaling the spatial dimension by the Larkin length $R_\star$ and the frequency dimension by the Larkin frequency $\omega_\star$. Next, the dimensionless spatial variables are discretized with a small spacing ϵ as $d/R_\star = (M+1)\epsilon$, where M is the division number. Then, the above prescription leads the classical energy functional (4.7), in units of $(\epsilon\hbar v)/(2\pi K R_\star)$, to take the discretized form:

$$\tilde{\mathcal{E}}[\theta] = \sum_{m=0}^{M-1} \left[\left(\frac{\theta_{m+1} - \theta_m}{\epsilon} \right)^2 - \frac{\mathcal{V}_m}{2} \right] - \frac{\mathcal{V}_0 + \mathcal{V}_M}{4}. \tag{4.17}$$

Here,

$$\mathcal{V}_m = 2\left[\mathcal{V}'_m \cos 2\theta_m + \mathcal{V}''_m \sin 2\theta_m \right] \tag{4.18}$$

is the discretized effective disorder potential in dimensionless units, and the correlators (2.50) are reproduced in continuum limit ($\epsilon \to 0$) if $\langle \mathcal{V}'_m \rangle = \langle \mathcal{V}''_m \rangle = \langle \mathcal{V}'_m \mathcal{V}''_n \rangle = 0$ and $\langle \mathcal{V}'_m \mathcal{V}'_n \rangle = \langle \mathcal{V}''_m \mathcal{V}''_n \rangle = \epsilon^{-1} \delta_{m,n}$. The last term in Eq. (4.17) is derived from considering an infinite periodic chain with the mirror symmetry $\mathcal{V}_m = \mathcal{V}_{2M-m}$ in unit chain ($0 \leq m \leq 2M - 1$). This ensures that the boundary conditions $\partial_x \bar{\theta}(0) = \partial_x \bar{\theta}(d) = 0$ are satisfied in continuum limit.

We compare two ways to generate the random fields $\mathcal{V}'_m$ and $\mathcal{V}''_m$. In the phase model reminiscent of the original model, we relate them with flatly distributed random phases $\chi_m \in [0, 2\pi)$ at each site,

$$\mathcal{V}'_m = \sqrt{\frac{2}{\epsilon}} \cos \chi_m, \quad \mathcal{V}''_m = \sqrt{\frac{2}{\epsilon}} \sin \chi_m. \tag{4.19}$$

Alternatively, in the box model, the random fields $\mathcal{V}'_m$ and $\mathcal{V}''_m$ are independent and flatly distributed in the interval $(-\sqrt{3/\epsilon}, \sqrt{3/\epsilon})$. Our numerical results could not distinguish between the two models (see Figs. 4.2).

The static fields $\{\bar{\theta}_m\}$ are determined by minimizing the classical energy functional (4.17). To perform the minimization, we adopted the minimization method described in Ref. [102]. Note that a common π-shift of the static field, $\theta_m \to \theta_m + \pi$, leaves the classical energy functional (4.17) invariant and the effective potential (4.18) only depends on $\bar{\theta}_m \mod \pi$. Thus, we can restrict for solutions $\bar{\theta}_m \in (-\pi/2, \pi/2]$ by substituting $(\theta_m - \theta_{m+1})^2$ with $\min_k (\theta_m - \theta_{m+1} - k\pi)^2$ in Eq. (4.17).

Now, we calculate the scattering amplitudes using the static fields $\bar{\theta}$ obtained by the above method. The linearized equation of motion (4.10) and boundary conditions (4.11)-(4.14) are discretized as

$$\left(\frac{\omega}{\omega_\star} \right)^2 \psi_m + \frac{\psi_{m+1} + \psi_{m-1} - 2\psi_m}{\epsilon^2} - \mathcal{V}_m \psi_m = 0, \tag{4.20}$$

for $0 < m \leq M$, and

$$\psi_0 = 1 + r(\omega), \tag{4.21}$$

$$\psi_M = t(\omega), \tag{4.22}$$

$$\frac{\psi_1 - \psi_0}{\epsilon} = i\frac{\omega}{\omega_\star}\frac{K}{K_0}[1 - r(\omega)], \tag{4.23}$$

$$\frac{\psi_M - \psi_{M-1}}{\epsilon} = i\frac{\omega}{\omega_\star}\frac{K}{K_0}t(\omega), \tag{4.24}$$

respectively. Using these boundary conditions, we can eliminate ψ_0 and ψ_M and express $r(\omega)$ and $t(\omega)$ in terms of ψ_1 and ψ_{M-1} as

$$r(\omega) = \left(1 - i\epsilon\frac{K}{K_0}\frac{\omega}{\omega_\star}\right)^{-1}\left(\psi_1 - 1 - i\epsilon\frac{K}{K_0}\frac{\omega}{\omega_\star}\right), \tag{4.25}$$

$$t(\omega) = \left(1 - i\epsilon\frac{K}{K_0}\frac{\omega}{\omega_\star}\right)^{-1}\psi_{M-1}. \tag{4.26}$$

Moreover, the equation of motion (4.20) reads eigenvalue equation with the vector $\{\psi_1, \ldots, \psi_{M-1}\}$. Thus, for a given disorder configuration yielding the potentials $\mathcal{V}_m$, by solving the eigenvalue problem, we obtain the scattering amplitudes from Eqs. (4.25) and (4.26). The averaged scattering amplitudes are evaluated numerically by iterating this procedure for a large number of disorder configurations, typically 10^4 disorder configurations in this thesis.

4.2.3 Effective disorder potential

The effective potential (4.16) depends on the solution $\bar{\theta}(x)$ of a nontrivial optimization problem defined by the functional (4.7), as discussed in the previous subsection. Thus, it is expected to have a complex pattern of non-Gaussian correlations of which, to the best of our knowledge, little is known. From the reality condition $\omega^2 > 0$ for the eigen spectrum of Eq. (4.10), the local potential mean has a well defined positive sign, $\langle \mathcal{V}(x) \rangle > 0$. Figure 4.2 (a) shows the mean of the disorder potential as a function of space for $d/R_\star = 20$. The mean reaches a constant value sufficiently far from the edges, on the scale of $R_\star$. We also found numerically a fitting function $v(x)$ that describes the exponential enhancement of $\langle \mathcal{V}(x) \rangle$ near the edges, see the legend of Fig. 4.2 (a).

The potential $\mathcal{V}(x)$ inherits a finite correlation length $R_\star$ from $\bar{\theta}$, despite the underlying disorder $\chi(x)$ being a short-ranged one. We characterize the spatial correlations in $\mathcal{V}(x)$ by considering its second cumulant and expressing it in the form

$$\langle\langle \mathcal{V}(x)\mathcal{V}(y) \rangle\rangle \equiv \langle (\mathcal{V}(x) - \langle \mathcal{V} \rangle)(\mathcal{V}(y) - \langle \mathcal{V} \rangle) \rangle$$
$$= \omega_\star^4\left[4\delta\left(\frac{x-y}{R_\star}\right) - w\left(\frac{x-y}{R_\star}\right)\right]. \tag{4.27}$$

Here, the introduced function $w(x)$ is smooth and decays at large scales. We find $w(x)$ numerically as $w(x) = ce^{-|x|/a}$ with $c \approx 3.24$ and $a \approx 0.346$ (see Fig. 4.2 (b)). We note that the random potential $\mathcal{V}(x)$ is non-Gaussian. Its third-order cumulant is shown in the inset of Fig. 4.2 (b). The Fourier component of $\langle\langle \mathcal{V}(x)\mathcal{V}(0) \rangle\rangle$ at small

(a)

(b)
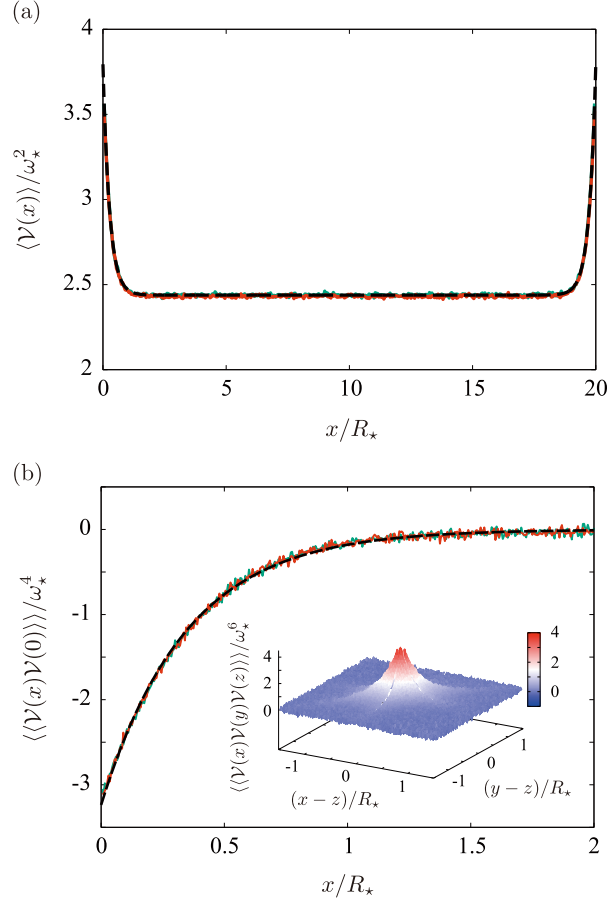
FIGURE 4.2: (a) The mean effective disorder potential and (b) the smooth part of the second-order correlation function at $d/R_\star = 20$. The green and red lines are the numerically obtained curves for the random phase and box models, respectively; they cannot be distinguished from each other. The dashed line represents the fitting functions $v(x) = d[e^{-x/b} + e^{-(d-x)/b}] + v_0$ with $d \approx 1.36$, $b \approx 0.269$, and $v_0 \approx 2.44$ in panel (a) and $-w(x) = -ce^{-|x|/a}$ with $c \approx 3.24$ and $a \approx 0.346$ in panel (b). The inset of panel (b) shows the third-order cumulant at noncoinciding points.

momentum on the scale of $1/R_\star$ is reduced by a factor $1 - \eta$ with

$$\eta = \frac{1}{4} \int_0^{d/R_\star} dx \, w(x) \approx 0.561, \tag{4.28}$$

compared to its large-momentum value, which is determined by the delta-function in Eq. (4.27). The property of $\eta \neq 0$ is the consequence of the collective pinning mechanism. In the large-frequency range of interest in Section 4.3, η is the only parameter needed to quantitatively predict the statistics of the scattering amplitudes. On the other hand, we illustrate in Section 4.4 that the signature properties of the reflection and transmission amplitudes at low frequencies cannot be accounted for by a white Gaussian disorder. Therefore, we attribute these properties to the non-Gaussianity of the potential $\mathcal{V}(x)$ induced by the pinning effect.

4.3 Weakly localized regime

In this section, we derive an analytical formula for the transmission $\langle T(\omega) \rangle \equiv \langle |t(\omega)|^2 \rangle$ in the high-frequency regime ($\omega > \omega_\star$), where disorder can be treated perturbatively.

4.3.1 Mapping to the Dirac equation

First, we show that, at high frequency ($\omega > \omega_\star$), the equation of motion (4.10) is equivalent to a Dirac equation in Gaussian random fields. Let us introduce two functions, $R(x)$ and $L(x)$, such that

$$\psi(x) = R(x) + L(x), \tag{4.29}$$

$$\partial_x \psi(x) = i\frac{\omega}{v} \left[R(x) - L(x) \right]. \tag{4.30}$$

Using $\partial_x \psi(x) = \partial_x R(x) + \partial_x L(x)$ and the equation of motion (4.10), the new functions are followed by

$$\omega R(x) = -iv\partial_x R(x) + \frac{\mathcal{V}(x)}{2\omega} \left[R(x) + L(x) \right], \tag{4.31}$$

$$\omega L(x) = +iv\partial_x L(x) + \frac{\mathcal{V}(x)}{2\omega} \left[R(x) + L(x) \right]. \tag{4.32}$$

The functions $R(x)$ and $L(x)$ have the meaning of the right- and left-moving components of the wave function, respectively. The terms $\propto \mathcal{V}(x)$ in Eqs. (4.31) and (4.32) result in scattering between the components $R(x)$ and $L(x)$. In the weak-disorder regime, only the forward- and back-scattering amplitudes evaluated within the Born approximation determine the scattering properties of the Josephson-junction chain. At $\omega \gg \omega_\star$, since the forward- and backward-scattering amplitudes are associated with the harmonics of the effective disorder potential near momenta $k = 0$ and $k = 2\omega/v \gg 1/R_\star$, respectively, it allows us to expand the effective disorder potential as

$$\frac{\mathcal{V}(x)}{2\omega} \approx \Delta_0(x) + \Delta(x)e^{2i\omega x/v} + \Delta^*(x)e^{-2i\omega x/v}, \tag{4.33}$$

where the real function $\Delta_0(x)$ and the complex function $\Delta(x)$ are slowly varying random functions in the scale of v/ω. We find that the slow components of Eqs. (4.31) and (4.32) yield a Dirac equation,

$$\left[-iv\partial_x \tau_3 + \Delta_0(x) + \Delta_1(x)\tau_1 + \Delta_2(x)\tau_2 \right] \Phi(x) = 0, \tag{4.34}$$

where $\Phi(x) = (R(x)e^{-i\omega(x-d)/v}, L(x)e^{i\omega(x-d)/v})^t$, $\Delta(x) = \Delta_1(x) + i\Delta_2(x)$, and Pauli matrices $\tau_{1,2,3}$. Using Eq. (4.27), the Born approximation applied to scattering off a potential given by Eq. (4.33) provides the forward- and back-scattering lengths,

$$\ell_0(\omega) = \frac{\ell_\pi(\omega)}{1 - \eta}, \quad \ell_\pi(\omega) = R_\star \left(\frac{\omega}{\omega_\star} \right)^2, \tag{4.35}$$

respectively. Thus, the correlation between the random offset charge (short-range correlation) and the static charge density $\propto \partial_x \bar{\theta}$ (long-range correlation) induced by the scattering off the potential tends to weaken the forward-scattering rate and introduces a quantitative difference between $\ell_0(\omega)$ and $\ell_\pi(\omega)$ by a factor $1/(1 - \eta)$.

As $\ell_0(\omega)$, $\ell_\pi(\omega) \gg R_\star$ in the high-frequency regime, the random fields $\Delta_0(x)$ and $\Delta(x)$ in Eq. (4.34) are viewed as Gaussian ones each of which has a length scale $\sim R_\star$. The Fourier components of the correlation function of $\mathcal{V}(x)$ are reproduced by the Fourier components of correlation functions of the random fields:

$$\langle \Delta_0(x)\Delta_0(y)\rangle = (1-\eta)\frac{\omega_\star^4}{\omega^2}\delta\left(\frac{x-y}{R_\star}\right), \tag{4.36}$$

$$\langle \Delta(x)\Delta^*(y)\rangle = \frac{\omega_\star^4}{\omega^2}\delta\left(\frac{x-y}{R_\star}\right). \tag{4.37}$$

Both fields $\Delta_0(x)$ and $\Delta(x)$ induce a random phase between right- and left-movers. The contribution from $\Delta_0(x)$ to the phase acquired over a distance x is estimated as $(2/v)\int_0^x dy\,\Delta_0(y)$, and its variance grows as $4x/\ell_0(\omega)$. As we will see below, the additional contribution from $\Delta(x)$ is $2x/\ell_\pi(\omega)$, and it only quantitatively modifies the result about the random phase. Phase scrambling occurs in a longer Josephson-junction chain with $d \gg \ell_0(\omega)$, $\ell_\pi(\omega)$. Using Eq. (4.35), this condition is equivalent to a small frequency condition, $\omega \ll \omega_{\rm cr}$ with crossover frequency $\omega_{\rm cr} = \omega_\star\sqrt{d/R_\star}$. Thus, we can see loss of coherent phases for $\omega_\star \ll \omega \ll \omega_{\rm cr}$. Reference [98] addressed the role of $\omega_{\rm cr}$ in the visibility of oscillations in the reflection amplitude. In this thesis, we find a similar effect in the frequency dependence of the transmission.

In addition, the backward-scattering represented by $\Delta(x)$ is responsible for the plasmons localization. The localization physics will be discussed in Section 4.4.

4.3.2   Fokker-Planck formalism

To proceed further, we use the Fokker-Planck formalism that was developed to predict the statistics of scattering properties of waves subject to Gaussian white-noise disorder. The previously known results [131, 132, 133, 134, 135] assume a perfect impedance matching. In this thesis, we generalize them to the case of a finite impedance mismatch.

The wave functions in the waveguides and the Josephson-junction chain are related through

$$\begin{pmatrix} R(0) \\ r(\omega) \end{pmatrix} = S_0\begin{pmatrix} 1 \\ L(0) \end{pmatrix}, \quad \begin{pmatrix} t(\omega) \\ L(d) \end{pmatrix} = S_0^T\begin{pmatrix} R(d) \\ 0 \end{pmatrix}. \tag{4.38}$$

Here, a phase factor $e^{-i\omega d/v}$ was absorbed in the transmission coefficient $t(\omega)$ and the scattering matrix at each edge is

$$S_0 = \begin{pmatrix} t_0 & r_0 \\ -r_0 & t_0 \end{pmatrix} \tag{4.39}$$

with $r_0 = \sqrt{R_0}$ and $t_0 = \sqrt{T_0}$ (see Eq. (4.5)). This allows us to relate the scattering amplitudes with the Ricatti variable,

$$z(x) = \frac{L(x)}{R(x)}e^{2i\omega(x-d)/v}, \tag{4.40}$$

at the edges of the chain ($x = 0, d$) as follows:

$$r(\omega) = \frac{-r_0 + z(0)e^{2i\omega d/v}}{1 - r_0 z(0)e^{2i\omega d/v}}, \quad r_0 = z(d). \tag{4.41}$$

From the Dirac equation (4.34), the Ricatti variable is a solution of a first-order non-linear stochastic differential equation,

$$-iv\partial_x z(x) = 2\Delta_0(x)z(x) + \Delta^*(x) + \Delta(x)z^2(x). \tag{4.42}$$

Thus, the reflection coefficient $r(\omega)$ and the transmission $T(\omega) = 1 - |r(\omega)|^2$ are expressed in terms of a solution of Eq. (4.42) with a given boundary condition (4.41).

Since the Ricatti equation (4.42) can be seen as a Wiener process, by taking advantage of the Gaussian correlators (4.36) and (4.37), we derive the Fokker-Planck equation for the conditional distribution probability $P(x, \theta_1, \theta_2)$, where θ_1 and θ_2 are the amplitude and the phase of the Ricatti variable such that $z = e^{i\theta_1}e^{-\theta_2}$, (see Appendix D for the derivation)

$$-\frac{\partial P}{\partial x} = \frac{2}{\ell(\omega)}\frac{\partial^2 P}{\partial \theta_1^2} + \frac{1}{\ell_\pi(\omega)}\frac{\partial^2}{\partial \theta_2^2}\left(\sinh^2\theta_2 P\right), \tag{4.43}$$

for $0 < x < d$, with the mean-free path

$$\ell(\omega) = \left(\frac{1}{\ell_0(\omega)} + \frac{1}{2\ell_\pi(\omega)}\right)^{-1} = \frac{2}{3 - 2\eta}\ell_\pi(\omega) \tag{4.44}$$

Moreover, the solution of Eq. (4.43) is separable, $P(x, \theta_1, \theta_2) = P_1(x, \theta_1)P_2(x, \theta_2)$, and each factor satisfies

$$-\frac{\partial P_1}{\partial x} = \frac{2}{\ell(\omega)}\frac{\partial^2 P_1}{\partial \theta_1^2}, \tag{4.45}$$

$$-\frac{\partial P_2}{\partial x} = \frac{1}{\ell_\pi(\omega)}\frac{\partial^2}{\partial \theta_2^2}\left(\sinh^2\theta_2 P_2\right), \tag{4.46}$$

with initial conditions $P_1(d, \theta_1) = \delta(\theta_1)$ and $P_2(d, \theta_2) = \delta(\theta_2 - \theta_0)$ with $\theta_0 = -\ln r_0$. Note that the statistics of θ_2 (4.46) is only sensitive to backward-scattering, i.e., the amplitude of the Ricatti variable is reflected from the localization properties. By contrast, the statistics of θ_1 (4.45), which describes the random phase between right- and left-movers, depends both on forward- and backward-scattering.

Since Eq. (4.45) is a standard diffusion equation, its solution at $x = 0$ is easily obtained by

$$P_1(\theta_1) \equiv P_1(x = 0, \theta_1) = \frac{1}{\sqrt{8\pi d/\ell}}\exp\left(-\frac{\theta_1^2}{8d/\ell}\right). \tag{4.47}$$

Then, the variance of the θ_1, $\langle\theta_1^2\rangle = 4d/\ell_0 + 2d/\ell_\pi$, includes the contributions from Δ_0 and Δ, which has the same order of magnitude, as discussed at the end of the
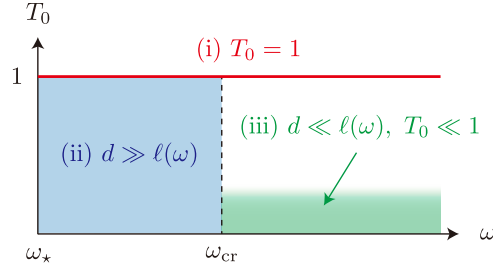
FIGURE 4.3: Parameter space of transmission due to impedance mismatch T_0 and frequency ω. The transmission $\langle T \rangle$ (4.49) can be expressed in simple forms for three parameter regions; (1) $T_0 = 1$, (2) $d \gg \ell(\omega)$, and (3) $d \ll \ell(\omega)$ and $T_0 \ll 1$.

previous subsection. The solution of Eq. (4.46) can also be obtained as

$$
\begin{aligned}
P_2(\theta_2) &\equiv P_2(x = 0, \theta_2) \\
&= \frac{e^{-d/4\ell_\pi}}{4\sinh^2\theta_2} \int_0^\infty dk\, k \tanh\left(\frac{\pi k}{2}\right) P_{-\frac{1}{2}+i\frac{k}{2}}(\coth\theta_2) P_{-\frac{1}{2}+i\frac{k}{2}}(\coth\theta_0) e^{-k^2 d/4\ell_\pi},
\end{aligned}
\tag{4.48}
$$

where $P_\nu(x)$ is the Legendre function of the first kind (see Appendix E for the derivation). Finally, we obtain the ensemble-averaged transmission as

$$
\langle T \rangle = \int d\theta_1 \int d\theta_2\, P_1(\theta_1) P_2(\theta_2) T(\theta_1, \theta_2),
\tag{4.49}
$$

where

$$
T(\theta_1, \theta_2) = T_0 \frac{1 - e^{-2\theta_2}}{1 + r_0^2 e^{-2\theta_2} - 2r_0 \sin(2\omega d/v + \theta_1) e^{-\theta_2}}
\tag{4.50}
$$

is obtained by plugging $z(0) = e^{i\theta_1 - \theta_2}$ into Eq. (4.41) and using $T = 1 - |r|^2$.

In the rest of this subsection, using Eq. (4.50), we derive simple formulas for the transmission in three cases (see Fig.).

(i) perfect impedance matching ($T_0 = 1$)

At $T_0 = 1$, Eq. (4.50) simplifies $T(\theta_1, \theta_2) = 1 - e^{-2\theta_2}$, which indicates that the statistics of θ_2 fully determines the transmission coefficient. By using properties of the Legendre function,

$$
P_\nu(1) = 1, \quad \text{and} \quad \int_1^\infty dx\, \frac{1}{1+x} P_{-\frac{1}{2}+i\frac{k}{2}}(x) = \frac{\pi}{\cosh(k\pi/2)},
\tag{4.51}
$$

(see Eq. 7.131.1 in Ref. [136]), we obtain the simple form for the transmission:

$$
\langle T(\omega) \rangle = \int_0^\infty dk\, \frac{\pi k}{2} \frac{\tanh(\pi k/2)}{\cosh(\pi k/2)} e^{-(1+k^2)d/4\ell_\pi(\omega)}.
\tag{4.52}
$$
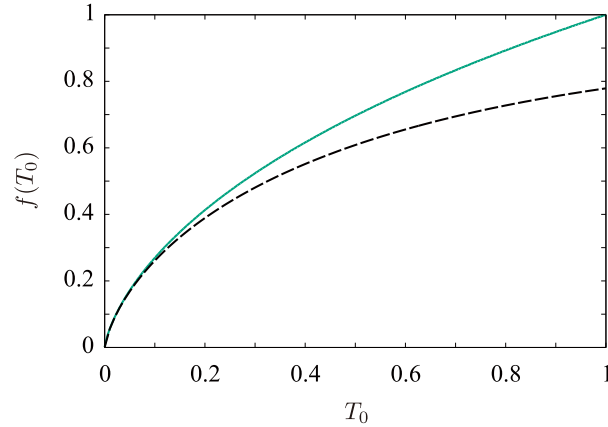
FIGURE 4.4: $f(T_0) = (4T_0/\pi^2)\mathbb{K}^2(1 - T_0)$ (green line) and its asymptotic form (4.57) for $T_0 \ll 1$ (dashed line).

At $d \ll \ell_\pi(\omega)$, $\langle T \rangle \approx 1$ as expected for a ballistic junction. On contrary, at $d \gg \ell_\pi(\omega)$, the ensemble-averaged transmission is

$$\langle T(\omega) \rangle \approx \frac{\pi^{5/2}}{2} \left(\frac{\ell_\pi(\omega)}{d} \right)^{3/2} e^{-d/4\ell_\pi(\omega)}, \tag{4.53}$$

which is agreement with Ref. [132]. Note that the frequency dependence of $\langle T(\omega) \rangle$ is smooth (no oscillations) and fully captured by $\ell_\pi(\omega)$.

(ii) asymptote at $d \gg \ell(\omega)$ and arbitrary T_0

The sine term regarding θ_1 in Eq. (4.50) produces Fabry-Pérot oscillations of the transmission with period $\pi v/d$ when the impedance mismatch is finite $K \neq K_0$. At $d \gg \ell(\omega)$, the dispersion of θ_1 given by Eq. (4.47) washes out the oscillations on average. Thus, in this regime, θ_1 can be taken as uniformly distributed, and Eq. (4.49) simplifies to

$$\langle T \rangle = \int d\theta_2 \, P_2(\theta_2) T(\theta_2), \quad T(\theta_2) = \frac{T_0(1 - e^{-2\theta_2})}{1 - R_0 e^{-2\theta_2}}. \tag{4.54}$$

Note that, at $T_0 = 1$, it reproduces Eq. (4.52). Let us calculate the transmission for an arbitrary value of T_0 using Eqs. (4.54) and (4.48). For $d \gg \ell_\pi(\omega)$, the k-integral in Eq. (4.48) is dominated by the region $k \ll 1$, so that we can replace

$$P_{-\frac{1}{2}+i\frac{k}{2}}(x) \approx P_{-\frac{1}{2}}(x) = \frac{2\sqrt{2}}{\pi\sqrt{x+1}} \mathbb{K}\left(\frac{x-1}{x+1} \right), \tag{4.55}$$

where $\mathbb{K}(m)$ is the complete elliptic integral. After performing the k-integral, we obtain

$$\langle T(\omega) \rangle = \frac{\pi^{5/2}}{2} \left(\frac{\ell_\pi(\omega)}{d} \right)^{3/2} e^{-d/4\ell_\pi(\omega)} f(T_0), \tag{4.56}$$

with $f(T_0) = (4T_0/\pi^2)\mathbb{K}^2(1 - T_0)$ (see Fig. 4.4). In particular, at the perfect impedance matching ($T_0 = 1$), $f(T_0 = 1) = 1$, which reproduces Eq. (4.53), while, at large

impedance mismatches ($T_0 \ll 1$),

$$f(T_0 \ll 1) \approx \frac{T_0}{\pi^2} \ln^2 \left(\frac{16}{T_0} \right). \tag{4.57}$$

Note that, as in Eq. (4.53), the frequency dependence of the pre-exponential factor in Eq. (4.56) comes only via $\ell_\pi(\omega)$, i.e., the transmission is smooth (no oscillations) as a function of frequency in this regime.

(iii) asymptote at $d \ll \ell(\omega)$ and $T_0 \ll 1$

At finite impedance mismatch and $d \ll \ell(\omega)$, Fabry-Pérot oscillations exist. For large mismatch ($T_0 \ll 1$), we can use the initial value for the θ_2-distribution, $P_2(\theta_2) \approx \delta(\theta_2 - T_0/2)$, and then obtain

$$\langle T(\omega) \rangle = \sum_n \int d\theta_1 \frac{T_0^2}{T_0^2 + [2(\omega - \omega_n)d/v + \theta_1]^2} P_1(\theta_1) \tag{4.58}$$

with $P_1(\theta_1)$ of Eq. (4.47). Here, $\omega_n = n\pi v/d$ are the frequencies at which the transmission has local maxima. Equation (4.58) describes how, as the frequency decreases, the oscillations' Lorentzian lineshapes with half-width $T_0 v/2d$, which is determined solely by the impedance mismatch, evolve into Gaussian ones with half-width $v\sqrt{2\ln 2/d\ell(\omega)}$, which is determined by the randomness of the Josephson-junction chain. The crossover frequency is given by ω_{cr}/T_0. Remarkably, in the frequency range $\omega_{\mathrm{cr}} \ll \omega \ll \omega_{\mathrm{cr}}/T_0$ the width of the oscillations is sensitive to η (see Eq. (4.44)), i.e., the collective pinning.

4.3.3   Numerical results

The brute-force numerical calculations for the transmission are compared with the predictions from the Fokker-Planck formalism in Fig. 4.5. In that figure, Eq. (4.52) is used at perfect impedance matching ($K/K_0 = 1$), while we use

$$\langle T(\omega) \rangle = 2\pi T_0 \sum_n P_1 \left(\frac{2(\omega - \omega_n)d}{v} \right) \int d\theta_2 \frac{2\theta_2}{2\theta_2 + T_0} P_2(\theta_2), \tag{4.59}$$

for $\omega_\star \ll \omega \ll \omega_{\mathrm{cr}}/T_0$, at $T_0 \ll 1$ (see Figs. 4.5 (a) and (b), respectively). They are in good agreement with each other for the high-frequency region.

The localization properties of a disordered Josephson-junction chain are frequently characterized by its Lyapunov exponent, $\gamma(\omega) = -(2d)^{-1}\ln T(\omega)$ for a long chain. In contrast with the transmission, the Lyapunov exponent has the self-averaging property [131]. Here, for a random variable $\vec{X} = (X_1, X_2, \ldots, X_N)$, the self-averaging property means

$$\langle X_j \rangle = \lim_{N \to \infty} \frac{1}{N} \sum_{i=1}^{N} X_i, \tag{4.60}$$

for arbitrary j, where $\langle \cdot \rangle$ denotes averaging over all disorder configurations. In Fig. 4.6 (a), we show the frequency dependence of the averaged Lyapunov exponent, $\langle \gamma(\omega) \rangle$ for different chain lengths at the impedance matching ($K/K_0 = 1$). Its inverse defines the localization length, $L_{\mathrm{loc}}(\omega) = 1/\langle \gamma(\omega) \rangle$. We checked numerically that a celebrated Thouless relation [137], $L_{\mathrm{loc}}(\omega) = 2\ell_\pi(\omega)$, works well
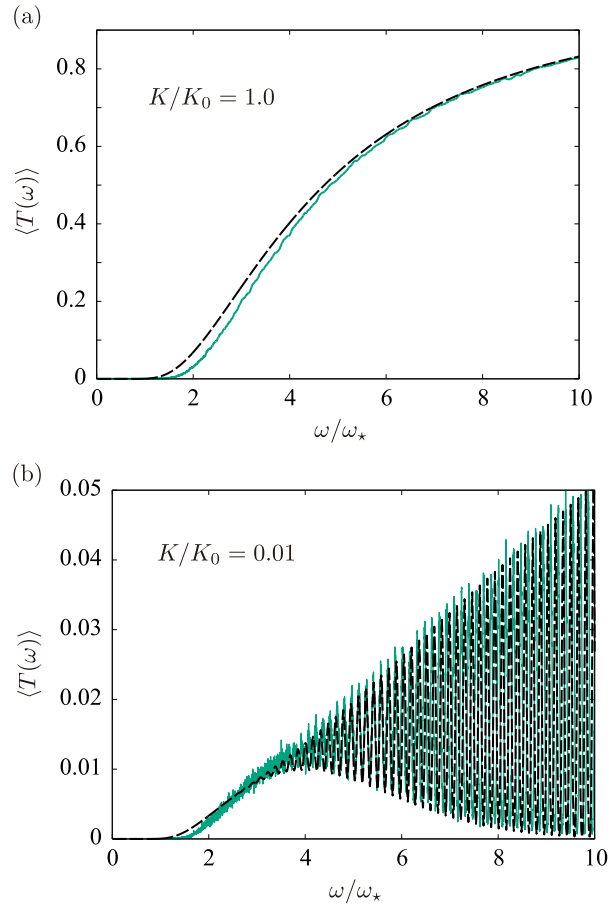
FIGURE 4.5: Frequency dependence of $\langle T(\omega) \rangle$ for (a) $K/K_0 = 1.0$ and (b) $K/K_0 = 0.01$ and $d/R_\star = 20$. The green lines are the numerical results, the dashed line is Eq. (4.52) in panel (a) and Eq. (4.59) in panel (b).

at large frequencies, $\omega \gg \omega_\star$. The self-averaging nature of $\gamma(\omega)$ is associated with the log-normal character of the distribution of the transmission. To discuss its statistics, the frequency dependence of the ratio between mean and variance, $\Sigma(\omega) = d \langle\langle \gamma^2(\omega) \rangle\rangle / \langle \gamma(\omega) \rangle$, is plotted in Fig. 4.6 (b). According to the Fokker-Planck formalism [131], that ratio should be 1 at $\omega_\star \ll \omega \ll \omega_{\mathrm{cr}}$. Despite the tendency as d increases, the agreement is not perfect. (We attribute it to insufficient length.) There was a renewed interest in $\Sigma(\omega)$ [138, 139, 140, 141] to test the single-parameter scaling hypothesis of the theory of localization [26].

The presence of the factor $1/4$ in the argument of the exponent in Eq. (4.53) or (4.56) reflects that the averaged transmission is dominated by rare, optimal disorder configurations – not simply captured by the log-normal distribution (tails), and which produce a resonant transmission, $T \sim 1$ [142, 143, 144]. In other words, $\langle T \rangle \gg T_{\mathrm{typ}}$ where $T_{\mathrm{typ}} = \exp(\langle \ln T \rangle)$ is the typical transmission. To check this effect, in Fig. 4.7, we plot the frequency dependence of their ratio $\ln \langle T(\omega) \rangle / \langle \ln T(\omega) \rangle$ for various lengths at $K = K_0$. (We attribute to insufficient length the deviation of that ratio from $1/4$ at $\omega \gg \omega_\star$.)

Now, we compare the effect of disorder has on the waves' transmission with that on their reflection. By using the reflection coefficient (4.41) and assuming the flat distribution of θ_1 mentioned above Eq. (4.54), we find that, for $\omega_\star \ll \omega \ll \omega_{\mathrm{cr}}$, the
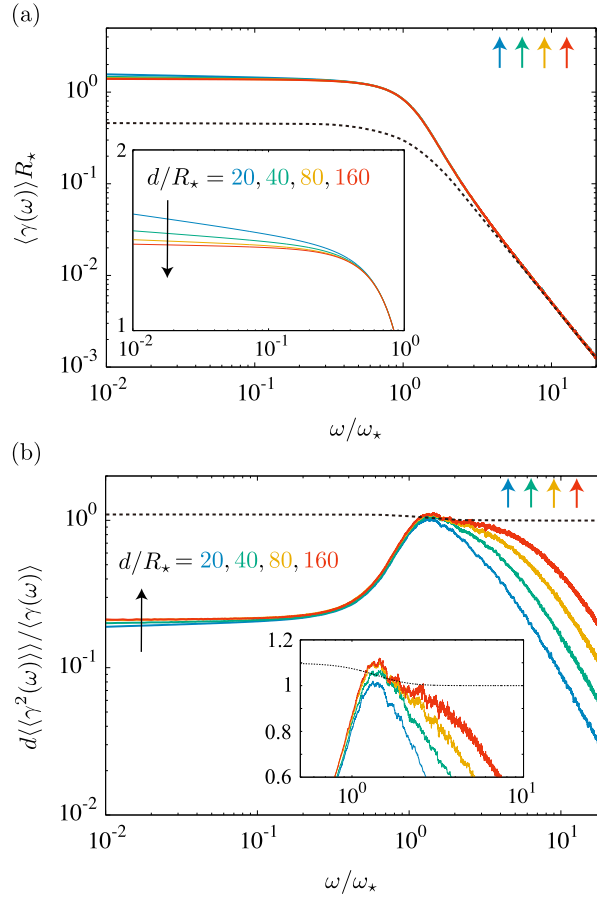
FIGURE 4.6: (a) The average of the Lyapunov exponent and (b) its variance as a function of frequency for different lengths $d/R_\star = 20, 40, 80,$ and 160 at $K/K_0 = 1.0$. Arrows indicate the crossover frequency ω_{cr} for each length. The inset is an enlarged view of the (a) low and (b) intermediate frequency regions. The dotted lines in panels (a) and (b) show the result of the Gaussian white-noise potential at $d \to \infty$ for comparisons. As d increases, the Lyapunov exponent approaches a constant value. At $\omega \gg \omega_\star$, $\langle \gamma(\omega) \rangle$ in the two models coincide, in agreement with the Thouless relation, $\langle \gamma(\omega) \rangle = [2\ell_\pi(\omega)]^{-1}$. At $\omega \ll \omega_\star$, the average exponent and its variance saturate to different values in the two models.

real part of the reflection coefficient averages to a frequency-independent value,

$$\langle r'(\omega) \rangle = -r_0. \tag{4.61}$$

This indicates that the averaged reflection coefficient is insensitive to disorder, in contrast to the averaged transmission, which is manifestly dependent on $\ell_\pi(\omega)$ (see Eqs. (4.53) and (4.56)). At higher frequency, $\omega_{\mathrm{cr}} \ll \omega \ll \omega_{\mathrm{cr}}/T_0$, and large impedance mismatch $T_0 \ll 1$, we use the same methods as the third case for the derivation of the simple transmission asymptote at $d \ll \ell(\omega)$ and $T_0 \ll 1$ to find

$$\langle r'(\omega) \rangle = -1 + \frac{T_0}{2} \sum_n P_1 \left(\frac{2\omega_n d}{v} \right). \tag{4.62}$$

This form expresses the inhomogeneous broadening of plasmon standing waves
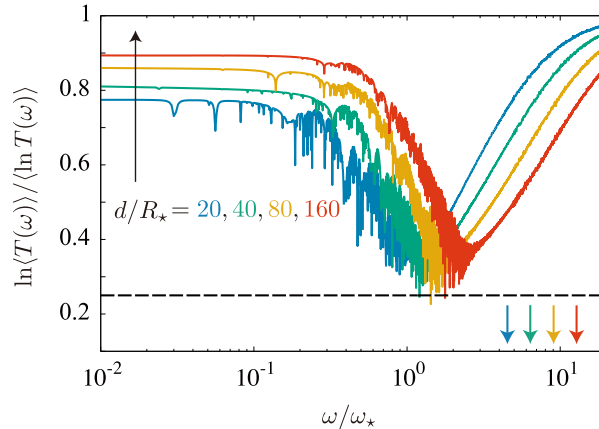
FIGURE 4.7: The frequency dependence of the ratio of $\ln \langle T(\omega) \rangle$ and $\langle \ln T(\omega) \rangle$ for different lengths $d/R_\star = 20, 40, 80$, and 160 at $K/K_0 = 1.0$. The ratio takes a frequency-independent value at low frequency, $\omega \ll \omega_\star$. As the frequency increases, it decreases while remaining above the value $1/4$ (dashed line) predicted in the frequency range $\omega_\star \ll \omega \ll \omega_{\mathrm{cr}}$, then it increases to the value 1 at larger frequencies. Arrows indicate the crossover frequency ω_{cr} for each length. A scaling analysis with the length gives the result $\ln \langle T(\omega) \rangle / \langle \ln T(\omega) \rangle \approx 0.90$ in the low-frequency limit $\omega/\omega_\star \to 0$ and $d/R_\star \to \infty$.

confined in the chain, in correspondence with Ref. [98]. Finally, the standard Fabry-Pérot formula for the reflection is recovered at $\omega \gg \omega_{\mathrm{cr}}/T_0$ when the levels' broadening is dominated by the radiation to waveguides, rather than inhomogeneous broadening.

4.4 Strongly localized regime

At low frequencies $\omega \ll \omega_\star$, plasmons are localized over a typical length $R_\star$, in the fluctuations of the effective disorder potential (4.16). Those fluctuations are non-Gaussian, and we have not been able to make an analytical theory of the scattering properties in that regime. However, we could gather several pieces of information from our numerical calculations. We compare them with known analytical results for the one-dimensional theory of localization in a Gaussian white-noise potential for which the additional function $w(x/R_\star)$ in Eq. (4.27) is replaced by zero. While the scattering properties of the two models coincide in the weakly localized regime ($\omega \gg \omega_\star$), important deviations appear in the strongly localized regime ($\omega \ll \omega_\star$). Below, we show the numerical results for the Lyapunov exponent, the reflection phase, and the transmission.

4.4.1 Lyapunov exponent

First, we discuss the average of the Lyapunov exponent and its variance. The Lyapunov exponent remains a self-averaging quantity, which saturates to a frequency-independent value, $\langle \gamma \rangle R_\star \approx 1.36$ at low frequencies, as shown in Fig. 4.6 (a). That value is larger than the one in the Gaussian white-noise model, $\langle \gamma \rangle R_\star = 3^{1/3} \times \sqrt{\pi}/\Gamma(1/6) \approx 0.46$ [145].

In agreement with the central limit theorem, we checked that the variance of the Lyapunov exponent scales inversely with d. The frequency dependence of the

ratio between the variance and average $\Sigma(\omega) = d \langle\langle \gamma^2(\omega) \rangle\rangle / \langle \gamma(\omega) \rangle$ is plotted in Fig. 4.6 (b). At low frequencies, numerical value marks $\Sigma \approx 0.218$, which is significantly smaller than the one in the Gaussian white-noise model at vanishing frequency, $\Sigma \approx 1.1$ [139]. Thus, a white-Gaussian disorder does not reproduce the right value of Σ, i.e., it emphasizes the role of non-Gaussian correlations in the effective potential created by the collective pinning effect.

The presented values of $\langle \gamma \rangle$ and Σ were obtained by brute-force numerical calculations of the dynamical plasmon propagation problem. Now, we show that these values are reproduced by solving the plasmon transmission problem for the static correlated random potential (4.16) upon averaging over its realizations. According to problem §25.5 in Ref. [146], the low-frequency transmission at perfect impedance matching ($K = K_0$) for the wave equation (4.10) is given by

$$T(\omega \to 0) \approx \frac{4\omega^2}{v^2 [\psi_0'(d)]^2}, \tag{4.63}$$

where $\psi_0(x)$ is the solution of Eq. (4.10) at $\omega = 0$ satisfying the boundary conditions $\psi_0(0) = 1$ and $\psi_0'(0) = 0$. Equation (4.63) works at the sufficiently small frequency for typical disorder configurations such that $\psi_0'(d) \neq 0$. Note that $\psi_0'(d) = 0$ would signal a zero-energy bound state, and resonant transmission, $T \approx 1$, is not captured by Eq. (4.63). An explicit solution of Eq. (4.10) reads

$$\psi_0(x) = \exp\left[\xi^{-1} \int_0^x dy\, Z(y) \right]. \tag{4.64}$$

Here, $Z(x) = R_\star \psi'(x)/\psi(x)$ is another Ricatti variable from z defined in Eq. (4.40), which solves an equation derived from Eq. (4.10) at $\omega = 0$,

$$R_\star \partial_x Z(x) = -Z^2(x) + \frac{\mathcal{V}(x)}{\omega_\star^2} \quad \text{with} \quad Z(0) = 0. \tag{4.65}$$

Then, the transmission (4.63) can be expressed in terms of the Ricatti variable as

$$T(\omega \to 0) \approx 4 \left(\frac{\omega}{\omega_\star} \right)^2 \frac{1}{Z^2(d)} \exp\left[-\frac{2}{R_\star} \int_0^d dy\, Z(y) \right]. \tag{4.66}$$

It was argued in Refs. [101, 102] that the solution of Eq. (4.65) with the correlated random potential (4.16) has a positive mean value, $\langle Z(x) \rangle > 0$. Thus, solving Eq. (4.65) provides another way to find the Lyapunov exponent and its variance from Eq. (4.66), which only depends on $\mathcal{V}(x)$, as mentioned above. This approach yields $\langle \gamma \rangle R_\star = 1.37$ and $\Sigma = 0.217$, which are very close agreement with the results of the brute-force numerical evaluation of scattering amplitudes at a low, but finite frequency, $\langle \gamma \rangle R_\star = 1.36$ and $\Sigma = 0.218$, respectively.

4.4.2 Reflection coefficient

When we enter the low-frequency regime, the transmission is exponentially suppressed and waves are almost perfectly reflected, $r(\omega) \approx 1$. In the limit of perfect impedance matching ($K = K_0$), we characterize the reflection coefficients with the distribution of the reflection phase [147, 148] (see Fig. 4.8). While the distribution is uniform at $\omega \gg \omega_\star$, a single-peak structure near $\theta_1 = \pm\pi$ develops at a lower frequency. At $\omega \ll \omega_\star$, the peak in the distribution obtained from the brute-force numerics takes a universal frequency dependence both in our model and in
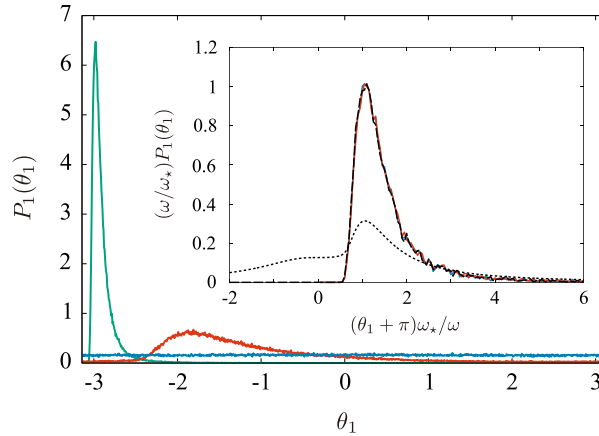
FIGURE 4.8: Probability distributions of the reflection phase θ_1 at $K/K_0 = 1.0$, $d/R_\star = 20$, $\omega/\omega_\star = 0.157$ (green), 1.16 (red), and 8.58 (blue). The inset shows the universal frequency dependence of the distribution found numerically in the vicinity of phase $\theta_1 = -\pi$ either by the brute force numerical calculations at $\omega/\omega_\star = 0.1$ (blue) and 0.25 (red), or from the solution of the Ricatti Eq. (4.65) (dashed line). The dotted line represents the analytical formula derived in Ref. [147] for a Gaussian white-noise disorder.

the Gaussian white-noise model, as shown in the inset of Fig. 4.8, with important differences between the two models. Furthermore, the universal dependence in our model agrees with the one obtained by solving numerically Eq. (4.65) in the interval $0 < x < d$ with a given boundary condition at $x = d$ for various disorder configurations. Then, we identify $Z(0) = -2(\omega/\omega_\star)/(\theta_1 + \pi)$, which is the consequence of the boundary conditions (4.11) and (4.13) with $K = K_0$, $\omega/\omega_\star \to 0$, and $r = e^{i\theta_1}$. The results do not depend on the boundary condition for $Z(d)$ if $d \gg R_\star$, e.g., $d/R_\star = 20$ in the inset of Fig. 4.8.

The distribution $P_1(\theta_1)$ of the reflection phase θ_1 can be seen as a measure of the modes localized nearby an end of the pinned region and their frequencies lie either above ($\theta_1 > -\pi$) or below ($\theta_1 < -\pi$) the one of the incoming waves. The distribution $P_1(\theta_1)$ appears to reach zero at $\theta_1 = -\pi$, unlike the white-noise Gaussian cases (see Appendix F), indicating the scarcity of low-frequency resonances. This agrees with the strong suppression of the low-frequency modes' density of states [100, 101, 102] in our pinned model, in contrast with the Gaussian models.

The distribution $P_1(\theta_1)$, together with Eqs. (4.11) and (4.13), allows us to find the statistics of the reflection phase at any impedance mismatch between the waveguide and half-infinite chain, i.e., $d/R_\star \to \infty$. In particular, the real part of the averaged reflection coefficient is

$$\langle r' \rangle + 1 = \int d\theta_1 \, P_1(\theta_1) \frac{2}{1 + (K_0/K)^2 \tan^2(\theta_1/2)}. \tag{4.67}$$

At $\omega \ll \omega_\star$, the frequency scaling of the peak in $P_1(\theta_1)$ near $\theta_1 = -\pi$, which is defined by

$$p(\varphi = (\theta_1 + \pi)\omega_\star/\omega) = (\omega/\omega_\star)P_1((\theta_1 + \pi)\omega_\star/\omega), \tag{4.68}$$
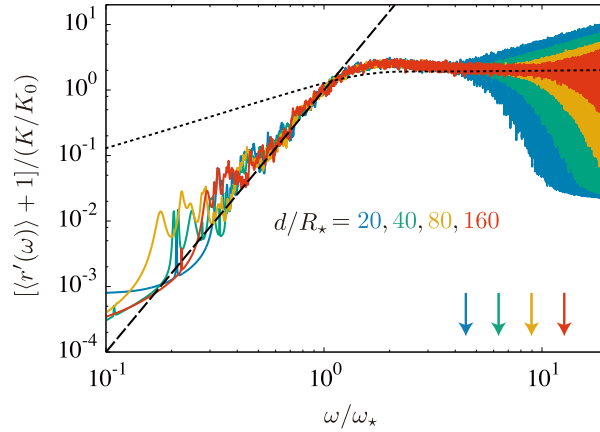
FIGURE 4.9: The frequency dependence of the local density of states at $K/K_0 = 0.01$. The dashed line represents $(\omega/\omega_\star)^4$. The pre-factor is also agreement with Ref. [98]. The dotted line is the result of the Gaussian white-noise model, (see Appendix F). Arrows indicate the crossover frequency ω_{cr} for each length, $d/R_\star = 20, 40, 80,$ and 160.

is independent of the frequency as demonstrated in the inset of Fig. 4.8. As a result, we obtain

$$\langle r' \rangle + 1 = A \left(\frac{K}{K_0} \right)^2 \left(\frac{\omega}{\omega_\star} \right)^2, \tag{4.69}$$

where the prefactor A can be evaluated by $A = \int d\varphi \, p(\varphi)\varphi^2 \approx 2.4$. At any $K \ll K_0$, another important contribution to Eq. (4.67), which scales linearly with K/K_0, comes from phase near $\theta_1 = 0$, yielding

$$\langle r' \rangle + 1 = 4\pi \frac{K}{K_0} P_1(\theta_1 = 0). \tag{4.70}$$

Our numerical result for $\langle r' \rangle$ at $K \ll K_0$, shown in Fig. 4.9, confirms the result of Ref. [98] and Eq. (4.70) with $P_1(\theta_1 = 0) \propto \omega^4$; in this regime $[\langle r'(\omega) \rangle + 1]/(K/K_0)$ can be interpreted as the local density of plasmon modes. However, we were not able to correlate this result with the result of a direct evaluation of $P_1(\theta_1 = 0)$ illustrated by Fig. 4.8, presumably due to an insufficient number of disorder configurations because configuration yielding $\theta_1 = 0$ is rare. Furthermore, the deviation of the numerical results from the ω^4-scaling seen in Fig. 4.9 at the lowest frequencies is suggestive of a crossover to the ω^2-scaling of Eq. (4.69); our numerical results did not allow us to check this scaling quantitatively. The different (K/K_0)-dependence of Eq. (4.70), compared with Eq. (4.69), ensures that it dominates over a wide frequency range. The scarcity of low-frequency modes reflects in a much stronger suppression of the local density of states $\propto \omega^4$ at $\omega \ll \omega_\star$ in our pinned model, in contrast with the results of the white-noise Gaussian models where $[\langle r'(\omega) \rangle + 1]/(K/K_0) \propto 1.29\omega/\omega_\star$ (see Appendix F).

4.4.3 Average transmission

At any frequency in the range, the averaged transmission is determined by the optimal configurations. Furthermore, the ratio $\ln \langle T \rangle / \langle \ln T \rangle$ remains smaller than 1, in accordance with the inequality between the arithmetic and geometric means. In Section 4.3.3, we found $\ln \langle T \rangle / \langle \ln T \rangle = 1/4$ in the diffusive regime ($\omega \gg \omega_\star$). In the

strongly localized regime, this ratio increases towards the value $\ln \langle T \rangle / \langle \ln T \rangle \approx 0.9$ (see Fig. 4.7). Its closeness to 1 indicates a small difference between the typical and optimal disorder configurations. This is further confirmed by the fact that ensemble-averaging of Eq. (4.63) yields a very close result for that ratio, $\ln \langle T \rangle / \langle \ln T \rangle \approx 0.93$. As disorder configurations with nearly-perfect transmission [131] are not taken into account in Eq. (4.63), they should have a negligible weight among the optimal disorder configurations.

Note that the frequency scaling $\langle T(\omega \to 0) \rangle \propto \omega^2$ in Eq. (4.66) confirms that, for the waves at the bottom of the plasmon spectrum, i.e., in the infinite wavelength limit, the disorder potential acts like a localized one for each realization of the disorder. Our numerical results do not have enough accuracy to check this asymptote quantitatively and to establish its range of validity.

For comparison, we expect disorder configurations with nearly-perfect transmission to play a major role at arbitrarily low frequency in the Gaussian models. This may result in a different frequency dependence of $\langle T(\omega) \rangle$ and $\ln \langle T(\omega) \rangle / \langle \ln T(\omega) \rangle$ at $\omega \ll \omega_\star$. As far as we know, this question has not been studied systematically. Our numerical results indicate $\ln \langle T(\omega) \rangle / \langle \ln T(\omega) \rangle \approx 0.72$ at $\omega \ll \omega_\star$ in the Gaussian white-noise model. We attribute the difference of the result from our pinned model result, $\ln \langle T(\omega) \rangle / \langle \ln T(\omega) \rangle \approx 0.9$, to the scarcity of low-frequency quasi-localized modes in the latter.

4.5 Short summary of this chapter

We investigated the transmission though the disordered Josephson-junction chain. In this thesis, we focused on the classical limit ($K \ll 1$), in which there is a competition between the elasticity and the pinning effect due to the disorder. By performing the numerical calculation in that regime, we obtained the frequency dependence of the transmission. For the high-frequency regime, the pinning effect is expected to be neglected naively because the wavelength is shorter than the Larkin length. Surprisingly, we found that the pinning-induced disorder still affects the forward-scattering length. On the other hand, for the low-frequency regime, we could gather the numerical pieces of the important quantities, such as the Lyapunov exponent, the reflection phase, the local density of states, and the ratio between the Lyapunov exponent and the logarithmic transmission and clarified the universality of the scattering property. Moreover, by comparing our model with the well-known model with the Gaussian white-noise disorder, we revealed that the correlations of the pinning-induced disorder play a crucial role in reproducing our results. Finally, we would like to stress that recent experimental technology enables us to fabricate the Josephson-junction chain with a small but finite K [88, 89]. Therefore, the theoretical prediction in this chapter can indeed be checked experimentally in the near future.

Chapter 5

Heat Transport through the Quantum Rabi System

In this chapter, we investigate heat transport through the quantum Rabi model [41]. First, we briefly review quantum heat transport in mesoscopic devices in Section 5.1. Then, we introduce the quantum Rabi model and formulate heat transport through it in Section 5.2. Using the noninteracting-blip approximation (NIBA), which is explained in Section 5.3, we present numerical results for the temperature dependence of the thermal conductance in Section 5.4.

5.1 Quantum heat transport

In this section, we introduce recent theoretical and experimental advances on quantum heat transport through a small object for which quantum mechanical effects become important at sufficiently low temperatures. In a pioneering theoretical work by John Pendry in 1983, he predicted that heat conducted by a single transport channel has a universal maximum at sufficiently low temperatures, which is known as a quantized thermal conductance [149]. This quantized thermal conductance can be observed for any type of carrier, e.g., phonons and photons. Based on the Landauer theory [150, 151], which has been developed for electric transport, the heat current for bosons between two heat baths, which are in thermal equilibrium, can be given by

$$J = \sum_n \frac{1}{h} \int_0^\infty d(\hbar\omega) \, \hbar\omega \mathcal{T}_n(\omega) \left[n_{\mathrm{L}}(\omega) - n_{\mathrm{R}}(\omega) \right], \tag{5.1}$$

where $n_i(\omega)$ is the Bose-Einstein distribution of the heat bath $i = \mathrm{L}, \mathrm{R}$, and $\mathcal{T}_n(\omega)$ is the transmission probability of the transport channel n. Here, assuming the perfect transmission, $\mathcal{T}_n(\epsilon) = 1$, and a small temperature gradient, $\delta T \equiv T_{\mathrm{L}} - T_{\mathrm{R}} \ll T$, we obtain the linear thermal conductance as

$$G \equiv \lim_{\delta T \to 0} \frac{J}{\delta T} = \mathcal{N} G_{\mathrm{Q}}, \tag{5.2}$$

where $\mathcal{N}$ is the number of transport channels and G_{Q} is the thermal conductance quantum

$$G_{\mathrm{Q}} = \frac{\pi^2 k_{\mathrm{B}}^2}{3h} T. \tag{5.3}$$

In 2000, it has been observed experimentally for the first time that phonons in nanobridges conduct heat with the linear thermal conductance G_{Q} per a transport channel [152].
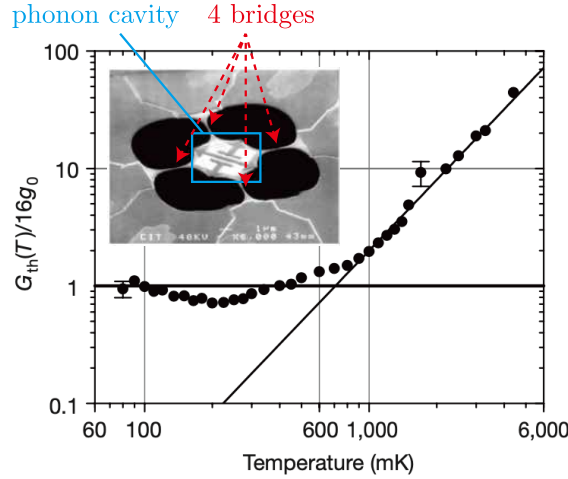
FIGURE 5.1: View for the quantized thermal conductance in a phononic system. The inset shows the suspended device, in which a $4 \times 4\,\mu\text{m}^2$ phonon cavity (the bright area in the center) patterned from the membrane is connected to four thin-film Nb bridges, phonon waveguides whose diameter at the narrowest point is less than 200 nm. In the dark regions, the membrane has been completely removed. The main panel shows the temperature dependence of the thermal conductance normalized by $16g_0$ ($16G_Q$ in the main text). These figures are taken from Ref. [152].
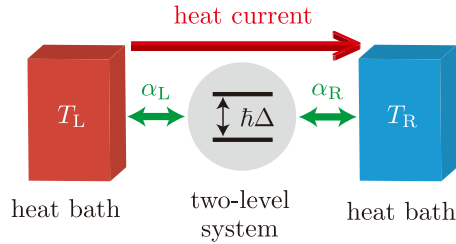
FIGURE 5.2: Schematic of heat transport through a two-level system between two bosonic heat baths. For $T_L > T_R$, the heat current flows from the left heat bath to the right heat bath.

Fig. 5.1 presents the measured thermal conductance, renormalized by $16G_Q$, through nanobridgeds as a function of temperature. At high temperatures, $T \gtrsim 0.8$ K, the thermal conductance shows the usual T^3-dependence due to the phonon scatterings. Below this temperature, $T \lesssim 0.8$ K, the thermal conductance levels off a value near the quantized thermal conductance, $16G_Q$. In Ref. [152], it was discussed that coefficient 16 consists of 4 from four independent bridges and 4 from four acoustic vibration modes in each bridge. Later, the quantized thermal conductance has also seen in other systems; the superconducting circuit with microwave photons [153, 154].

As described in Section 2.8, the superconducting circuit is a convenient platform for the study of quantum heat transport. One of the most fundamental systems is a superconducting qubit embedded in two thermal photon baths fabricated in superconducting circuits, as shown in Fig 5.2. As described in Section 2.5, quantum heat transport for this system can be described by the spin-boson model. The theoretical study by the author of this thesis for the spin-boson model [38] has systematically clarified the transport processes for all types of heat baths (the Ohmic bath $s = 1$,
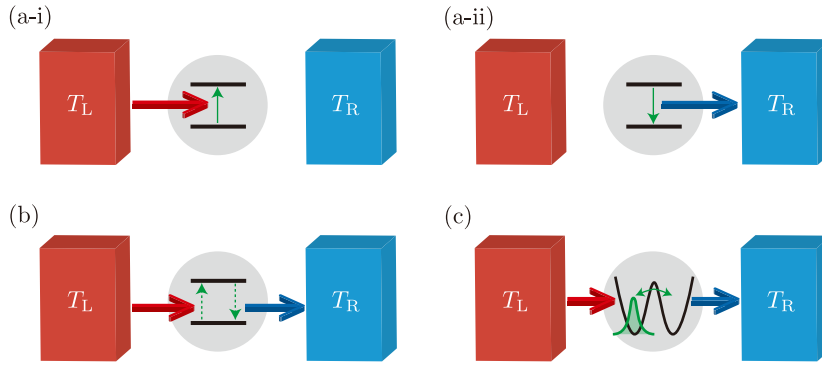
FIGURE 5.3: Three transport processes of heat transport through a two-level system. (a) At weak couplings and temperatures comparable to the renormalized tunneling splitting energy, one photon absorption (a-i) and emission (a-ii) processes are relevant; sequential tunneling process. (b) At low temperatures, heat is carried by the virtual excitation processes; the co-tunneling process. (c) At high temperatures or strong couplings, heat transport is caused by the stochastic transition between two degenerate states localized in each well; incoherent tunneling process.

the sub-Ohmic bath $s < 1$, and the super-Ohmic bath $s > 1$ categorized by the exponent s of the spectral function; see Eq. (2.39)) by using the quantum Monte Carlo simulations. Depending on the exponent of the spectral function s, the temperature $T = T_L + 0 = T_R - 0$, and the coupling strength $\alpha = \alpha_L = \alpha_R$, the relevant transport process changes (see Fig. 5.3). At weak couplings, $\alpha \ll 1$, and the intermediate temperature, $k_B T \sim \hbar\tilde{\Delta}$, where $\tilde{\Delta}$ is a renormalized tunneling splitting frequency, one photon absorption and emission processes cause dominantly heat transport (Fig. 5.3 (a); sequential tunneling process). As the temperature decreases, $k_B T \ll \hbar\tilde{\Delta}$, one photon processes, i.e., the sequential tunneling process, are suppressed and then a virtual excitation associated with higher-order processes is relevant for heat transport (Fig. 5.3 (b); co-tunneling process). This transport process is associated with the Kondo effect, as discussed in Section 2.5. At high temperatures, $k_B T \gg \hbar\tilde{\Delta}$, or strong coupling, $\alpha > 1$, the quantum coherence of the two-level system is broken and then heat transport is induced by a stochastic transition between two degenerate states localized in each well (Fig. 5.3 (c); incoherent tunneling process).

Thus, heat transport through a two-level system provides a concrete theoretical basis for describing quantum heat transport. However, it is too simple for the discussion of sophisticated control of quantum heat devices because the number of independent model parameters is not large. We also note that recent experiments on heat transport through an assembly consisting of a superconducting qubit capacitively embedded between two superconducting resonators have indicated complex functions as a quantum heat device [104, 106]. From the next section, we consider a two-level system embedded between harmonic resonators, which is one of the more ubiquitous devices in the current quantum computing toolbox, instead of a two-level system for studying quantum heat transport.

5.2 Formalism for heat transport

In this section, we formulate heat transport through the quantum Rabi model in the ultra-strong coupling regime. By using the exact mapping to the spin-boson

model with structured heat baths, we derive the linear thermal conductance and its asymptotic form for the weak dissipation.

5.2.1 Dissipative quantum Rabi model and spin-boson model

To treat heat transport through a two-level system embedded between harmonic resonators, we consider the dissipative quantum Rabi model (see Fig. 5.4), whose Hamiltonian consists of three parts:

$$\mathcal{H} = \mathcal{H}_R + \sum_r (\mathcal{H}_{B,r} + \mathcal{H}_{I,r}). \tag{5.4}$$

Here, $\mathcal{H}_R$ represents the quantum Rabi model describing the two-level system embedded between harmonic resonators (indicated by the central part of Fig. 5.4 (a) enclosed by the dashed line), $\mathcal{H}_{B,r}$ the heat bath r ($=$ L, R), and $\mathcal{H}_{I,r}$ the coupling between the harmonic resonator r and the heat bath r. Although the Hamiltonian of the quantum Rabi model, $\mathcal{H}_R$, has already been given in Section 2.4, we briefly repeat it here. The quantum Rabi model describes a two-level system coupled to harmonic resonators and its Hamiltonian is given by

$$\mathcal{H}_R = -\frac{\hbar\Delta}{2}\sigma_x + \sum_r \hbar\Omega_r a_r^\dagger a_r + \sum_r \hbar g_r \sigma_z \left(a_r + a_r^\dagger\right), \tag{5.5}$$

where a_r ($a_r^\dagger$) is an annihilation (a creation) operator of the harmonic resonator r ($=$ L, R), $\sigma_{i=\{x,y,z\}}$ are the Pauli matrices, and Δ is a tunneling splitting frequency of the two-level system. Ω_r is a natural frequency of the harmonic resonator r, and the frequency g_r represents the coupling strength between the two-level system and the harmonic resonator r. Here, we have dropped a detunning term of the two-level system for simplicity.

The two heat baths coupled to harmonic resonators are modeled as a collection of harmonic oscillators. The Hamiltonian of the heat bath r ($=$ L, R) is given as

$$\mathcal{H}_{B,r} = \sum_k \hbar\omega_{r,k} b_{r,k}^\dagger b_{r,k} \tag{5.6}$$

with an annihilation (a creation) operator $b_{r,k}$ ($b_{r,k}^\dagger$) of the k-th bosonic mode with the frequency $\omega_{r,k}$ in the heat bath r. The heat baths and the quantum Rabi model are coupled to each other via the harmonic resonators:

$$\mathcal{H}_{I,r} = \sum_k \hbar\lambda_{r,k} \left(a_r + a_r^\dagger\right) \left(b_{r,k} + b_{r,k}^\dagger\right), \tag{5.7}$$

where the frequency $\lambda_{r,k}$ represents the coupling strength between the harmonic resonator r and the k-th bosonic mode in the heat bath r. As discussed in Section 2.5, each of the heat baths is completely characterized by a spectral density

$$I_r(\omega) \equiv \sum_k \lambda_{r,k}^2 \delta\left(\omega - \omega_{r,k}\right). \tag{5.8}$$

In this thesis, we consider the Ohmic heat baths (see also Section 2.5):

$$I_r(\omega) = 2\eta_r\omega. \tag{5.9}$$
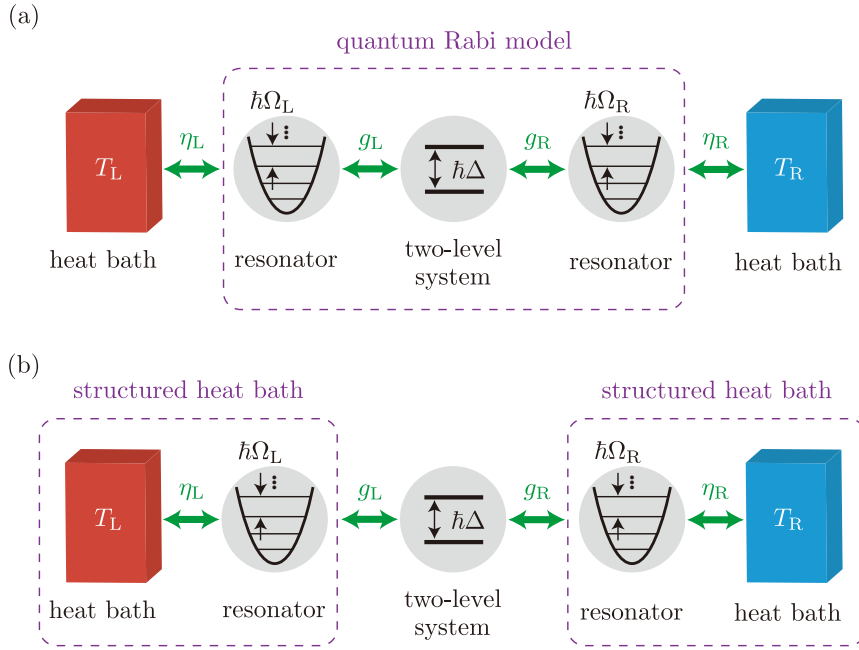
FIGURE 5.4: Schematic illustrations of the model considered in this chapter. A two-level system with the tunneling splitting frequency Δ is embedded between two harmonic resonators with natural frequencies Ω_L and Ω_R which contacts to an Ohmic bath L and R, respectively. The finite temperature difference ($T_L > T_R$) induces heat transport from the left (hotter) heat bath to the right (cooler) heat bath. Two ways of viewing the model; (a) the quntum Rabi model coupled to two Ohmic heat baths which is called the dissipative quantum Rabi model and (b) the two-level system coupled to two structured heat baths composed of the harmonic resonator and the Ohmic heat bath, which is equivalent to the spin-boson model. In this thesis, we consider the symmetric case, $\Omega_L = \Omega_R = \Omega$, $g_L = g_R = g$, and $\eta_L = \eta_R = \eta$.

Here, η_r represents a dimensionless coupling strength between the heat bath r and the harmonic resonator r.

Now, let us introduce the exact mapping of the model considered here by changing the way of viewing the model; from the quantum Rabi model coupled to Ohmic heat baths, as shown in Fig. 5.4 (a), to the two-level system coupled to structured heat baths, as shown in Fig. 5.4 (b). Then, the dissipative quantum Rabi model (5.4) can be mapped to the spin-boson model (see the detail derivation in Appendix H) [155, 156, 83]:

$$\mathcal{H}_{\text{sb}} = \mathcal{H}_{\text{TLS}} + \mathcal{H}_{\text{B}} + \mathcal{H}_{\text{I}}, \tag{5.10}$$

$$\mathcal{H}_{\text{TLS}} = -\frac{\hbar\Delta}{2}\sigma_x, \tag{5.11}$$

$$\mathcal{H}_{\text{B}} = \sum_r \mathcal{H}_{\text{B},r} = \sum_{k,r} \hbar\Xi_{r,k} B_{r,k}^\dagger B_{r,k}, \tag{5.12}$$

$$\mathcal{H}_{\text{I}} = \sum_r \mathcal{H}_{\text{I},r} = -\frac{\sigma_z}{2}\sum_{k,r} \hbar\Lambda_{r,k}\left(B_{r,k} + B_{r,k}^\dagger\right), \tag{5.13}$$

where $B_{r,k}$ ($B_{r,k}^\dagger$) is an annihilation (a creation) operator for the k-th bosonic mode with the frequency $\Xi_{r,k}$ in a new heat bath r, composed of the bare heat bath and

the harmonic resonator, and $\Lambda_{r,k}$ represents the coupling strength between the two-level system and the k-th bosonic mode in the new heat bath r. The spectral density characterizing the effective heat baths is expressed by

$$I_{\text{eff},r}(\omega) \equiv \sum_k \Lambda_{r,k}^2 \delta(\omega - \Xi_{r,k}) = 2\alpha_r \omega \frac{\Omega_r^4}{(\Omega_r^2 - \omega^2)^2 + (2\Gamma_r \omega)^2}, \tag{5.14}$$

which is called as a structured spectral density. The spectral density $I_{\text{eff},r}(\omega)$ has a peak at the natural frequency of the harmonic resonator, Ω_r, with the width, $\Gamma_r = \pi \eta_r \Omega_r$, and its height is characterized by the dimensionless coupling strength $\alpha_r = \eta_r (4g_r / \Omega_r)^2$.

At the end of this subsection, we comment on the region of $\Delta \ll \Omega_r$. In this region, since the lowest two states of the quantum Rabi model are separated well from the other, the dissipative quantum Rabi model can be regarded as the Ohmic spin-boson model. This correspondence can also be seen from the spectral density (5.14), i.e., the structured part of the spectral density can be neglected and then it becomes Ohmic, $I_{\text{eff},r}(\omega) \sim 2\alpha_r \omega$. Therefore, heat transport in this regime can be understood by simply referring to the results on heat transport in the Ohmic spin-boson model, as discussed in Section 5.1. This parameter regime is not preferable to control heat transport because this effective two-level system shows a rather simple behavior for heat transport with respect to the parameters. In fact, the degrees of freedom regarding the harmonic resonators, i.e., Ω_r, g_r, and η, are absorbed into a renormalized tunneling splitting frequency Δ_*. In this thesis, we focus on the opposite region, $\Delta \gtrsim \Omega$, in which the present model is expected to exhibit non-trivial transport properties.

5.2.2 Linear thermal conductance

The heat current mediated via the quantum Rabi model from the heat bath r is defined as

$$J_r \equiv -\frac{d\mathcal{H}_{\text{B},r}}{dt}. \tag{5.15}$$

Using the picture of the spin-boson model with the structured heat bath (5.10), the steady state heat current is formulated by the Keldysh formalism as [157, 158, 107]

$$\langle J_r \rangle = \frac{\hbar^2}{2} \int_0^\infty d\omega \, \omega I_{\text{eff},r}(\omega) \left\{ \text{Im}\left[\chi^{\text{R}}(\omega)\right] n_r(\omega) - \frac{i}{2} \chi^<(\omega) \right\}, \tag{5.16}$$

where $n_r(\omega) = 1/(e^{\beta_r \omega} - 1)$ is the Bose-Einstein distribution for the structured heat bath r, $\beta_r = 1/k_{\text{B}} T_r$ is the inverse temperature, k_{B} is the Boltzmann constant, and T_r is the temperature of the heat bath r (for a detailed derivation, see Appendix G). The retarded and lesser components of the spin correlation function of the two-level system are defined as

$$\chi^{\text{R}}(t) \equiv -\frac{i}{\hbar} \theta(t) \langle [\sigma_z(t), \sigma_z(0)] \rangle, \tag{5.17}$$

$$\chi^<(t) \equiv -\frac{i}{\hbar} \langle \sigma_z(t) \sigma_z(0) \rangle, \tag{5.18}$$

respectively. For simplicity, we consider the symmetric case, $\Omega_{\text{L}} = \Omega_{\text{R}} \equiv \Omega$, $g_{\text{L}} = g_{\text{R}} \equiv g$, and $\eta_{\text{L}} = \eta_{\text{R}} \equiv \eta$ in this thesis. Using the energy conservation law, $\langle J_{\text{L}} \rangle +

$\langle J_R \rangle = 0$, we finally obtain the heat current as

$$\langle J_L \rangle = \frac{\alpha \gamma \hbar^2}{8} \int_0^\infty d\omega \, \omega \tilde{I}_{\text{eff}}(\omega) \text{Im} \left[\chi^R(\omega) \right] \left[n_L(\omega) - n_R(\omega) \right] \tag{5.19}$$

with $\alpha = \alpha_L + \alpha_R$, $\gamma = 4\alpha_L \alpha_R / \alpha^2$, and $\tilde{I}_{\text{eff}}(\omega) = \alpha_r^{-1} I_{\text{eff},r}(\omega)$.

Using the expression of the heat current, we obtain the linear thermal conductance as

$$\kappa \equiv \lim_{T_L, T_R \to T} \frac{\langle J_L \rangle}{T_L - T_R} \tag{5.20}$$

$$= \frac{\alpha \gamma \hbar k_B}{8} \int_0^\infty d\omega \, \tilde{I}_{\text{eff}}(\omega) \text{Im} \left[\chi^R(\omega) \right] \left[\frac{\beta \hbar \omega / 2}{\sinh(\beta \hbar \omega / 2)} \right]^2 . \tag{5.21}$$

For the convenience of analysis, we introduce a symmetrized correlation function,

$$S(t) = \frac{1}{2} \langle \sigma_z(t) \sigma_z(0) + \sigma_z(0) \sigma_z(t) \rangle . \tag{5.22}$$

From the fluctuation-dissipation theorem [17], the imaginary part of the retarded component of the spin correlation function is related to the symmetrized correlation function as

$$S(\omega) = \hbar \coth \left(\frac{\beta \hbar \omega}{2} \right) \text{Im} \left[\chi^R(\omega) \right] . \tag{5.23}$$

Then, the linear thermal conductance is rewritten as

$$\kappa = \frac{\alpha \gamma k_B}{16} \int_0^\infty d\omega \, \tilde{I}_{\text{eff}}(\omega) S(\omega) \frac{(\beta \hbar \omega)^2}{\sinh(\beta \hbar \omega)} . \tag{5.24}$$

Due to the factor $(\beta \hbar \omega)^2 / \sinh(\beta \hbar \omega)$ in the integral, the behavior of the linear thermal conductance is mainly determined by the symmetrized correlation function in the region of $0 < \omega \lesssim k_B T / \hbar$.

5.2.3 Weak-dissipation regime

Here, we consider the behavior of the linear thermal conductance for the weak dissipation, i.e., $\eta \ll 1$. First, we look at the non-dissipative quantum Rabi model, $\eta = 0$, for which the eigenstates and their energy are denoted as $|n\rangle$ and $\hbar \omega_n$, respectively:

$$\mathcal{H}_R |n\rangle = \hbar \omega_n |n\rangle , \quad (n = 0, 1, 2, \dots) . \tag{5.25}$$

Then, the symmetrized correlation function $S(\omega)$ is described as

$$S(\omega) = \frac{\pi}{Z_R} \sum_{n,m} e^{-\beta \hbar \omega_m} |\langle n|\sigma_z|m\rangle|^2 \left[\delta(\omega - \omega_{nm}) + \delta(\omega + \omega_{nm}) \right] , \tag{5.26}$$

where Z_R is the partition function of the quantum Rabi model and $\omega_{nm} = \omega_n - \omega_m$ is the transition frequency between the m-th and n-th states. When switching slowly on the dissipation η, the peaks in $S(\omega)$ have finite widths from the delta-function ones. In general, their positions and widths vary as the dissipation increases. However, in the weak-dissipation regime ($\eta \ll 1$) these effects are weak enough that the

expression of $S(\omega)$ in the non-dissipative quantum Rabi model (5.26) can be used approximately.

At low temperatures, the behavior of $S(\omega)$ is determined mainly by transitions from the ground state. Then, the symmetrized correlation function is approximated as

$$S(\omega) \approx \pi \sum_n |\langle n|\sigma_z|0\rangle|^2 \left[\delta(\omega - \omega_{n0}) + \delta(\omega + \omega_{n0})\right].$$
(5.27)

By substituting this expression into Eq. (5.24), the linear thermal conductance is obtained as

$$\kappa \approx \frac{\pi\alpha\gamma k_B}{16} \sum_n |\langle n|\sigma_z|0\rangle|^2 \tilde{I}_{\text{eff}}(\omega_{n0}) \frac{(\beta\hbar\omega_{n0})^2}{\sinh(\beta\hbar\omega_{n0})}.$$
(5.28)

As a simple example, let us consider the case that the temperature is comparable to the first transition energy, $k_B T \sim \hbar\omega_{10}$, and the first transition energy is much smaller than the other, $\omega_{10} \ll \omega_{n0}$ ($n \geq 2$). For this case, the thermal conductance is approximated as

$$\kappa \approx \frac{\pi\alpha\gamma k_B}{16} \tilde{I}_{\text{eff}}(\omega_{10}) \frac{(\beta\hbar\omega_{10})^2}{\sinh(\beta\hbar\omega_{10})}.$$
(5.29)

From this expression, the thermal conductance shows the Schottky-type temperature dependence [36, 37, 23, 38]; it has a peak near $\hbar\omega_{10}/k_B$ and shows exponential suppression, $\kappa(T) \sim T^{-2}e^{-\hbar\omega_{10}/k_B T}$, for $k_B T \ll \hbar\omega_{10}$. When the transition energy to the second excited state, $\hbar\omega_{20}$, is also comparable to the temperature, the linear thermal conductance is approximated as a sum of the two Schottky functions. This implies that the linear thermal conductance is expected to have two peak structure as a function of the temperature. We will discuss this characteristic behavior numerically in Section 5.4 in detail. The weak-dissipation approximation discussed here is useful for qualitative discussion on the temperature dependence of the linear thermal conductance. However, since the dissipation indeed affects the peak positions and peak broadening, we need a more sophisticated approximation for quantitative discussion. In the next section, we will introduce an alternative approximation.

5.3   Non-interacting blip approximation

In this section, we introduce the noninteracting-blip approximation (NIBA), which works well in a wide parameter region including the strong system-bath coupling regime [16, 17, 38], and apply it to the linear thermal conductance.

First, let us consider the time evolution of the population $\langle\sigma_z(t)\rangle$. It is described by the generalized master equation

$$\frac{d\langle\sigma_z(t)\rangle}{dt} = -\int_0^t dt' \, K_z(t - t') \langle\sigma_z(t')\rangle.$$
(5.30)

Here, the kernel $K_z(t)$ can describe non-Markivian dynamics of the population $\langle\sigma_z(t)\rangle$. Although, in general, the non-local kernel is a complicated structure, it takes a simple form in the NIBA [16, 17],

$$K_z(t) = \Delta^2 e^{-Q'(t)} \cos Q''(t),$$
(5.31)

where $Q(t) = Q'(t) + iQ''(t)$ is the complex bath correlation function, the real and imaginary parts are

$$Q'(t) = \int_0^\infty d\omega \, \frac{I_{\text{eff}}(\omega)}{\omega^2} \coth\left(\frac{\beta\hbar\omega}{2}\right)(1 - \cos\omega t), \tag{5.32}$$

$$Q''(t) = \int_0^\infty d\omega \, \frac{I_{\text{eff}}(\omega)}{\omega^2} \sin\omega t, \tag{5.33}$$

respectively, with $I_{\text{eff}}(\omega) = I_{\text{eff,L}}(\omega) + I_{\text{eff,R}}(\omega)$. When the spectral density is the structured one as Eq. (5.14), we can calculate the complex bath correlation function explicitly as follows [159, 83]:

$$Q'(t) = \pi\alpha\left[\frac{2}{\hbar\beta}t - L\left(e^{-\Gamma t}\cos\bar{\Omega}t - 1\right) - Ze^{-\Gamma t}\sin\bar{\Omega}t + Q'_{\text{Mats}}(t)\right], \tag{5.34}$$

$$Q''(t) = \pi\alpha\left[1 - e^{-\Gamma t}\left(\cos\bar{\Omega}t - N\sin\bar{\Omega}t\right)\right], \tag{5.35}$$

where

$$\bar{\Omega} = \sqrt{\Omega^2 - \Gamma^2}, \quad N = \frac{\Omega^2 - 2\Gamma^2}{2\Gamma\bar{\Omega}}, \tag{5.36}$$

$$L = \frac{N\sinh(\beta\hbar\bar{\Omega}) - \sin(\beta\hbar\Gamma)}{\cosh(\beta\hbar\bar{\Omega}) - \cos(\beta\hbar\Gamma)}, \tag{5.37}$$

$$Z = \frac{\sinh(\beta\hbar\bar{\Omega}) + N\sin(\beta\hbar\Gamma)}{\cosh(\beta\hbar\bar{\Omega}) - \cos(\beta\hbar\Gamma)}, \tag{5.38}$$

and $Q'_{\text{Mats}}(t)$ is a series with respect to the Matsubara frequency, $\nu_n = 2\pi n/(\hbar\beta)$,

$$Q'_{\text{Mats}}(t) = \frac{4\Omega^4}{\hbar\beta}\sum_{n=1}^\infty \frac{1}{\nu_n}\frac{1 - e^{-\nu_n t}}{(\Omega^2 + \nu_n^2)^2 - (2\Gamma\nu_n)^2}. \tag{5.39}$$

The symmetrized correlation function $S(\omega)$ can be related to the non-local kernel as [17]

$$S(\omega) = \text{Re}\left[\frac{2}{-i\omega + \hat{K}_z(-i\omega)}\right], \tag{5.40}$$

where $\hat{K}_z(\lambda)$ is the Laplace transformation of $K_z(t)$. By using Eqs. (5.31)-(5.40) and (5.24), we can calculate the linear thermal conductance numerically within the NIBA. In general, the NIBA is justified at arbitrary temperatures for the weak system-bath coupling or for incoherent transport realized at the high temperature or the strong system-bath coupling [17, 16]. Moreover, even when the system-bath coupling is not weak, the NIBA fails at sufficiently low temperatures where heat transport is induced by virtual excitations, i.e., the co-tunneling process is dominant (see Section 5.1) [38]. However, the deviation from the exact results remains small as far as the system-bath coupling is sufficiently weak.

5.4 Numerical results

In this section, we present the numerical results for the symmetrized correlation function and the linear thermal conductance using the NIBA for $\Omega \lesssim \Delta$, where heat transport is expected to be non-trivial, as discussed in Section 5.2.
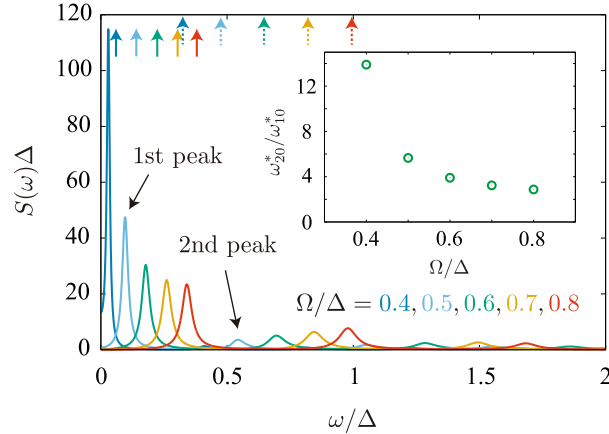
FIGURE 5.5: Symmetrized correlation function $S(\omega)$ as a function of the frequency for different Ω/Δ at fixed other parameters as $g/\Delta = 0.5$, $\eta = 0.01$, $k_{\rm B}T/(\hbar\Delta) = 0.01$. The symmetrized correlation function has several peaks and the peaks at the lower frequency are more dominant. The black arrows indicate the first peak at $\omega_{10}^*/\Delta = 0.096$ and the second one at $\omega_{20}^*/\Delta = 0.54$ at $\Omega/\Delta = 0.5$. The solid and dotted arrows represent the lowest two transition frequencies of the non-dissipative quantum Rabi model, ω_{10} and ω_{20}, respectively, which are obtained by the exact diagonalization of the non-dissipative quantum Rabi model. The inset represents a ratio between the frequencies of the first and second peaks, $\omega_{10}^*/\omega_{20}^*$, as a function of Ω/Δ.

5.4.1   Symmetrized correlation function

First, we show the symmetrized correlation function, $S(\omega)$, in Fig. 5.5 for $g/\Delta = 0.5$, $\eta = 0.01$, and $k_{\rm B}T/(\hbar\Delta) = 0.01$. From this figure, the symmetrized correlation function has several peaks corresponding to the transition frequencies of the dissipative quantum Rabi model, as indicated by the approximation for the weak dissipation (see Section 5.2). This multi-peak structure derives from the multilevel property of the quantum Rabi model. However, the peak positions are slightly shifted from the transition frequencies of the non-dissipative quantum Rabi model due to the dissipation even for small dissipation, $\eta = 0.01$. For later discussion, we introduce the renormalized frequencies ω_{n0}^* corresponding to the n-th peak in the symmetrized correlation function.

5.4.2   Linear thermal conductance

Next, we consider the linear thermal conductance. Fig. 5.6 (a) shows the temperature dependence of the linear thermal conductance for $g/\Delta = 0.5$, $\eta = 0.01$, and different Ω/Δ. For $\Omega/\Delta = 0.4$, it is clear that there are two peaks in the temperature dependence. We also see that the two-peak structure becomes less significant as Ω/Δ increases from 0.4 to 0.8. This feature originates from the first and second peaks of the symmetrized correlation function, ω_{10}^* and ω_{20}^*, respectively (see Fig. 5.5). Then, its temperature dependence can be qualitatively described by the sum of the two Schottky-type functions, $T^{-2}e^{-\hbar\omega_{10}^*/k_{\rm B}T}$ and $T^{-2}e^{-\hbar\omega_{20}^*/k_{\rm B}T}$, which leads to the two-peak structure. The two-peak structure is a signature of the multilevel property of the quantum Rabi model and can be clearly observed only when the symmetrized correlation function has sharp well-separated peaks. We show the temperature dependence of the linear thermal conductance for $\Omega/\Delta = 0.5$, $g/\Delta = 0.5$, and different
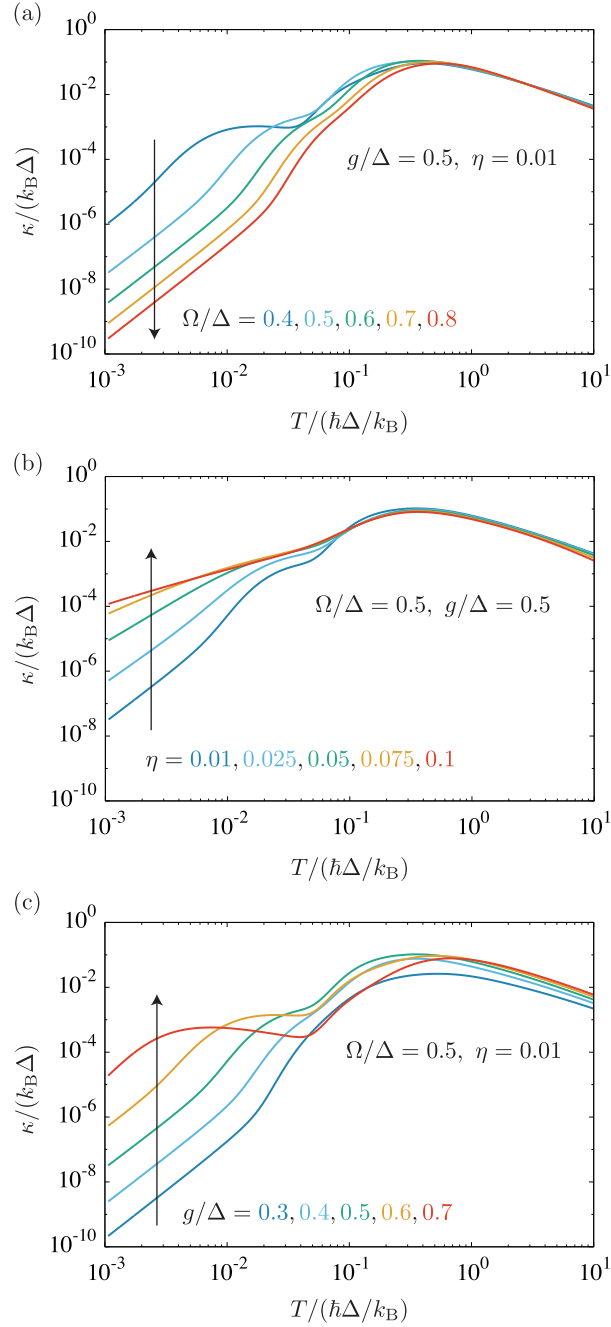
FIGURE 5.6: Temperature dependence of the linear thermal conductance for $\Omega/\Delta = 0.5$, $g/\Delta = 0.5$, and $\eta = 0.01$. When varying (a) $\Omega/\Delta = 0.4 - 0.8$, (b) $\eta = 0.01 - 0.1$, and (c) $g/\Delta = 0.3 - 0.7$, the linear thermal conductance considerably changes between the one- and two-peak structures.
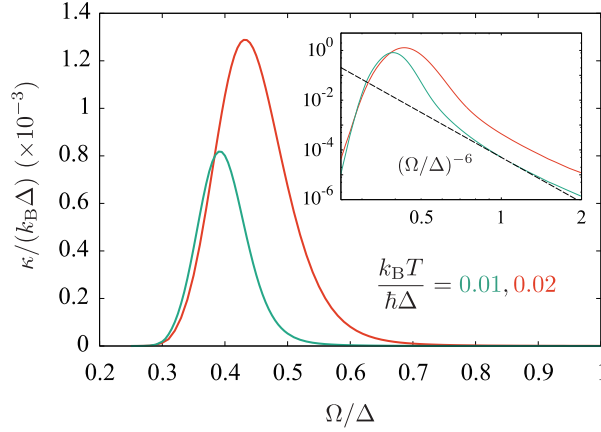
FIGURE 5.7: Linear thermal conductance as a function of Ω/Δ for $g/\Delta = 0.5$, $\eta = 0.01$, and different temperatures $k_B T/(\hbar\Delta) = 0.01$ and 0.02. The inset is an enlarged view of the high-frequency side of the peak frequency. The dashed line represents a guide for the power law $(\Omega/\Delta)^{-6}$.

η in Fig. 5.6 (b). As η increases from 0.01 to 0.1, the peak at the low-temperature side becomes less significant. This is because the peaks in the symmetrized correlation function are broadened due to the dissipation and are smoothed out them after performing the integral in Eq. (5.24).

Now, let us discuss the detailed condition for the appearance of the two-peak structure in the linear thermal conductance (5.24). If the peaks in the symmetrized correlation function are sufficiently sharp, the linear thermal conductance is approximately evaluated as

$$\kappa(T) \sim a_1 \frac{e^{-1/\tilde{T}}}{(k_B T)^2} + a_2 \frac{e^{-(\omega_{20}^*/\omega_{10}^*)/\tilde{T}}}{(k_B T)^2}, \tag{5.41}$$

where $\tilde{T} = k_B T/(\hbar\omega_{10}^*)$ and the prefactors are

$$a_n = \frac{\pi\alpha\gamma k_B}{8} |\langle n| \sigma_z |0\rangle|^2 (\hbar\omega_{n0}^*)^2 \tilde{I}_{\text{eff}}(\omega_{n0}^*). \tag{5.42}$$

From this expression, one can see that the condition $\omega_{20}^*/\omega_{10}^* \gg 1$ is required to have the two-peak structure in the temperature dependence of the linear thermal conductance. Note that although the ratio between a_1 and a_2 contributes to the appearance of the two peaks, it is almost irrelevant. This condition can be confirmed by the comparison between Fig. 5.5 and Fig. 5.6 (a). As Ω/Δ increases from 0.4 to 0.8, the ratio $\omega_{20}^*/\omega_{10}^*$ is reduced from 13.9 to 2.87, as shown in the inset of Fig. 5.5. With the decreasing of $\omega_{20}^*/\omega_{10}^*$, the two-peak structure becomes less significant (see main panel in Fig. 5.6 (a)). This feature can be also observed from the dependence of the hybridization constant g. Fig. 5.6 (c) shows the temperature dependence of the linear thermal conductance for $\Omega/\Delta = 0.5$, $\eta = 0.01$, and different g/Δ. It is observed that as g/Δ increases from 0.3 to 0.7, the two-peak structure becomes more significant. This is because the ratio $\omega_{20}^*/\omega_{10}^*$ is enlarged due to the level repulsion as the hybridization g increases.

When we choose the parameters for which the two-peak structure is clearly observed, the linear thermal conductance is sensitive to the parameters, particularly to Ω/Δ. In Fig. 5.7, we show the linear thermal conductance as a function of Ω/Δ

for two different temperatures. The linear thermal conductance has a sharp peak at $\Omega = \Omega_0$, where $\Omega_0/\Delta \approx 0.40$ and 0.44 for $k_\mathrm{B}T/(\hbar\Delta) = 0.01$ and 0.02, respectively. While it decays exponentially in the smaller Ω/Δ side of the peak, it shows a power-law decay in the opposite side, whose exponent is -6 (see the inset in Fig. 5.7). The strong dependence of Ω/Δ has an advantage for the application of heat transistor or heat valve in mesoscopic heat devices.

Now, we comment on the power-law decay for large Ω/Δ in the linear thermal conductance as a function of Ω/Δ. It is a signature of the co-tunneling process in which heat transport is induced by the tunneling process via virtual excitations, as discussed in Section 5.1. At low temperatures, $k_\mathrm{B}T \ll \hbar\Gamma$, $\hbar\bar{\Omega}$, $\hbar\omega_{20}^*$, it is supposed the system behaves effectively like the Ohmic spin-boson model with a single parameter ω_{10}^* because the high-energy states are almost irrelevant. Furthermore, for $k_\mathrm{B}T \lesssim 0.1\hbar\omega_{10}^*$, thermal excitation from the ground state to the first excited state is strongly suppressed, and then heat transport is governed by the co-tunneling process for which the linear thermal conductance is written as [37, 23, 38]

$$\kappa \approx \frac{\pi^3 \gamma k_\mathrm{B}^4}{30} \alpha^2 \chi_0^2 T^3, \tag{5.43}$$

where the static spin susceptibility χ_0 of the effective Ohmic spin-boson model is roughly approximated as $2/(\hbar\omega_{10}^*)$ for the weak coupling, $\alpha \ll 1$. Using $\alpha = \eta(4g/\Omega)^2$ and $\omega_{10}^* \propto \Omega$ for $\Omega \lesssim \Delta$, we obtain $\kappa(\Omega) \propto \Omega^{-6}$, which is consistent with the numerical result shown in the inset of Fig. 5.7.

5.4.3 Rotating-wave approximation

Finally, we comment on the contribution of the counter-rotating terms. By neglecting the counter-rotating terms, i.e., the rotating-wave approximation to the quantum Rabi model, we obtain the Jaynes-Cummings model, as discussed Section 2.4. While these two models give almost the same results in weak coupling regime, $g/\Delta \ll 1$, they are different in the ultrastrong coupling regime, $g/\Delta \gtrsim 1$. We stress that the qubit-resonator system in the ultrastrong coupling regime can be described not by the Jaynes-Cumming model but by the quantum Rabi model because the rotating-wave approximation fails in that regime. However, it would be instructive and useful to consider the Jaynes-Cummings model as a mathematical model or a model that may be realized in systems other than superconducting circuits. Since it is cumbersome to construct the NIBA for the Jaynes-Cummings model, we employ the approximation for the weak dissipation ($\eta \ll 1$) with the same procedure in Section 5.2.

For the convenience of later discussion, we introduced new Pauli operators, $\tau_{x,y,z}$, defined as

$$\tau_x = \sigma_z, \quad \tau_y = \sigma_y, \quad \tau_z = -\sigma_x. \tag{5.44}$$

This corresponds to a rotation of the coordinate around the y-axis by $\pi/2$. We also introduce the state vectors of the two-level system, $|0\rangle$ and $|1\rangle$, as eigenstates of τ_z as

$$\tau_z |0\rangle = -|0\rangle, \quad \tau_z |1\rangle = +|1\rangle. \tag{5.45}$$

For a decoupled system ($g = 0$), $|0\rangle$ and $|1\rangle$ correspond to the ground and excited states of the two-level system, respectively. Moreover, we define $\tau_+ = |1\rangle\langle 0|$ and

$\tau_- = |0\rangle \langle 1|$. Using these new operators and the identity $\tau_x = \tau_+ + \tau_-$, the Hamiltonian of the quantum Rabi model can be rewritten as

$$\mathcal{H}_R = \frac{\hbar\Delta}{2}\tau_z + \sum_r \hbar\Omega_r a_r^\dagger a_r + \sum_r \hbar g_r \left(\tau_+ + \tau_-\right)\left(a_r + a_r^\dagger\right). \tag{5.46}$$

After dropping the counter-rotating terms including $\tau_+ a^\dagger$ and $\tau_- a$ by applying the rotating-wave approximation, we finally obtain the Jaynes-Cummings model as

$$\mathcal{H}_{JC} = \frac{\hbar\Delta}{2}\tau_z + \sum_r \hbar\Omega_r a_r^\dagger a_r + \sum_r \hbar g_r \left(\tau_+ a_r + \tau_- a_r^\dagger\right). \tag{5.47}$$

For simplicity, we consider the symmetric case, $\Omega_L = \Omega_R \equiv \Omega$ and $\eta_L = \eta_R \equiv \eta$. Introducing new operators

$$A = \frac{a_L + a_R}{\sqrt{2}}, \quad B = \frac{a_L - a_R}{\sqrt{2}}, \tag{5.48}$$

corresponding to symmetric and antisymmetric modes, respectively, the Hamiltonian is expressed as

$$\mathcal{H}_{JC} = \mathcal{H}_A + \mathcal{H}_B, \tag{5.49}$$

$$\mathcal{H}_A = \frac{\hbar\Delta}{2}\tau_z + \hbar\Omega A^\dagger A + \sqrt{2}\hbar g \left(\tau_+ A + \tau_- A^\dagger\right), \tag{5.50}$$

$$\mathcal{H}_B = \hbar\Omega B^\dagger B. \tag{5.51}$$

From this expression, since the antisymmetric mode is completely decoupled with the two-level system, it does not contribute heat transport through a two-level system. Thus, it is sufficient to consider only the Hamiltonian H_A.

The Jaynes-Cummings model conserves the total number of particles, whose operator is $\hat{N} = \tau_+\tau_- + A^\dagger A$ while the quantum Rabi model does not. The basis of the Jaynes-Cummings model, $|\tau\rangle \otimes |n\rangle$, has an eigenvalue $N = \tau + n$, where $\tau (= 0, 1)$ and $n (= 0, 1, 2, \dots)$ assign the states of the two-level system and the symmetric mode, respectively. It is easy to show the ground state is given as $|0\rangle \otimes |0\rangle$. For the excited states, there are two eigenstates belonging to the same $N (\geq 1)$:

$$|i; N\rangle = a_{Ni} |0\rangle \otimes |N\rangle + b_{Ni} |1\rangle \otimes |N - 1\rangle, \quad (i = 1, 2), \tag{5.52}$$

where a_{Ni} and b_{Ni} are quantum amplitudes.

At low temperatures, the symmetrized correlation function is determined by the transitions from the ground state dominantly. Then, the symmetrized correlation function is written as

$$S_{JC}(\omega) \approx \pi \sum_{i=1,2} |\langle i; 1| \tau_x |0; 0\rangle|^2 \delta(\omega - \omega_{i,1} + \omega_{0,0}), \tag{5.53}$$

where $\hbar\omega_{i,N}$ is an energy eigenvalue of $|i; N\rangle$. Here, we have used the fact that the operator τ_x changes the eigenvalue N only by one. Thus, the existence of the conserved quantity, N, strongly restricts the possible transitions from the ground state to the excited states. However, the expression of the symmetrized correlation function in the Jaynes-Cummings model (5.53) indicates that it has indeed two peaks at $\omega = \omega_{i,1} - \omega_{0,0}$ ($i = 1, 2$). Therefore, we can conclude that the two-peak structure appears in the temperature dependence of the linear thermal conductance even for the

Jaynes-Cummings model when $\omega_{20}/\omega_{10} \gg 1$. Note that since the energy spectrum differs between the Jaynes-Cummings and the quantum Rabi models, particularly in the ultra-strong coupling regime [60], they give qualitatively different temperature dependences for the linear thermal conductance there.

5.5   Short summary of this chapter

We studied heat transport through an assembly, a two-level system embedded between harmonic resonators, described by the quantum Rabi model. By mapping the quantum Rabi model to the spin-boson model with the structured bath and using the noninteracting-blip approximation (NIBA), we calculated the linear thermal conductance. As a result, we discovered that the linear thermal conductance shows the two peaks as a function of the temperature in the ultrastrong coupling regime. We found that this characteristic behavior comes from the multiple levels in the quantum Rabi model. In addition, we found that the linear thermal conductance changes sensitively to the tunable parameter, particularly the natural frequency of the harmonic oscillators.

Chapter 6

Summary and Perspectives

In this thesis, we have studied three problems on transport properties of the superconducting circuits from several viewpoints. We have theoretically discussed various transport properties, in particular, with emphasis on many-body effects induced by system-environment coupling, Coulomb interaction, and disorder.

In Chapter 3, we investigated the quantum critical phenomena in the microwave scattering off a superconducting charge qubit coupled to an *RLC* transmission line, which is effectively described by the sub-Ohmic spin-boson model. This model exhibits a zero-temperature quantum phase transition at zero temperature due to the coupling between the two-level system and the heat bath. By performing the continuous-time quantum Monte Carlo simulation, we observed quantum critical behavior in the frequency dependence of the reflection loss consistent with analytic results using the renormalization group analysis. Moreover, by using the general relation between the circuit impedance and the spectral density of the heat bath, we showed that the sub-Ohmic heat bath could be constructed by the arrays of the *RLC* circuits whose circuit constants depend on the spacial positions. This study paves a path toward the observation of quantum critical phenomena in superconducting circuits in a controllable way. Because various types of quantum measurement on qubits are possible in superconducting circuits, it would be a challenging task to study the effect of its back-action on quantum phase transition.

In Chapter 4, we considered a one-dimensional Josephson-junction chain with the disorder and studied the transmission through it. The disordered Josephson-junction chain exhibit a superfluid-Bose glass transition at a critical Luttinger parameter $K_c = 3/2$, where the Luttinger parameter K is related to the circuit impedance as $Z = R_Q/(2K)$. We focused on the classical limit ($K \ll 1$), corresponding to the deep insulating regime, where the collective pinning affects an elastic scattering property in a wide frequency range. In the high-frequency regime, we investigated the transmission using the Fokker-Planck approach. The analytical formulas for the transmission agree with numerical results obtained by solving the Schödinger equation. Surprisingly, we found that the correlations of the pinning-induced disorder still affect the forward-scattering length despite the wavelength being shorter than the Larkin length. In the low-frequency regime, the localization becomes strong and the analytical approach does not work. To obtain information on this strongly-localized regime, we performed a brute-force numerical calculation. We found that the Lyapunov exponent is significantly increased, and its variance is suppressed in comparison with the well-known model with the Gaussian white-noise disorder. We show that the ratio $\ln \langle T(\omega) \rangle / \langle \ln T(\omega) \rangle$ takes a value near 1, indicating the strong correlation between the typical disorder configurations and rare disorder configurations optimal for the transmission determines the low-frequency transport properties. From the fact that the transmission is exponentially suppressed, we also found signatures of the scarcity of the localized low-frequency plasmon modes. It also

affects the distribution of the reflection phase. These observables make out unique signatures of the non-Gaussianity of the pinned chain. We expect that our study provides benchmarks for further developments of the dynamics in quantum Bose glass. It is an important future problem to investigate the effect of large quantum fluctuation ($K \sim 1$) beyond the classical regime ($K \ll 1$). It is also a fascinating problem to extend the present work to the experiment of inelastic microwave scattering.

Finally, we studied heat transport through the quantum Rabi model consisting of a superconducting qubit embedded between superconducting LC resonators. By using the exact mapping to the spin-boson model and the non-perturbative approximation, we evaluated the linear thermal conductance. In the ultra-strong coupling regime, the temperature dependence of the linear thermal conductance has a two-peak structure. This characteristic behavior comes from the fact that there are multiple levels in the quantum Rabi model and can not be observed in heat transport through a simple two-level system. Moreover, we found that the linear thermal conductance is highly sensitive to the controllable parameters, particularly to the natural frequency of the harmonic resonators. This property is advantageous to the application of well-controllable nanoscale heat devices such as a heat transistor. In this thesis, we restricted ourselves to the linear response theory to study quantum heat transport. For studying the rectification effect in heat transport through nanoscale objects, we need to expand our theory beyond the linear response.

In the last part of this chapter, we describe future perspectives of the present theoretical work. There are several future problems that may bring fruitful physics. First of all, this thesis treated only thermal equilibrium properties regarding to many-body effects in the superconducting circuits. While equilibrium properties are fundamental and important, the systems being in equilibrium is just a part of realistic systems. Therefore, it is important to expand our results toward non-equilibrium states under large temperature/voltage biases or strong excitations by microwaves. Next, it will be a fascinating problem to combine the many-body effects with quantum measurement. Thanks to the technological development in the superconducting circuit, the environment (e.g., a transmission line and a Josephson-junction chain) can be monitored mode by mode experimentally. It allows us to consider the effect of the quantum measurement of a small quantum system on the environments, i.e., "backaction". For example, by performing the quantum measurement to a superconducting qubit coupled to environments, we can trace how the quantum measurement affects modes in the environments. It is not only important in the aspect of fundamental physics but also expected to be helpful for quantum processing. Third, in the superconducting circuit, quantum dynamics away from the equilibrium states can be simulated. For example, in the superconducting circuit, we can switch on and off the interaction between an impurity and the Josephson transmission line by tuning a flux through. This setup enables us to study quantum quench dynamics of the many-body states in a controllable way. The theoretical investigation of such dynamics in superconducting circuits is also an important future problem. We expect that these general future problems will attract the interest of researchers in the near future. We hope that the present theoretical work will contribute to taking an important step towards future development in this direction.

Appendix A

Lagrangian and Hamiltonian for a transmission line

In this appendix, we derive the Lagrangian and Hamiltonian of the transmission line.

The transmission line is a long circuit in which electromagnetic waves can propagate freely. In the transmission line, the voltage and the current change over its length. Therefore, the capacitance and the inductance are represented in the density at a position, c and l, respectively. The lumped element model of the transmission line is a series of the LC-circuit with the inductance $l\,dx$ and the capacitance $c\,dx$, where dx is a spacing, per unit length as shown in Fig. A.1.

This formalism is valid not only for the transmission line but also for any linear circuit system. The Lagrangian of the lumped element model can be written down as

$$\mathcal{L} = \frac{1}{2}\dot{\vec{\phi}}^{t}\mathbb{C}\dot{\vec{\phi}} - \frac{1}{2}\vec{\phi}^{t}\mathbb{L}^{-1}\vec{\phi}, \tag{A.1}$$

where $\vec{\phi}$ is a vector whose components are the flux at node $n = 1, 2, \ldots, N$,

$$\vec{\phi} = \begin{pmatrix} \phi_1 \\ \phi_2 \\ \vdots \\ \phi_N \end{pmatrix}, \quad \dot{\vec{\phi}} = \begin{pmatrix} \dot{\phi}_1 \\ \dot{\phi}_2 \\ \vdots \\ \dot{\phi}_N \end{pmatrix}. \tag{A.2}$$

The capacitance matrix $\mathbb{C}$ and the inductance matrix $\mathbb{L}$ are real and symmetric. Note that what the Lagrangian can be written in the quadratic form means that the system is linear. Using the Euler-Lagrange equation, the evolution of the fluxes is described by

$$\ddot{\vec{\phi}} = -\mathbb{C}^{-1}\mathbb{L}^{-1}\vec{\phi}. \tag{A.3}$$
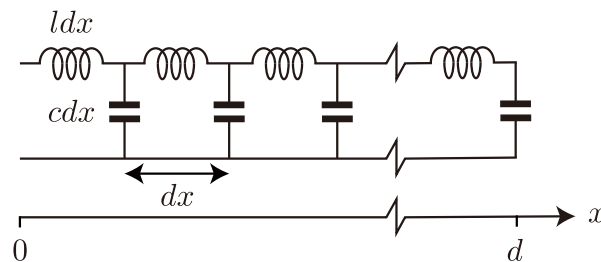

FIGURE A.1: Lumped element model of the transmission line.

From this equation, the system has resonance frequencies, and they are given by positive square root of the eigenvalues of the matrix $\mathbb{C}^{-1}\mathbb{L}^{-1}$.

By performing the Legendre transformation, the Lagrangian provides the Hamiltonian

$$\mathcal{H} = \frac{1}{2}\vec{Q}^t\mathbb{C}^{-1}\vec{Q} + \frac{1}{2}\vec{\phi}^t\mathbb{L}^{-1}\vec{\phi}, \tag{A.4}$$

where $\vec{Q}$ is a vector of charges at each node and has the relation to the flux,

$$\vec{Q} = \mathbb{C}\dot{\vec{\phi}}. \tag{A.5}$$

The charge component at node n is conjugate to the flux at the same node,

$$[Q_n, \phi_m] = i\hbar\delta_{n,m}. \tag{A.6}$$

Note that the Hamiltonian (A.4) and the commutation relation (A.6) recover ones of the *LC*-circuit (2.6) and (2.5) when one restricts a single node.

Now, we treat the transmission line as a quantum mechanical problem by replacing $\vec{Q}$ and $\vec{\phi}$ with operators [160]. First, let us introduce bosonic annihilation and creation operators a_n and $a_n^\dagger$, respectively, which satisfy the commutation relation $[a_n, a_m^\dagger] = \delta_{n,m}$,

$$\phi_n = \sqrt{\frac{\hbar}{2}}\sum_{m=1}^{N}\mathbb{A}_{n,m}\left(a_m + a_m^\dagger\right), \tag{A.7}$$

$$Q_n = -i\sqrt{\frac{\hbar}{2}}\sum_{m=1}^{N}\mathbb{B}_{n,m}\left(a_m - a_m^\dagger\right). \tag{A.8}$$

To hold the commutation relation, the coefficient matrices $\mathbb{A}$ and $\mathbb{B}$ has a relation,

$$\mathbb{A}\mathbb{B}^t = \mathbb{1}. \tag{A.9}$$

Using new variables, the Hamiltonian becomes

$$\mathcal{H} = \frac{\hbar}{4}\sum_{j,k=1}^{N}\left\{\left(a_j + a_j^\dagger\right)\left[\mathbb{B}^t\mathbb{C}^{-1}\mathbb{B}\right]_{j,k}\left(a_k + a_k^\dagger\right) - \left(a_j - a_j^\dagger\right)\left[\mathbb{A}^t\mathbb{L}^{-1}\mathbb{A}\right]_{j,k}\left(a_k - a_k^\dagger\right)\right\}. \tag{A.10}$$

The coefficient matrices $\mathbb{A}$ and $\mathbb{B}$ are chosen as matrices that diagonalize $\mathbb{L}$ and $\mathbb{C}$, respectively, such that

$$\mathbb{A}^t\mathbb{L}^{-1}\mathbb{A} = \mathbb{B}^t\mathbb{C}^{-1}\mathbb{B} = \begin{pmatrix} \omega_1 & 0 & \cdots & 0 \\ 0 & \omega_2 & \cdots & 0 \\ \vdots & \vdots & \ddots & \vdots \\ 0 & 0 & \cdots & \omega_N \end{pmatrix}. \tag{A.11}$$

In this choice, one can easily see that the columns of the coefficient matrix $\mathbb{A}$ are the eigenvectors of $\mathbb{C}^{-1}\mathbb{L}^{-1}$ with eigenvalues ω_n^2.

Finally, we can obtain the Hamiltonian on the diagonal basis,

$$\mathcal{H} = \sum_{n=1}^{N} \hbar\omega_n \left(a_n^\dagger a_n + \frac{1}{2} \right), \tag{A.12}$$

which means that a linear circuit with the inductances and capacitances is equivalent to a collection of harmonic oscillators.

Now, we consider transmission line with the constant element density. In the transmission line, the capacitance and inductance matrices are

$$\frac{\mathbb{C}}{cdx} = \mathbb{L}^{-1}ldx = \begin{pmatrix} 1 & -1 & 0 & 0 & \cdots & 0 \\ -1 & 2 & -1 & 0 & \cdots & 0 \\ 0 & -1 & 2 & -1 & \cdots & 0 \\ \vdots & \vdots & \ddots & \ddots & \ddots & \vdots \\ 0 & 0 & \cdots & -1 & 2 & -1 \\ 0 & 0 & \cdots & 0 & -1 & 1 \end{pmatrix}, \tag{A.13}$$

and eigenvalues of $\mathbb{L}^{-1}\mathbb{C}^{-1}$ are constant $\omega_n^2 = [1/(\sqrt{lc}dx)]^2$.

Finally, we consider the continuum limit, $dx \to 0$, of the transmission line. In this limit, the flux (charge) variable becomes a functions of position x, $\phi_n \to \phi(x)$ ($Q_n \to Q(x)dx$). Thus, the Lagrangian (A.1) reads

$$\mathcal{L} = \int_0^d dx \left\{ \frac{c}{2} [\partial_t\phi(x,t)]^2 - \frac{1}{2l} [\partial_x\phi(x,t)]^2 \right\}, \tag{A.14}$$

where d is the length of the transmission line and Euler-Lagrange equation for the Lagrangian provides the wave equation for the flux

$$v^2\partial_x^2\phi(x,t) - \partial_t^2\phi(x,t) = 0, \tag{A.15}$$

with the velocity $v = 1/\sqrt{lc}$. Note that when imposing the open boundary condition, $\partial_x\phi(0,t) = \partial_x\phi(d,t) = 0$, the position dependence of the flux is separable, $\phi(x,t) = \sum_n \phi(x)\cos(\pi nx/d)$, and thus one can recover the equation (A.3). Finally, by performing the Legendre transformation, we obtain the Hamiltonian for the transmission line in the continuum limit, Eq. (2.10) in the main text. It is clear that the Hamiltonian and the commutation relation of the transmission line in the continuum limit are natural extensions of the *LC*-circuit.

Appendix B

Lagrangian for a Josephson-junction chain

In this appendix, we derive the Lagrangian for the one-dimensional Josephson-junction chain shown in Fig. B.1. As discussed in Section 2.2, the Hamiltonian of a single Josephson junction is given by

$$\mathcal{H} = E_{\mathrm{J}} \left(1 - \cos \varphi\right) + E_{\mathrm{C}} q^2, \tag{B.1}$$

where E_{J} is the Josephson energy, $E_{\mathrm{C}} = (2e)^2/(2C)$ is the charging energy at the Josephson junction, q is the quasicharge on the Josephson junction, and φ is the phase difference across the Josephson junction. In this thesis, we consider the limit $E_{\mathrm{J}} \gg E_{\mathrm{C}}$, which corresponds to the transmon limit (see Section 2.3), to decrease quantum fluctuations of the phase across a single Josephson junction due to the quantum phase slips. In the transmon limit, each energy band is almost flat and the transition frequency between each band is estimated as the plasma frequency $\Omega = \sqrt{2E_{\mathrm{J}}E_{\mathrm{C}}}/\hbar$ (see Fig. 2.5). When considering only the lowest energy band, the plasma frequency plays the role of the ultraviolet cutoff in the low-energy theory. Then, eigenenergies in the lowest band are given by

$$E_{\mathrm{QPS}} = -\Lambda \cos(2\pi q), \tag{B.2}$$

where the half-band width Λ is determined by quantum phase slip, i.e., a non-perturbative process in which the phase difference across the Josephson junction φ_n jumps by $\pm 2\pi$ due to quantum tunneling between the minima of the Josephson
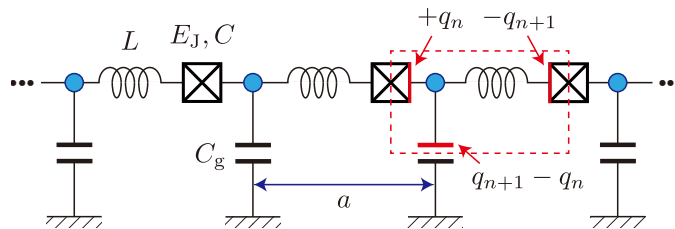

FIGURE B.1: Josephson-junction chain consisting of Josephson junctions with the Josephson energy E_{J} and the Josephson capacitance C_{J}, ground capacitances C_{g}, and phenomenological inductances L. The elementary cell length is a. The quasicharge on the n-th Josephson junction is q_n. The blue dots represent the superconducting islands.

energy. The amplitude of the quantum phase slip is given as

$$\Lambda = \frac{8}{\sqrt{\pi}} \left(2E_J^3 E_C\right)^{1/4} e^{-\sqrt{32E_J/E_C}}. \tag{B.3}$$

This is associated with the conjuration relation between the phase difference φ and quasi charge q as $[\varphi, q] = i$, i.e., operators $e^{\pm 2\pi i q}$ translate the phase difference by $\pm 2\pi$, $\varphi \to \varphi \pm 2\pi$. In the transmon limit ($E_J \gg E_C$), the amplitude is exponentially small, $\Lambda \ll 1$, and the quantum phase slips become rare events. When the number of the Josephson junctions in the chain is small enough, the contribution of the quantum phase slip is negligible and the Josephson-junction chain faithfully behaves as the superinductor consisting of Josephson inductances L_L. However, the recent technological development enables the realization of longer chains with $N \sim 10^4$ [89] for which a finite density of quantum phase slips can appear.

Since the total charge in the elementary cell, inside of the red-dashed box in Fig. B.1, is zero, the charge on the n-th ground capacitance is $2e(q_{n+1} - q_n)$, and the Coulomb energy at the ground capacitance along the Josephson-junction chain is

$$E_{\text{Coulomb}} = \sum_n \frac{(2e)^2}{2C_g}(q_{n+1} - q_n)^2. \tag{B.4}$$

We assume that all characteristic frequencies are much smaller than the plasma frequency and employ the adiabatic approximation in which the quasicharge is a smooth function of the position. In the continuum limit ($\sum_n a \to \int dx$), the Coulomb energy is expressed as

$$E_{\text{Coulomb}} = \int_0^d dx\, aE_g \left[\partial_x q(x,t)\right]^2. \tag{B.5}$$

where d is the chain length and $E_g = (2e)^2/(2C_g)$ is the charging energy at the ground capacitance. Note that the continuous approximation is valid when the characteristic wave vectors are much smaller than $1/a$ and the plasma frequency is much smaller than v/a [87]. The latter condition is equivalent to small ground capacitance $C_g \ll C$ (or $E_g \gg E_C$), which corresponds to the large charge screening length $\ell_{\text{sc}} = a\sqrt{C/C_g} \gg a$, i.e., long-range Coulomb interaction. The inductive energy along the chain is

$$E_{\text{inductive}} = \sum_n \frac{L}{2}\left(2e\dot{q}_n\right)^2, \tag{B.6}$$

and it can be expressed in the continuum limit as

$$E_{\text{inductive}} = \int_0^d dx\, \frac{1}{a}\frac{(2e)^2 L}{2}\left[\dot{q}(x,t)\right]^2. \tag{B.7}$$

Here, we have introduced the phenomenological inductance L between the Josephson junction for simplicity [87]. We note that the mass term, $\propto \dot{q}^2$, can be derived from the Hubbard-Stratonovich transformation [161, 162] without introducing the phenomenological inductance. In this derivation, the phenomenological inductance coincides with the Josephson inductance, Eq. (2.16), in the transmon limit ($E_J \gg E_C$).

Therefore, the inductive energy reads

$$E_{\text{inductive}} = \int_0^d dx \, \frac{1}{a} \frac{(2e)^2 L_J}{2} \, [\dot{q}(x,t)]^2 = \int_0^d dx \, \frac{1}{a} \frac{\hbar^2}{2E_J} \, [\dot{q}(x,t)]^2 . \tag{B.8}$$

Combining Eqs. (B.2), (B.5), and (B.8), we obtain the full Lagrangian as

$$\mathcal{L} = \int_0^d dx \, \left\{ \frac{1}{a} \frac{\hbar^2}{2E_J} \, [\dot{q}(x,t)]^2 - a E_g \, [\partial_x q(x,t)]^2 + \frac{1}{a} \Lambda \cos\left[2\pi q(x,t)\right] \right\} . \tag{B.9}$$

Finally, by introducing a new field $\theta(x,t) = \pi q(x,t)$, we obtain the Lagrangian, Eq. (2.44) in the main text.

Appendix C

Impedance of RLC Transmission Lines

In this appendix, we derive the analytical expression of the impedance of the RLC transmission lines with spatially-dependent resistances (3.28).

Assuming $|\omega C_{L,j} Z_{L,j+1}(\omega)| \ll 1$, the recurrence relation (3.26) becomes a differential equation in the continuous limit ($N \to \infty$):

$$\frac{\partial Z(\omega, x)}{\partial x} = -r(x) + i\omega l(x) + i\omega c(x) Z^2(\omega, x), \tag{C.1}$$

where $Z(\omega, x = j/N) \equiv Z_{L,j}(\omega)$, and $r(x)$, $l(x)$, and $c(x)$ are the resistance, capacitance, and inductance per unit length at $x = j/N$, respectively. The total impedance of the RLC transmission line is obtained from the relation $Z_L(\omega) = Z(\omega, x \to 0)$. The spatial dependence of the circuit elements given in Eq. (3.28) can be rewritten in the continuous limit as

$$r(x) = rx^n, \quad l(x) = 0, \quad c(x) = c. \tag{C.2}$$

At $x \gg x^* \equiv (n^2/4\omega rc)^{1/(n+2)}$, we can neglect $\partial_x Z(\omega, x)$ and then obtain the impedance as

$$Z(\omega, x) \approx Z_A(\omega, x) = \sqrt{\frac{r}{i\omega c}} \, x^{n/2}. \tag{C.3}$$

At $x \ll x^*$, where the first term, rx^n, on the right-hand side of Eq. (C.1), can be neglected, the impedance is given by

$$Z(\omega, x) \approx Z_B(\omega, x) = \frac{1}{-i\omega cx + f(\omega)}, \tag{C.4}$$

where $f(\omega)$ is the constant of integration determined from the condition $Z_A(\omega, x^*) = Z_B(\omega, x^*)$. Finally, we obtain the impedance of the RLC transmission line as

$$Z_L(\omega) \sim Z_B(\omega, x \to 0) = \frac{n}{\sqrt{2}\omega c} \left(\frac{4\omega rc}{n^2}\right)^{1/(n+2)} \left(1 + i\frac{n + \sqrt{2}}{\sqrt{2}}\right)^{-1}. \tag{C.5}$$

for $\omega^* \ll \omega \ll \omega_c$. Therefore, the spectral density is obtained as

$$I_L(\omega) \propto \tilde{I}_L(\omega) = \omega \text{Re}[Z_L(\omega)] \propto \omega^{1/(n+2)}. \tag{C.6}$$

This expression is consistent with Eq. (3.29). Note that the high-frequency cutoff ω_c

is obtained through the condition $\omega C |Z_A(\omega, x^*)| \ll 1$, where the recurrence relation (3.26) can be reduced to the differential equation (C.1) for $x < x^*$. The imaginary part of the impedance shows a sharp peak for $x \sim 1$. Then, for $x > x^*$, it can be neglected in the above analysis, given a condition $\omega C (1 - x^*) \mathrm{Im}\left[Z_A(\omega, x^*)\right] \gg 1$, which results in the low-frequency cutoff ω^* (3.30).

Appendix D

Fokker-Planck Equation

In this appendix, we provide the general recipe to derive the Fokker-Planck equation (4.43) from the Ricatti equation (4.42) and Gaussian correlators (4.36) and (4.37).

First, we consider the general dynamical equation for the multidimensional variable $\vec{X} = (X_1, X_2, \ldots, X_N)$,

$$\partial_t X_i(t) = a_i(\vec{X}(t)) + \sum_j b_{ij}(\vec{X}(t))\xi_j(t), \tag{D.1}$$

where $\xi_j(t)$ is the random force characterized by the Gaussian correlator,

$$\langle \xi_i(t)\xi_j(t')\rangle = 2D_{ij}\delta(t-t'). \tag{D.2}$$

Then, the joint probability $P(t, \vec{X})$ of the variables $X_1, X_2, \ldots, X_N$ satisfies the Fokker-Planck equation [163]

$$\frac{\partial P(t, \vec{X})}{\partial t} = -\sum_i \frac{\partial}{\partial X_i}\left[a_i(\vec{X})P(t, \vec{X})\right] + \sum_{ijlm} D_{lm}\frac{\partial}{\partial X_i}\left\{b_{il}(\vec{X})\frac{\partial}{\partial X_j}\left[b_{jm}(\vec{X})P(t, \vec{X})\right]\right\}. \tag{D.3}$$

This general formula has the correspondence with our model as follows: $t = x$, $\vec{X}(t) = z(x)$, $a_1 = 0$, $(b_{11}, b_{12}, b_{13}) = (2iz, i, iz^2)$, $(\xi_1, \xi_2, \xi_3) = (\Delta_0, \Delta^*, \Delta)$, and

$$\begin{pmatrix} D_{11} & D_{12} & D_{13} \\ D_{21} & D_{22} & D_{23} \\ D_{31} & D_{32} & D_{33} \end{pmatrix} = \begin{pmatrix} \omega_\star/2\ell_0(\omega) & 0 & 0 \\ 0 & 0 & \omega_\star/2\ell_\pi(\omega) \\ 0 & \omega_\star/2\ell_\pi(\omega) & 0 \end{pmatrix}. \tag{D.4}$$

By using the above correspondence and introducing $z = e^{i\theta_1}e^{-\theta_2}$, we obtain Eq. (4.43).

Appendix E

Exact Solution of $P_2(x, \theta_2)$

In this appendix, according to Ref. [135], we find the solution of Eq. (4.46) for the conditional probability $P_2(x, \theta_2)$ with the initial condition $P_2(x = d, \theta_2) = \delta(\theta_2 + \ln r_0)$.

To this end, we use various changes of variables to recover equivalent formulations of that equation. First, introducing $\tau = (d - x)/\ell_\pi$, λ (> 0) such that $e^{-2\theta_2} = \lambda/(1 + \lambda)$, and $\tilde{P}(\tau, \lambda) = P_2(\tau, \theta_2)|d\theta_2/d\lambda|$, Eq. (4.46) reads

$$\frac{\partial \tilde{P}}{\partial \tau} = \frac{\partial}{\partial \lambda} \left[\lambda(1 + \lambda) \frac{\partial \tilde{P}}{\partial \lambda} \right]. \tag{E.1}$$

Then, introducing X (> 0) such that $\lambda = \sinh^2 X$ and $\bar{P}(\tau, X) = \tilde{P}(\tau, \lambda)|d\lambda/dX|$, we find

$$\frac{\partial \bar{P}}{\partial \tau} = \frac{1}{4} \left[\frac{\partial^2 \bar{P}}{\partial X^2} - \frac{\partial}{\partial X} \left(\frac{2\cosh 2X}{\sinh 2X} \bar{P} \right) \right]. \tag{E.2}$$

Furthermore, using a new probability variable $Q(X) = \bar{P}(X)/\sqrt{\sinh 2X}$, it satisfies

$$-\frac{\partial Q}{\partial \tau} = \left(\mathcal{H} + \frac{1}{4} \right) Q \tag{E.3}$$

with an effective Hamiltonian

$$\mathcal{H} = -\frac{1}{4} \frac{\partial^2}{\partial X^2} - \frac{1}{4 \sinh^2 2X}. \tag{E.4}$$

Together with Eq. (E.2), the probability conservation,

$$\int_0^\infty dX \bar{P}(\tau, X) = 1, \tag{E.5}$$

imposes

$$\lim_{X \to 0} \left(\frac{\partial \bar{P}}{\partial X} - \frac{\bar{P}}{X} \right) = 0 \tag{E.6}$$

and, subsequently,

$$\lim_{X \to 0} \left(\frac{\partial Q}{\partial X} - \frac{Q}{2X} \right) = 0. \tag{E.7}$$

The knowledge about a normalized eigenspectrum of Eq. (E.4), $\mathcal{H}\psi_k = \varepsilon_k \psi_k$, with the boundary condition (E.7) allows us to express the conditional probability as

$$\bar{P}(\tau, X) = \sqrt{\frac{\sinh 2X}{\sinh 2X'}} \sum_k \psi_k(X)\psi_k^*(X')e^{-(\varepsilon_k+1/4)\tau}, \tag{E.8}$$

such that $P(0, X) = \delta(X - X')$ with $\cosh 2X' = (2 - T_0)/T_0$.

Now, we consider the solution of the eigenvalue problem, $\mathcal{H}\psi_k = \varepsilon_k \psi_k$, with the boundary condition (E.7). By changing variable $z = \cosh 2X \ (> 1)$ and $f_k(z)$ such that $\psi_k(X) = \sqrt{\sinh 2X} \, f_k(\cosh 2X)$, the new variable $f_k(z)$ satisfies the Legendre differential equation

$$\frac{d}{dz}\left[(1 - z^2)\frac{df_k}{dz}\right] + \nu(\nu + 1)f_k = 0, \tag{E.9}$$

with $(\nu + 1/2)^2 = -\varepsilon_k$. The boundary condition (E.7) translates into

$$\left[(z - 1)^{3/4}\frac{df_k(z)}{dz}\right]_{z \to 1} = 0. \tag{E.10}$$

The solution of Eq. (E.9) is expressed by the Legendre functions of the first and second kind, $P_\nu(z)$ and $Q_\nu(z)$, respectively. The boundary condition (E.10) excludes $Q_\nu(z)$ from the set of solutions because it diverges logarithmically at $z \to 1$. As $P_\nu(z) \sim z^{-\nu-1}$ for $|z| \gg 1$, the normalizability condition of the wavefunctions also requires $\mathrm{Re}[\nu] > 1/2$, which results in that only solutions with $\varepsilon_k > 0$ are allowed from the relation $(\nu + 1/2)^2 = -\varepsilon_k$. Thus, the set of solutions is given by the conical functions, $f_k(z) = C_k P_{-1/2+ik/2}(z)$ with $\varepsilon_k = k^2/4$ ($k > 0$) and the pre-factor C_k [as $P_{-1/2+ik/2}(z) = P_{-1/2-ik/2}(z)$]. The normalization condition

$$\int_0^\infty dx\psi_k(x)\psi_{k'}(x) = \delta(k - k') \tag{E.11}$$

is then obtained by choosing $C_k = \sqrt{\pi k \tanh(\pi k/2)}$. Finally, Eq. (E.8) reads

$$\bar{P}(\tau, X) = \frac{\sinh 2X}{2}\int_0^\infty dk \, k \tanh\left(\frac{\pi k}{2}\right)P_{-\frac{1}{2}+i\frac{k}{2}}(\cosh 2X)$$
$$\times P_{-\frac{1}{2}+i\frac{k}{2}}(\cosh 2X')e^{-(1+k^2)\tau/4}. \tag{E.12}$$

Reverting to variable θ_2 and setting $x = 0$, i.e., $\tau = d/\ell_\pi$, we obtain Eq. (4.48).

Appendix F

Gaussian White-noise Disorder Potential

In this appendix, we show analytical results from the literature on a model with Gaussian white-noise disorder potential, which was used in plotting some of the lines in Figs. 4.6, 4.9 and 4.8 [148, 145, 139]. We assume that the correlation of the disorder potential corresponds to the first term of Eq. (4.27) including the delta function as a white-noise disorder potential. Note that the literature mostly addresses the stationary Schrödinger equation at energy E. In the context of Eq. (4.10), we set $E = \omega^2 (\geq 0)$ and then use positive-energy results in literature.

The Lyapunov exponent for the white-noise disorder potential is given by [145]

$$\langle \gamma(\omega) \rangle R_\star = \frac{1}{2} \frac{\int_0^\infty dx \, \sqrt{x} \exp\left[-x^3/24 - x/2(\omega/\omega_\star)^2\right]}{\int_0^\infty dx \, 1/\sqrt{x} \exp\left[-x^3/24 - x/2(\omega/\omega_\star)^2\right]}. \tag{F.1}$$

This formula is plotted by the dotted line in Fig. 4.6 (a). Then, it yields the zero-frequency result

$$\langle \gamma(0) \rangle R_\star = \frac{3^{1/3} \sqrt{\pi}}{\Gamma(1/6)} \approx 0.46, \tag{F.2}$$

while, at $\omega \gg \omega_\star$, the Thouless relation holds $\langle \gamma(\omega) \rangle R_\star = (\omega_\star/\omega)^2/2$ as well as our pinned model.

The variance of the Lyapunov exponent is given by [141]

$$\langle\langle \gamma^2(\omega) \rangle\rangle R_\star d = \int_0^\infty ds \, \frac{1}{s} \text{Re}\left[\left(2\langle\gamma(\omega)\rangle R_\star - i\frac{d}{ds}\right) f^2(s)\right], \tag{F.3}$$

with $f(s) = \phi(s)/\phi(0)$ and

$$\phi(s) = \text{Ai}\left(-\frac{(\omega/\omega_\star)^2 + 2is}{2^{2/3}}\right) - i\,\text{Bi}\left(-\frac{(\omega/\omega_\star)^2 + 2is}{2^{2/3}}\right), \tag{F.4}$$

where Ai and Bi are Airy functions. This formula is plotted by the dotted line in Fig. 4.6 (b). It yields the zero-frequency result [139]

$$\langle\langle \gamma^2(0) \rangle\rangle d = \langle\gamma(0)\rangle \left[\frac{5\pi}{3\sqrt{3}} - {}_3F_2\left(1,1,\frac{7}{6};\frac{3}{2},\frac{3}{2};\frac{3}{4}\right)\right] \approx 1.1\,\langle\gamma(0)\rangle, \tag{F.5}$$

where ${}_3F_2$ is an hypergeometric function, while, at $\omega \gg \omega_\star$, $\langle\langle \gamma^2(\omega) \rangle\rangle d = \langle\gamma(\omega)\rangle$.

The distribution of the reflection phase at the perfect impedance matching ($K = K_0$) between a half-infinite chain and a waveguide [147],

$$P_1(\theta_1) = \left. \frac{(\omega/\omega_\star)^2 + Z^2}{2|\omega|/\omega_\star} P(Z) \right|_{Z=-(\omega/\omega_\star)\tan(\theta_1/2)}, \tag{F.6}$$

is related with the distribution of the Ricatti variable Z,

$$P(Z) = \frac{\int_0^\infty dx \, \exp\left[-x^3/24 - x/2(\omega/\omega_\star)^2 - x/2(Z - x/2)^2\right]}{\int_0^\infty dx \, \sqrt{2\pi/x} \exp\left[-x^3/24 - x/2(\omega/\omega_\star)^2\right]}. \tag{F.7}$$

From Eqs. (F.1) and (F.7), we can check that the relation

$$\langle \gamma(\omega) \rangle R_\star = \int dZ \, ZP(Z), \tag{F.8}$$

holds at any ω. While, at $\omega \gg \omega_\star$, the distribution is uniform, $P_1(\theta_1) \approx 1/(2\pi)$, at $0 < \omega \ll \omega_\star$, the distribution is concentrated around phase $\theta_1 = -\pi$ with

$$P_1(\theta_1) \approx \frac{\omega_\star}{\omega} p\left((\theta_1 + \pi)\frac{\omega_\star}{\omega}\right), \tag{F.9}$$

$$p(\varphi) = \frac{3^{5/6}}{\sqrt{\pi}\Gamma(1/6)} \int_0^\infty dx \, \frac{1}{\varphi^2} \exp\left(-\frac{x^3}{6} + \frac{x^2}{\varphi} - \frac{2x}{\varphi^2}\right), \tag{F.10}$$

if $|\theta_1 + \pi| \ll 1$. The function $p(\varphi)$ is plotted by the dotted line in the inset of Fig. 4.8. The tails of the distribution $P_1(\theta_1)$ at $|\theta_1 + \pi| \gg \omega/\omega_\star$ are given by

$$P_1(\theta_1) \approx \frac{\alpha\omega/\omega_\star}{\cos^2(\theta_1/2)}, \quad \alpha = \frac{3^{1/6}\Gamma(2/3)}{2^{7/3}\pi} \approx 0.10. \tag{F.11}$$

From Eq. (F.6), we can find the real part of the disorder-averaged reflection coefficient at any impedance mismatch ($K < K_0$),

$$r' + 1 = \frac{2}{1 + (K_0/K)^2 \tan^2(\theta_1/2)}. \tag{F.12}$$

While, at $\omega \gg \omega_\star$, Eq. (4.61) is reproduced with the uniform distribution, at $\omega \ll \omega_\star$, the average is contributed by the tails of the distribution $P_1(\theta_1)$, Eq. (F.11), which yields

$$\langle r' \rangle + 1 = 4\pi\alpha \frac{K}{K_0} \frac{\omega}{\omega_\star}. \tag{F.13}$$

At large impedance mismatch ($K \ll K_0$), Eq. (F.12) is approximated by $r' + 1 \approx 4\pi(K/K_0)\delta(\theta_1)$, which results in

$$\langle r' \rangle + 1 = 4\pi\frac{K}{K_0}P_1(\theta_1 = 0) \tag{F.14}$$

with $P_1(\theta_1)$ of Eq. (F.6). This formula is plotted by dotted line in Fig. 4.9. We can check that Eq. (F.14) reproduces Eq. (F.13) using Eq. (F.11) for $\theta_1 \approx 0$.

The linear frequency dependence in Eq. (F.13) at low frequency, as well as the saturation at $\omega \gg \omega_\star$, reflects the frequency dependence of the bulk plasmon density

of modes. Indeed by using the particle density of states of the Schrödinger problem [164, 165, 145] at energy $E = \omega^2$ (> 0), we find

$$\frac{\nu(\omega)}{\nu_0} = \frac{\omega}{\omega_\star} \sqrt{2\pi} \frac{\int_0^\infty dx \sqrt{x} \exp\left[-x^3/24 - x/2(\omega/\omega_\star)^2\right]}{\left\{\int_0^\infty dx \, 1/\sqrt{x} \exp\left[-x^3/24 - x/2(\omega/\omega_\star)^2\right]\right\}^2}, \tag{F.15}$$

where $\nu_0 = 1/(\pi v)$. In particular,

$$\nu(\omega)/\nu_0 = \begin{cases} 1, & (\omega \gg \omega_\star), \\ 6\pi \, 3^{1/6}/\Gamma^2(1/6) \, (\omega/\omega_\star) \approx 0.73 \, \omega/\omega_\star, & (\omega \ll \omega_\star). \end{cases} \tag{F.16}$$

The linear frequency dependence at low frequencies reflects the finite particle density of states $\tilde{\nu}(0)$ of the Schrödinger problem at $E = 0$ due to the relation $\nu(\omega) = 2\omega\tilde{\nu}(\omega^2)$, which connects the waves' and particles' densities of states. The finiteness of $\tilde{\nu}(0)$ is a precursor of the Lifshits tail of states at $E < 0$, which is an inaccessible region for waves. Note that the overall frequency dependences of $\langle r'(\omega) \rangle + 1$ and $\nu(\omega)$ are different.

Note that Eqs. (F.1) and (F.15) alternatively read

$$\langle \gamma(\omega) \rangle R_\star = -\text{Im}\left[f'(s = 0)\right], \tag{F.17}$$

$$\nu(\omega)/\nu_0 = -\omega_\star \text{Re}\left[\frac{d}{d\omega} f'(s = 0)\right], \tag{F.18}$$

respectively. Actually, the relation of the Lyapunov exponent $\langle \gamma(\omega) \rangle$ and the density of modes $\nu(\omega)$ to a common analytic function in the upper complex plane is valid beyond the Gaussian white-noise model. It is a consequence of the Herbert-Jones-Thouless relation [166] for any potential with translational invariance,

$$\gamma(E) - \gamma_0(E) = \int dE' \, \ln|E - E'| \left[\tilde{\nu}(E') - \tilde{\nu}_0(E')\right]. \tag{F.19}$$

Here, $\gamma_0(E) = \Theta(-E)\sqrt{-E}/v$ and $\tilde{\nu}_0(E) = \Theta(E)/(2\pi v\sqrt{E})$ are for a free particle. In the presence of a random potential, $\gamma(E)$ and $\tilde{\nu}(E)$ are the respective functions averaged over the disorder realizations, and the translational invariance property refers to the correlation function of the potential. Equation (F.8), which relates the Lyapunov exponent with the average the Ricatti variable, also holds for a translationally invariant disorder potential, under an additional assumption of inversion symmetric disorder [131].

Appendix G

Heat Current in the Keldysh Formalism

In this appendix, we derive the heat current mediated through the quantum Rabi model using the picture of the spin-boson model (5.10). The heat current from the heat bath r into the central system is defined as

$$J_r \equiv -\frac{d\mathcal{H}_{\mathrm{B},r}}{dt}. \tag{G.1}$$

Using the Heisenberg equation, the heat current operator reads

$$J_r = -i\hbar \frac{\sigma_z}{2} \sum_k \Lambda_{r,k} \Xi_{r,k} \left(-B_{r,k} + B_{r,k}^\dagger \right). \tag{G.2}$$

Then, the expectation value of the heat current is

$$\langle J_r(t) \rangle = -\frac{i\hbar}{2} \sum_k \Lambda_{r,k} \Xi_{r,k} \left\langle \sigma_z(t) \left(-B_{r,k}(t) + B_{r,k}^\dagger(t) \right) \right\rangle, \tag{G.3}$$

where $\mathcal{O}(t) = e^{+i\mathcal{H}_{\mathrm{sb}}t/\hbar} \mathcal{O} e^{-i\mathcal{H}_{\mathrm{sb}}t/\hbar}$ and $\langle \mathcal{O} \rangle = \mathrm{tr}[\rho_0 \mathcal{O}]$ with the initial density matrix ρ_0. Here, we assume that the initial density matrix can be described by product states:

$$\rho_0 = \rho_{\mathrm{TLS}} \otimes \prod_r \frac{e^{-\beta_r \mathcal{H}_{\mathrm{B},r}}}{Z_{\mathrm{B},r}}, \tag{G.4}$$

where ρ_{TLS} is the density matrix of the two-level system, $\beta_r = 1/(k_{\mathrm{B}} T_r)$ is the inverse temperature of the structured heat bath r, and $Z_{\mathrm{B},r}$ is the partition function of the structured heat bath r. The heat current can be expressed in terms of Green functions as

$$\langle J_r(t) \rangle = \mathrm{Re} \left[\sum_k \Xi_{r,k} \Lambda_{r,k} G^<_{\sigma_z, B_{r,k}^\dagger}(t_1, t_2) \right] \Bigg|_{t_1 = t_2 = t}, \tag{G.5}$$

where $G^<_{\sigma_z, B_{r,k}^\dagger}(t_1, t_2)$ is the lesser component of the Green function defined by

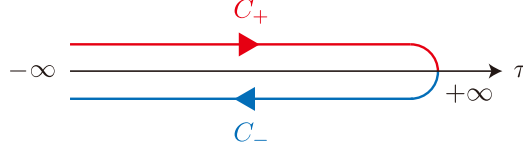$$G^<_{A,B}(t_1, t_2) \equiv -\frac{i}{\hbar} \langle B(t_2) A(t_1) \rangle. \tag{G.6}$$

FIGURE G.1: Keldysh contour $C = C_+ \cup C_-$. C_+ and C_- are forward and backward branches, respectively.

For later, we introduce other components of the Green function, the retarded and advanced components,

$$G^{\mathrm{R}}_{A,B}(t_1, t_2) \equiv -\frac{i}{\hbar}\theta(t_1 - t_2) \langle [A(t_1), B(t_2)] \rangle, \tag{G.7}$$

$$G^{\mathrm{A}}_{A,B}(t_1, t_2) \equiv +\frac{i}{\hbar}\theta(t_2 - t_1) \langle [A(t_1), B(t_2)] \rangle, \tag{G.8}$$

respectively, where $\theta(t)$ is the Heaviside step function.

Now, we move to the Keldysh contour and calculate the lesser component using the Keldysh formalism. As shown in Fig G.1, the Keldysh contour is composed of forward and backward branches, where the forward branch, C_+, is running from $t = -\infty$ to $t = +\infty$ and the backward one, C_-, is going back in the opposite direction. First, we introduce the Green function defined on the Keldysh contour as

$$G_{A,B}(\tau_1, \tau_2) \equiv -\frac{i}{\hbar} \langle T_C A(\tau_1) B(\tau_2) \rangle, \tag{G.9}$$

where τ is the Keldysh time defined on the Keldysh contour and T_C is the Keldysh time-ordered product operator. The formal expansion with respect to the coupling provides

$$G_{\sigma_z, B^\dagger_{r,k}}(\tau_1, \tau_2) = -\frac{i}{\hbar} \left\langle T_C S_C \tilde{\sigma}_z(\tau_1) \tilde{B}^\dagger_{r,k}(\tau_2) \right\rangle, \tag{G.10}$$

where $\tilde{\mathcal{O}}(\tau) = e^{+i(\mathcal{H}_{\mathrm{TLS}}+\mathcal{H}_{\mathrm{B}})\tau/\hbar}\mathcal{O}e^{-i(\mathcal{H}_{\mathrm{TLS}}+\mathcal{H}_{\mathrm{B}})\tau/\hbar}$ is the time evolution in the interaction picture. The S-matrix on the Keldysh contour S_C is

$$S_C = \sum_{n=0}^{\infty} \frac{(-i)^n}{n!} \int_C du_1 \cdots \int_C du_n\, \tilde{\mathcal{H}}_{\mathrm{I}}(u_1) \cdots \tilde{\mathcal{H}}_{\mathrm{I}}(u_n), \tag{G.11}$$

where the Keldysh time u and $\int_C du$ indicates a line integral along the Keldysh contour. By using the Wick's theorem [167], the Green function can be reduced to

$$G_{\sigma_z, B^\dagger_{r,k}}(\tau_1, \tau_2) = \frac{\Lambda_{r,k}}{2} \int_C du\, G_{\sigma_z, \sigma_z}(\tau_1, u) g_{B_{r,k} B^\dagger_{r,k}}(u, \tau_2), \tag{G.12}$$

where $g_{B_{r,k}, B^\dagger_{r,k}}(\tau, \tau')$ is the Green function of the isolated structured heat bath r. Now, we back to the real-time axis from the Keldysh contour by using the Langreth rule [168]. The lesser component can be expressed as

$$G^{<}_{\sigma_z, B^\dagger_{r,k}}(t_1, t_2) = \frac{\hbar \Lambda_{r,k}}{2} \int_{-\infty}^{\infty} dt' \left[G^{\mathrm{R}}_{\sigma_z, \sigma_z}(t_1, t') g^{<}_{B_{r,k}, B^\dagger_{r,k}}(t', t_2) + G^{<}_{\sigma_z, \sigma_z}(t_1, t') g^{\mathrm{A}}_{B_{r,k}, B^\dagger_{r,k}}(t', t_2) \right]. \tag{G.13}$$

Therefore, by plugging this expression into Eq. (G.5), the heat current can be written as

$$\langle J_r(t) \rangle = \text{Re} \int_{-\infty}^{\infty} dt' \, (-i) \frac{\partial}{\partial t_2} \left[G^{\text{R}}_{\sigma_z,\sigma_z}(t_1,t') \Sigma_r^<(t',t_2) + G^<_{\sigma_z,\sigma_z}(t_1,t') \Sigma_r^{\text{A}}(t',t_2) \right] \Big|_{t_1=t_2=t'},$$

(G.14)

where $\Sigma_r^<(t,t')$ and $\Sigma_r^{\text{A}}(t,t')$ are the lesser and advanced components of the self-energy,

$$\Sigma_r^<(t,t') \equiv \sum_k \frac{\hbar \Lambda_{r,k}^2}{2} g^<_{B_{r,k},B_{r,k}^\dagger}(t,t') = -\frac{i\hbar}{2} \int_0^\infty d\omega \, e^{-i\omega(t-t')} I_{\text{eff},r}(\omega) n_r(\omega),$$

(G.15)

$$\Sigma_r^{\text{A}}(t,t') \equiv \sum_k \frac{\hbar \Lambda_{r,k}^2}{2} g^{\text{A}}_{B_{r,k},B_{r,k}^\dagger}(t,t') = \frac{i\hbar}{2} \theta(t-t') \int_0^\infty d\omega \, e^{+i\omega(t-t')} I_{\text{eff},r}(\omega),$$

(G.16)

with the Bose-Einstein distribution, $n_r(\omega) = 1/(e^{\beta_r \omega} - 1)$, in the structured heat bath r. Here, we have used the definition of the spectral density (2.38). Finally, by performing the Fourier transformation, we obtain the formula for the heat current, Eq. (5.16) in the main text.

Appendix H

Mapping to the Spin-boson Model

In this appendix, we provide the detail of the mapping from the dissipative quantum Rabi model (5.4) to the spin-boson model (5.10) with the structured spectral density (5.14).

Let us start with the dissipative quantum Rabi model given as

$$\mathcal{H} = \mathcal{H}_S + \sum_r \left(\mathcal{H}_{\text{res},r} + \mathcal{H}_{\text{bath},r} \right) + \sum_r \left(\mathcal{H}_{\text{S-res},r} + \mathcal{H}_{\text{res-bath},r} \right), \tag{H.1}$$

$$\mathcal{H}_S = -\frac{\hbar\Delta}{2} \sigma_x, \tag{H.2}$$

$$\mathcal{H}_{\text{res},r} = \frac{P_r^2}{2m_{r,0}} + \frac{1}{2} M_r \Omega_r^2 X_r^2, \tag{H.3}$$

$$\mathcal{H}_{\text{bath},r} = \sum_k \left(\frac{p_{r,k}^2}{2m_{r,k}} + \frac{1}{2} m_{r,k} \omega_{r,k}^2 x_{r,k}^2 \right), \tag{H.4}$$

where $\mathcal{H}_S$, $\mathcal{H}_{\text{res},r}$, and $\mathcal{H}_{\text{bath},r}$ describe the two-level system, the harmonic oscillator $r\,(= \text{L}, \text{R})$, and the heat bath r, respectively. For the harmonic oscillator r, the Hamiltonian is rewritten using a natural frequency Ω_r, a mass M_r, a momentum operator P_r, and a position operator X_r. The heat bath r is described by a collection of the harmonic oscillators, where its Hamiltonian is similarly rewritten by using a natural frequency $\omega_{r,k}$, a mass $m_{r,k}$, a momentum operator $p_{r,k}$, and a position operator $x_{r,k}$. The coupling between the two-level system and the harmonic oscillator is described by

$$\mathcal{H}_{\text{S-res},r} = -\frac{1}{2} C_r \sigma_z X_r, \tag{H.5}$$

where C_r denotes a coupling strength. Similarly, the coupling between the harmonic oscillator and the heat bath is by

$$\mathcal{H}_{\text{res-bath},r} = -\sum_k c_{r,k} X_r x_{r,k}, \tag{H.6}$$

where $c_{r,k}$ denotes a coupling strength. It is easy to check that the Hamiltonian (H.1) reproduces the original form given in the main text (5.4) by introducing annihilation operators defined as

$$a_r = \sqrt{\frac{M_r \Omega_r}{2\hbar}} \left(X_r + \frac{i}{M_r \Omega_r} P_r \right), \tag{H.7}$$

$$b_{r,k} = \sqrt{\frac{m_{r,k} \omega_{r,k}}{2\hbar}} \left(x_{r,k} + \frac{i}{m_{r,k} \omega_{r,k}} p_{r,k} \right). \tag{H.8}$$

We note that the coupling strengths, C_r and $c_{r,k}$, are related to the parameters used in the main text as

$$g_r = -\frac{C_r}{\sqrt{8\hbar M_r \Omega_r}}, \quad \lambda_{r,k} = -\frac{c_{r,k}}{\sqrt{4M_r \Omega_r m_{r,k} \omega_{r,k}}}, \tag{H.9}$$

respectively.

Now, we consider a composite system composed of the harmonic oscillator r and the heat bath r, whose Hamiltonian is given as

$$\mathcal{H}_{\text{res+bath},r} = \mathcal{H}_{\text{res},r} + \mathcal{H}_{\text{bath},r} + \mathcal{H}_{\text{res-bath},r}. \tag{H.10}$$

The key idea of the present mapping is that the Hamiltonian $\mathcal{H}_{\text{res+bath},r}$ is exactly solvable because it only includes the harmonic oscillators. Indeed, the Hamiltonian $\mathcal{H}_{\text{res+bath},r}$ can be diagonalized by the canonical transformation [169, 170] as

$$\mathcal{H}_{\text{res+bath},r} = \sum_k \left(\frac{\tilde{p}_{r,k}^2}{2\tilde{m}_{r,k}} + \frac{1}{2}\tilde{m}_{r,k}\tilde{\omega}_{r,k}^2 \tilde{x}_{r,k}^2 \right), \tag{H.11}$$

where $\tilde{p}_{r,k}$ and $\tilde{x}_{r,k}$ are new momentum and position operators, respectively. This expression indicates that the composite system can be regarded as an effective heat bath for the spin-boson model. Then, the coupling between the effective heat bath and the two-level system is obtained by rewriting $\mathcal{H}_{\text{S-res},r}$ with the new operator $\tilde{x}_{r,k}$ as

$$\tilde{\mathcal{H}}_{\text{S-bath},r} = -\frac{1}{2}\sigma_z \sum_k \tilde{c}_{r,k}\tilde{x}_{r,k}, \tag{H.12}$$

where $\tilde{c}_{r,k}$ is a coupling strength between the two-level system and the effective heat bath. This coupling form between the two-level system and the heat bath takes the bilinear form after the canonical transformation. Thus, the resultant model becomes the spin-boson model. By using the relation

$$\sum_k \tilde{c}_{r,k}\tilde{x}_{r,k} = C_r X_r, \tag{H.13}$$

the spectral density of the effective heat bath can be written by

$$I_{\text{eff},r}(\omega) = \frac{C_r^2}{\pi\hbar}\text{Im}\left[G_r(\omega)\right]. \tag{H.14}$$

Here, $G_r(\omega)$ is the Fourier transformation of a correlation function of the harmonic oscillator

$$G_r(t) = -\frac{1}{i\hbar}\theta(t)\left\langle [X_r(t), X_r(0)] \right\rangle_{\text{bath},r}, \tag{H.15}$$

where $X_r(t)$ and $\langle X_r \rangle_{\text{bath},r}$ indicate the time evolution and the thermal average with respect to $\mathcal{H}_{\text{res+bath},r}$. The linear response theory allows the Fourier transformation of the correlation function to find [17]

$$G_r(\omega) = \frac{1}{M_r}\frac{1}{\Omega_r^2 - \omega^2 - i\omega\gamma_r(\omega)}, \tag{H.16}$$

with the friction kernel

$$\gamma_r(t) = \theta(t)\frac{1}{M_r}\sum_k \frac{c_{r,k}^2}{m_{r,k}\omega_{r,k}^2}\cos(\omega_{r,k}t). \tag{H.17}$$

Assuming the heat baths of the original model as the Ohmic baths (5.9), the Fourier transformation of the friction kernel reads constant, $\gamma_r(\omega) = 2\pi\eta_r\Omega_r = 2\Gamma_r$. Therefore, the effective spectral density (H.14) is calculated as

$$I_{\text{eff},r}(\omega) = \frac{C_r^2}{\pi\hbar M_r}\frac{2\Gamma_r\omega}{(\Omega_r^2 - \omega^2)^2 + (2\Gamma_r\omega)^2}. \tag{H.18}$$

Using Eq. (H.9), we obtain Eq. (5.14) in the main text.

Bibliography

[1] R. P. Feynman, International Journal of Theoretical Physics **21**, 467 (1982).

[2] M. A. Nielsen and I. L. Chuang, *Quantum Computation and Quantum Information: 10th Anniversary Edition* (Cambridge University Press, 2010).

[3] G. Wendin, Reports on Progress in Physics **80**, 106001 (2017).

[4] F. H. L. Koppens *et al.*, Nature **442**, 766 (2006).

[5] M. Veldhorst *et al.*, Nature Nanotechnology **9**, 981 (2014).

[6] M. D. Shulman *et al.*, Nature Communications **5**, 5156 (2014).

[7] I. Bloch, Nature **453**, 1016 (2008).

[8] R. Blatt and D. Wineland, Nature **453**, 1008 (2008).

[9] C. Weitenberg *et al.*, Nature **471**, 319 (2011).

[10] Y. Nakamura, Y. A. Pashkin, and J. S. Tsai, Nature **398**, 786 (1999).

[11] J. M. Gambetta, J. M. Chow, and M. Steffen, npj Quantum Information **3**, 2 (2017).

[12] A. Blais, R.-S. Huang, A. Wallraff, S. M. Girvin, and R. J. Schoelkopf, Phys. Rev. A **69**, 062320 (2004).

[13] J. Clarke and F. K. Wilhelm, Nature **453**, 1031 (2008).

[14] S. M. Girvin, M. H. Devoret, and R. J. Schoelkopf, Physica Scripta **T137**, 014012 (2009).

[15] M. H. Devoret and R. J. Schoelkopf, Science **339**, 1169 (2013).

[16] A. J. Leggett *et al.*, Rev. Mod. Phys. **59**, 1 (1987).

[17] U. Weiss, *Quantum Dissipative Systems*, 4th ed. (WORLD SCIENTIFIC, 2012).

[18] F. Guinea, V. Hakim, and A. Muramatsu, Phys. Rev. B **32**, 4410 (1985).

[19] A. Winter, H. Rieger, M. Vojta, and R. Bulla, Phys. Rev. Lett. **102**, 030601 (2009).

[20] M. Vojta, Phys. Rev. B **85**, 115113 (2012).

[21] K. Le Hur, Phys. Rev. B **85**, 140506 (2012).

[22] M. Goldstein, M. H. Devoret, M. Houzet, and L. I. Glazman, Phys. Rev. Lett. **110**, 017002 (2013).

[23] K. Saito and T. Kato, Phys. Rev. Lett. **111**, 214301 (2013).

[24] J. Puertas Martínez *et al.*, npj Quantum Information **5**, 19 (2019).

[25] P. W. Anderson, Phys. Rev. **109**, 1492 (1958).

[26] E. Abrahams, P. W. Anderson, D. C. Licciardello, and T. V. Ramakrishnan, Phys. Rev. Lett. **42**, 673 (1979).

[27] P. W. Anderson, Rev. Mod. Phys. **50**, 191 (1978).

[28] E. Abrahams, *50 Years of Anderson Localization* (WORLD SCIENTIFIC, 2010).

[29] S. Sachdev, *Quantum Phase Transitions*, 2 ed. (Cambridge University Press, 2011).

[30] R. M. Bradley and S. Doniach, Phys. Rev. B **30**, 1138 (1984).

[31] T. Giamarchi and H. J. Schulz, Phys. Rev. B **37**, 325 (1988).

[32] T. Giamarchi, *Quantum Phase Transitions* (Oxford University Press, 2003).

[33] J. P. Pekola, Nature Physics **11**, 118 (2015).

[34] J. P. Pekola, Europhysics News **52**, 15 (2021).

[35] J. P. Pekola and B. Karimi, Rev. Mod. Phys. **93**, 041001 (2021).

[36] D. Segal and A. Nitzan, Phys. Rev. Lett. **94**, 034301 (2005).

[37] T. Ruokola and T. Ojanen, Phys. Rev. B **83**, 045417 (2011).

[38] T. Yamamoto, M. Kato, T. Kato, and K. Saito, New Journal of Physics **20**, 093014 (2018).

[39] T. Yamamoto and T. Kato, Journal of the Physical Society of Japan **88**, 094601 (2019).

[40] T. Yamamoto, L. I. Glazman, and M. Houzet, Phys. Rev. B **103**, 224211 (2021).

[41] T. Yamamoto and T. Kato, Journal of Physics: Condensed Matter (2021).

[42] G.-L. Ingold and Y. V. Nazarov, Charge tunneling rates in ultrasmall junctions, in *Single Charge Tunneling: Coulomb Blockade Phenomena in Nanostructures*, edited by H. Grabert and M. H. Devoret, pp. 21–108, NATO ASI Series, Plenum Press, New York, 1992.

[43] B. D. Josephson, Physics Letters **1**, 251 (1962).

[44] B. D. Josephson, Rev. Mod. Phys. **36**, 216 (1964).

[45] A. Schmid, Phys. Rev. Lett. **51**, 1506 (1983).

[46] F. Guinea, V. Hakim, and A. Muramatsu, Phys. Rev. Lett. **54**, 263 (1985).

[47] G. Schön and A. Zaikin, Physics Reports **198**, 237 (1990).

[48] P. Werner and M. Troyer, Phys. Rev. Lett. **95**, 060201 (2005).

[49] S. L. Lukyanov and P. Werner, Journal of Statistical Mechanics: Theory and Experiment **2007**, P06002 (2007).

[50] M. Houzet and L. I. Glazman, Phys. Rev. Lett. **125**, 267701 (2020).

[51] J. Koch *et al.*, Phys. Rev. A **76**, 042319 (2007).

[52] J. A. Schreier *et al.*, Phys. Rev. B **77**, 180502 (2008).

[53] P. Jurcevic *et al.*, arXiv:2008.08571v2 .

[54] J. E. Mooij *et al.*, Science **285**, 1036 (1999).

[55] I. Chiorescu, Y. Nakamura, C. J. P. M. Harmans, and J. E. Mooij, Science **299**, 1869 (2003).

[56] J. Bourassa *et al.*, Phys. Rev. A **80**, 032109 (2009).

[57] I. I. Rabi, Phys. Rev. **49**, 324 (1936).

[58] D. Braak, Phys. Rev. Lett. **107**, 100401 (2011).

[59] E. Jaynes and F. Cummings, Proceedings of the IEEE **51**, 89 (1963).

[60] A. Frisk Kockum, A. Miranowicz, S. De Liberato, S. Savasta, and F. Nori, Nature Reviews Physics **1**, 19 (2019).

[61] P. Forn-Díaz, L. Lamata, E. Rico, J. Kono, and E. Solano, Rev. Mod. Phys. **91**, 025005 (2019).

[62] F. Yoshihara *et al.*, Phys. Rev. Lett. **120**, 183601 (2018).

[63] R. P. Feynman and F. L. Vernon Jr., Annals of Physics **24**, 118 (1963).

[64] A. O. Caldeira and A. J. Leggett, Annals of Physics **149**, 374 (1983).

[65] Y. Makhlin, G. Schön, and A. Shnirman, Rev. Mod. Phys. **73**, 357 (2001).

[66] W. de Haas, J. de Boer, and G. van dën Berg, Physica , 1115 (1934).

[67] A. C. Hewson, *The Kondo Problem to Heavy Fermions* (Cambridge University Press, 1993).

[68] J. Kondo, Progress of Theoretical Physics **32**, 37 (1964).

[69] P. W. Anderson, Journal of Physics C: Solid State Physics **3**, 2436 (1970).

[70] K. G. Wilson, Rev. Mod. Phys. **47**, 773 (1975).

[71] P. Nozières and A. Blandin, J. Phys. France **41**, 193 (1980).

[72] N. Andrei, Phys. Rev. Lett. **45**, 379 (1980).

[73] P. B. Wiegmann, Sov. Phys. JETP Lett. **31**, 392 (1980).

[74] J. Li, W.-D. Schneider, R. Berndt, O. R. Bryant, and S. Crampin, Phys. Rev. Lett. **81**, 4464 (1998).

[75] V. Madhavan, W. Chen, T. Jamneala, M. F. Crommie, and N. S. Wingreen, Science **280**, 567 (1998).

[76] D. Goldhaber-Gordon *et al.*, Nature **391**, 156 (1998).

[77] W. G. van der Wiel *et al.*, Science **289**, 2105 (2000).

[78] L. Riegger *et al.*, Phys. Rev. Lett. **120**, 143601 (2018).

[79] P. W. Anderson and G. Yuval, Journal of Physics C: Solid State Physics **4**, 607 (1971).

[80] J. M. Kosterlitz, Phys. Rev. Lett. **37**, 1577 (1976).

[81] P. Forn-Díaz *et al.*, Nature Physics **13**, 39 (2017).

[82] S. Léger *et al.*, Nature Communications **10**, 5259 (2019).

[83] L. Magazzù and M. Grifoni, Journal of Statistical Mechanics: Theory and Experiment **2019**, 104002 (2019).

[84] M. Devoret, S. Girvin, and R. Schoelkopf, Annalen der Physik **16**, 767 (2007).

[85] K. K. Likharev and A. B. Zorin, Journal of Low Temperature Physics **59**, 347 (1985).

[86] K. A. Matveev, A. I. Larkin, and L. I. Glazman, Phys. Rev. Lett. **89**, 096802 (2002).

[87] V. Gurarie and A. M. Tsvelik, Journal of Low Temperature Physics **135**, 245 (2004).

[88] V. E. Manucharyan, J. Koch, L. I. Glazman, and M. H. Devoret, Science **326**, 113 (2009).

[89] R. Kuzmin *et al.*, Nature Physics **15**, 930 (2019).

[90] M. Bard, I. V. Protopopov, I. V. Gornyi, A. Shnirman, and A. D. Mirlin, Phys. Rev. B **96**, 064514 (2017).

[91] D. Ristè *et al.*, Nature Communications **4**, 1913 (2013).

[92] D. A. Ivanov, Phys. Rev. Lett. **86**, 268 (2001).

[93] J. R. Friedman and D. V. Averin, Phys. Rev. Lett. **88**, 050403 (2002).

[94] A. I. Larkin and Y. N. Ovchinnikov, Sov. Phys. JETP **38**, 854 (1974).

[95] A. I. Larkin, Sov. Phys. JETP **31**, 784 (1970).

[96] Y. Imry and S.-k. Ma, Phys. Rev. Lett. **35**, 1399 (1975).

[97] H. Fukuyama and P. A. Lee, Phys. Rev. B **17**, 535 (1978).

[98] M. Houzet and L. I. Glazman, Phys. Rev. Lett. **122**, 237701 (2019).

[99] I. L. Aleiner and I. M. Ruzin, Phys. Rev. Lett. **72**, 1056 (1994).

[100] M. M. Fogler, Phys. Rev. Lett. **88**, 186402 (2002).

[101] V. Gurarie and J. T. Chalker, Phys. Rev. Lett. **89**, 136801 (2002).

[102] V. Gurarie and J. T. Chalker, Phys. Rev. B **68**, 134207 (2003).

[103] Y. Suzumura and H. Fukuyama, Journal of the Physical Society of Japan **52**, 2870 (1983).

[104] A. Ronzani *et al.*, Nature Physics **14**, 991 (2018).

[105] J. P. Pekola and B. Karimi, arXiv:2010.11122v1 .

[106] J. Senior *et al.*, Communications Physics **3**, 40 (2020).

[107] T. Ojanen and A.-P. Jauho, Phys. Rev. Lett. **100**, 155902 (2008).

[108] K. Joulain, J. Drevillon, Y. Ezzahri, and J. Ordonez-Miranda, Phys. Rev. Lett. **116**, 200601 (2016).

[109] M. Kilgour and D. Segal, Phys. Rev. E **98**, 012117 (2018).

[110] B. Karimi and J. P. Pekola, Phys. Rev. B **94**, 184503 (2016).

[111] R. Uzdin, A. Levy, and R. Kosloff, Phys. Rev. X **5**, 031044 (2015).

[112] J. Klatzow *et al.*, Phys. Rev. Lett. **122**, 110601 (2019).

[113] S. K. Kehrein, A. Mielke, and P. Neu, Zeitschrift für Physik B Condensed Matter **99**, 269 (1995).

[114] S. K. Kehrein and A. Mielke, Physics Letters A **219**, 313 (1996).

[115] R. Bulla, N.-H. Tong, and M. Vojta, Phys. Rev. Lett. **91**, 170601 (2003).

[116] M. Vojta, N.-H. Tong, and R. Bulla, Phys. Rev. Lett. **94**, 070604 (2005).

[117] M. Vojta, N.-H. Tong, and R. Bulla, Phys. Rev. Lett. **102**, 249904 (2009).

[118] A. W. Chin, J. Prior, S. F. Huelga, and M. B. Plenio, Phys. Rev. Lett. **107**, 160601 (2011).

[119] E. Luijten and H. W. J. Blöte, Phys. Rev. B **56**, 8945 (1997).

[120] E. Luijten, *Interaction Range, Universality and the Upper Critical Dimension* (Ph.D. thesis, Delft University of Technology, 1997).

[121] N.-H. Tong and M. Vojta, Phys. Rev. Lett. **97**, 016802 (2006).

[122] L. Yu, N. Tong, Z. Xue, Z. Wang, and S. Zhu, Science China Physics, Mechanics and Astronomy **55**, 1557 (2012).

[123] H. Bruus and K. Flensberg, *Many-Body Quantum Theory in Condensed Matter Physics: An Introduction* (Oxford University Press, 2004).

[124] A. A. Clerk, M. H. Devoret, S. M. Girvin, F. Marquardt, and R. J. Schoelkopf, Rev. Mod. Phys. **82**, 1155 (2010).

[125] H. Rieger and N. Kawashima, The European Physical Journal B **9**, 233 (1999).

[126] R. H. Swendsen and J.-S. Wang, Phys. Rev. Lett. **58**, 86 (1987).

[127] G. A. Baker and P. Graves-Morris, *Padé Approximants*, 2 ed. (Cambridge University Press, 1996).

[128] F. B. Anders, R. Bulla, and M. Vojta, Phys. Rev. Lett. **98**, 210402 (2007).

[129] M. Sassetti and U. Weiss, Phys. Rev. Lett. **65**, 2262 (1990).

[130] H. Shiba, Progress of Theoretical Physics **54**, 967 (1975).

[131] I. M. Lifshits, S. A. Gredeskul, and L. A. Pastur, *Introduction to the Theory of Disordered Systems* (Wiley, 1988).

[132] M. E. Gertsenshtein and V. B. Vasil'ev, Theory of Probability and its Applications **54**, 391 (1959).

[133] A. A. Abrikosov and I. A. Ryzhkin, Sov. Phys. JETP **44**, 630 (1976).

[134] T. N. Antsygina, L. A. Pastur, and V. A. Slyusarev, Sov. J. Low. Temp. Phys. **7**, 1 (1981).

[135] C. W. J. Beenakker and B. Rejaei, Phys. Rev. Lett. **71**, 3689 (1993).

[136] 7 - definite integrals of special functions, in *Table of Integrals, Series, and Products (Eighth Edition)*, edited by D. Zwillinger, V. Moll, I. Gradshteyn, and I. Ryzhik, pp. 776–865, Academic Press, Boston, , eighth edition ed., 2014.

[137] D. J. Thouless, Journal of Physics C: Solid State Physics **6**, L49 (1973).

[138] L. I. Deych, A. A. Lisyansky, and B. L. Altshuler, Phys. Rev. Lett. **84**, 2678 (2000).

[139] H. Schomerus and M. Titov, Phys. Rev. E **66**, 066207 (2002).

[140] L. I. Deych, M. V. Erementchouk, and A. A. Lisyansky, Phys. Rev. Lett. **90**, 126601 (2003).

[141] C. Texier, Journal of Statistical Physics **181**, 990 (2020).

[142] I. M. Lifshits and V. Y. Kirpichenkov, Sov. Phys. JETP **50**, 499 (1979).

[143] A. I. Larkin and K. A. Matveev, Sov. Phys. JETP **66**, 580 (1987).

[144] J. B. Pendry, Journal of Physics C: Solid State Physics **20**, 733 (1987).

[145] B. Derrida and E. Gardner, Journal de Physique **45**, 1283 (1984).

[146] L. D. Landau and E. M. Lifshitz, *Quantum Mechanics: Non-relativistic Theory*, 3rd ed. (Pergamon Press).

[147] P. Sulem, Physica **70**, 190 (1973).

[148] C. Barnes and J. M. Luck, Journal of Physics A: Mathematical and General **23**, 1717 (1990).

[149] J. B. Pendry, Journal of Physics A: Mathematical and General **16**, 2161 (1983).

[150] R. Landauer, IBM Journal of Research and Development **1**, 223 (1957).

[151] R. Landauer, Physics Letters A **85**, 91 (1981).

[152] K. Schwab, E. A. Henriksen, J. M. Worlock, and M. L. Roukes, Nature **404**, 974 (2000).

[153] M. Meschke, W. Guichard, and J. P. Pekola, Nature **444**, 187 (2006).

[154] A. V. Timofeev, M. Helle, M. Meschke, M. Möttönen, and J. P. Pekola, Phys. Rev. Lett. **102**, 200801 (2009).

[155] M. C. Goorden, M. Thorwart, and M. Grifoni, Phys. Rev. Lett. **93**, 267005 (2004).

[156] D. Zueco and J. García-Ripoll, Phys. Rev. A **99**, 013807 (2019).

[157] Y. Meir and N. S. Wingreen, Phys. Rev. Lett. **68**, 2512 (1992).

[158] K. Saito, EPL (Europhysics Letters) **83**, 50006 (2008).

[159] F. Nesi, M. Grifoni, and E. Paladino, New Journal of Physics **9**, 316 (2007).

[160] I. Snyman and S. Florens, Phys. Rev. B **92**, 085131 (2015).

[161] J. Homfeld, I. Protopopov, S. Rachel, and A. Shnirman, Phys. Rev. B **83**, 064517 (2011).

[162] N. Vogt *et al.*, Phys. Rev. B **92**, 045435 (2015).

[163] J. Klafter and I. M. Sokolov, *First Steps in Random Walks: From Tools to Applications* (Oxford University Press, 2021).

[164] H. L. Frisch and S. P. Lloyd, Phys. Rev. **120**, 1175 (1960).

[165] B. I. Halperin, Phys. Rev. **139**, A104 (1965).

[166] D. J. Thouless, Journal of Physics C: Solid State Physics **5**, 77 (1972).

[167] G. D. Mahan, *Many-Particle Physics*, 3rd ed. (Springer, 2000).

[168] G. Stefanucci and R. van Leeuwen, *Nonequilibrium Many-Body Theory of Quantum Systems: A Modern Introduction* (Cambridge University Press, 2013).

[169] U. Fano, Phys. Rev. **124**, 1866 (1961).

[170] T. Kato, A. A. Golubov, and Y. Nakamura, Phys. Rev. B **76**, 172502 (2007).